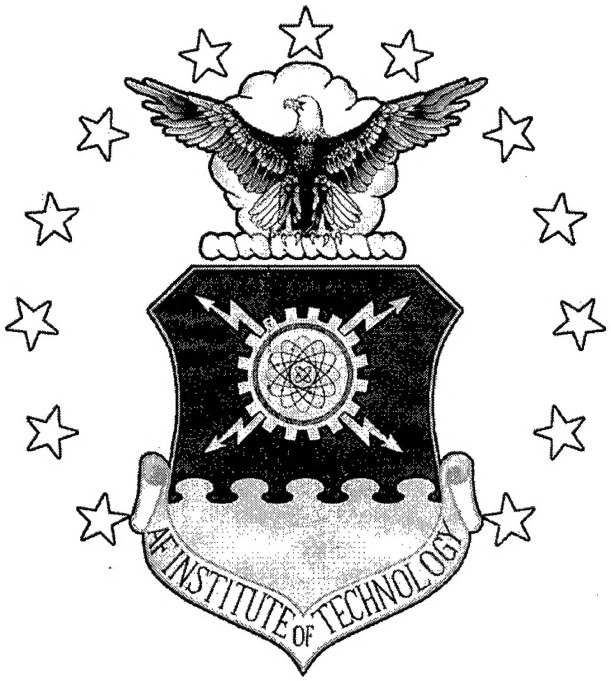

MODELING PIEZOCERAMIC TWIST ACTUATION IN SINGLE-CELL ANISOTROPIC TORQUE BOX OF LOW-OBSERVABLE UAV WING

THESIS

Peter Cseke, Jr., Captain, USAF

AFIT/GAE/ENY/00M-4

DEPARTMENT OF THE AIR FORCE
AIR UNIVERSITY

AIR FORCE INSTITUTE OF TECHNOLOGY

Wright-Patterson Air Force Base, Ohio

The views expressed in this thesis are those of the author and do not reflect the official policy or position of the Department of Defense or the United States Government.

AFIT/GAE/ENY/00M-4

MODELING PIEZOCERAMIC TWIST ACTUATION IN SINGLE-CELL ANISOTROPIC TORQUE BOX OF LOW-OBSERVABLE UAV WING

THESIS

Presented to the Faculty of the School of Engineering and Management

of the Air Force Institute of Technology

Air University

In Partial Fulfillment of the

Requirements for the Degree of

Master of Science in Aeronautical Engineering

Peter Cseke, Jr., B.S. B.S.

Captain, USAF

March, 2000

AFIT/GAE/ENY/00M-4

MODELING PIEZOCERAMIC TWIST ACTUATION IN SINGLE-CELL ANISOTROPIC TORQUE BOX OF LOW-OBSERVABLE UAV WING

Peter Cseke, Jr., B.S. B.S.

Captain, USAF

Approved:

Captain Gregory S. Agnes, Ph.D. Thesis Advisor	09 Mar 00 Date
LtCol Jeffrey S. Turcotte, Ph.D. Committee Member	08 MAR 2000 Date
Dr. Bradley S. Liebst Committee Member	09 MAR 00 Date

Preface

I would like to thank Capt Greg Agnes, Ph.D. for his never ending patience in providing guidance toward establishing the correct methods and more complete expressions presented in this thesis, and his help in showing me actually how simple some of the solutions were to many of my over-complicated problem statements. His help in installing LaTEX — the software on which this thesis was written — and explaining JPEG-to-encapsulated postscript conversion was instrumental in completing this work. I am grateful for his efforts in developing the LaTEX slide-show style files used for the thesis presentation. Without it, preparing for the defense would have been a great deal more arduous. I also would like to thank the faculty of the Department of Aeronautics and Astronautics for their support, and for constantly reminding me (as well as the others) that this was supposed to be fun! I would like to thank Dr. Brad Liebst, our Department Head, for always sounding off during his lectures. Also, many thanks for keeping his office candy jar always filled to the brim. Thank you Lt. Col Little for deciding not to give homework assignments during the end-of-quarter "crunch-time", and Lt. Col Turcotte, for never ever leaving his course outlines to a chance. Finally, I extend my gratitude to the Air Force for selecting me for this master's program, and for continuing to send me to very exotic places.

Peter Cseke, Jr.

Table of Contents

List of Figures

List of Tables

Abstract

The reduction of an aircraft's radar cross section can increase its survivability in hostile airspace by making it more difficult to locate and track by enemy radar. Replacing articulated flight control surfaces with adaptive controls will reduce surface discontinuities, and enhance low observability. Actuation of the aerodynamic surfaces is achieved by an electric field applied to PZT actuators embedded in the top and bottom skins, creating differential strain and shear in the host substrate. This creates torsion about the elastic axis, and a change in the wing lift coefficient. The torsion of the designed baseline UAV's wing torquebox was modeled in the presence of a full complement of air-loads by extending the Bredt-Batho theorem. This was accomplished through modifying Libove's method, using a thin-walled, linearly elastic, fully anisotropic, trapezoid cross-section beam. The linear tip twist angles due to a uniform cross-sectional moment were verified using the isotropic Bredt-Batho theorem, and published anisotropic results by applying isotropic, then anisotropic laminate elastic properties. The isotropic solutions were within 3.1%; the anisotropic results were within 6.9-10.9% of the published angles. The PZT actuation of the host structure was achieved by substituting the PZT-composite laminate elastic properties into the derived solution and inducing strain and shear of the PZT lamina by applying an electric field, without the presence of external forces or moments. Using two different PZT laminae, the angular twist as a function of the host lamina orientation angle and applied voltage was recorded. The amount of twist ranged between 0.03-0.39 degrees, and 0.12-1.04 degrees for the AFC and G-1195 PZT laminae respectively.

MODELING PIEZOCERAMIC TWIST ACTUATION IN SINGLE-CELL ANISOTROPIC TORQUE BOX OF LOW-OBSERVABLE UAV WING

I. Introduction

Mathematics up to the present day have been quite useless to us in regard to flying.

From the 14th Annual Report of the Aeronautical Society of Great Britain, 1879

1.1 Background

1.1.1 Aerial Reconnaissance. Strategic and tactical reconnaissance have been the sources of intelligence information for military commanders since the first human armed conflict. One form of today's military intelligence gathering is overflight by reconnaissance vehicles, such as a satellite or aircraft. These sources provide detailed and accurate information that is mostly independent of local weather (Synthetic Aperture Radar, or infrared photography); however, they cannot always meet real-time demand. One might need to wait hours before the satellite is in position or until the long-range aircraft from a far away base is launched. Today's battle commanders and combat controllers demand up to the minute information on enemy positions as well as real-time battle damage assessment in almost all weather conditions. The tactical unmanned aerial vehicles

(UAVs) can provide those pieces of information. They are deployed close to the conflict areas, can reach their targets quickly, loiter above the target area for extended periods, and they can also be quickly turned around for new missions.

The UAVs for strategic reconnaissance in our current inventory are divided into three categories. The conventional, medium altitude endurance UAV, Predator (Tier II) is designed to provide 24-hour, near continuous, on-station surveillance with a 500 nm operational radius using simultaneous carriage of electro-optical (EO), infrared (IR) and synthetic aperture radar (SAR) sensors, at an altitude of 25,000 feet. Demonstrated system capability can provide 20 hours total flight time at 13,000 ft [7].

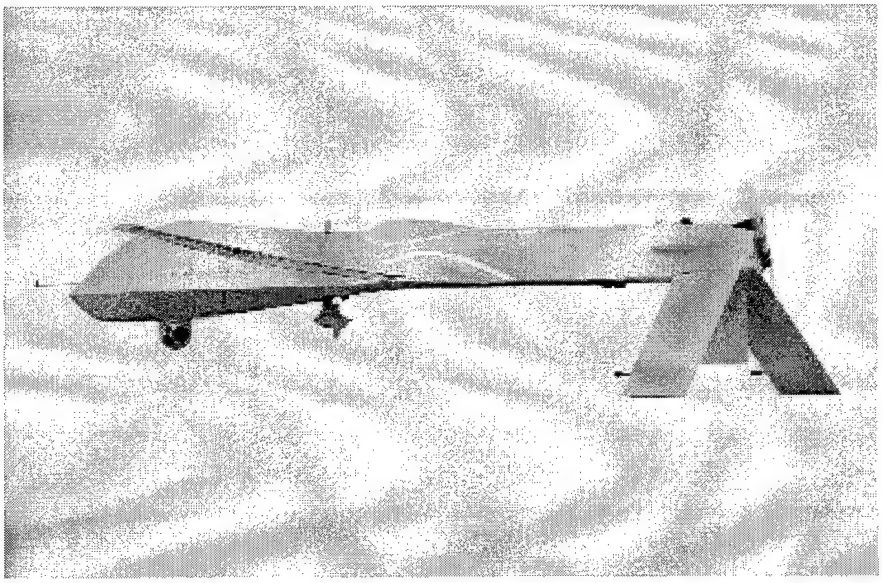

Figure 1.1 MAE Predator UAV

The conventional, high-altitude endurance (HAE) UAV, Global Hawk (Tier II+) is designed to provide 24 hour, on-station surveillance with a 3000 nm radius using EO, IR and SAR sensors at an altitude of over 50,000 ft. The higher altitude and longer operational radius allows greater survivability and operational flexibility [7].

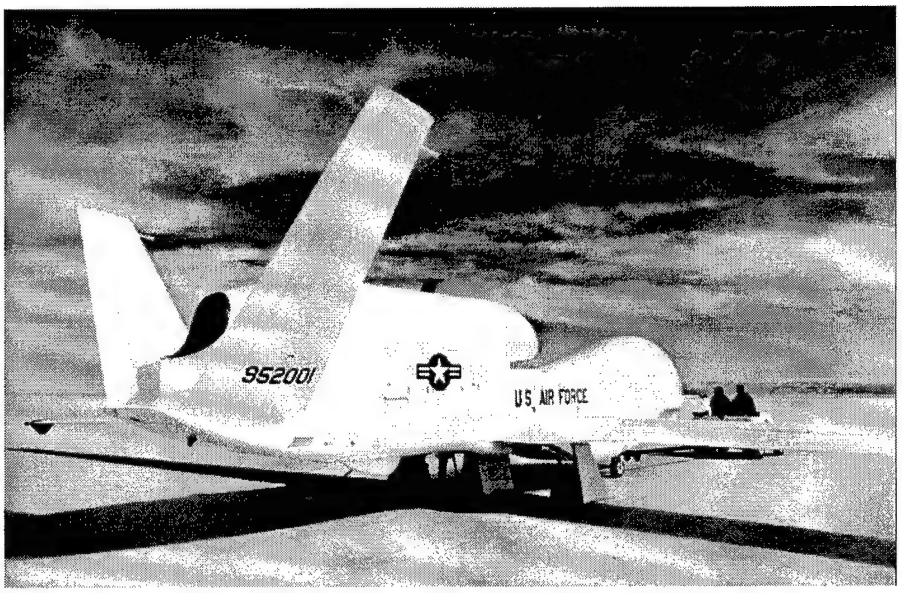

Figure 1.2 HAE Global Hawk on the dry lakebed of Edwards AFB, CA.

The low-observable (LO), high-altitude endurance UAV, Darkstar (Tier III) was designed for low observability and optimized for moderate endurance, high-threat reconnaissance missions in which coverage is more important than range or endurance. It is equipped with either EO or SAR sensors and flies at altitudes greater than 45,000 ft, with on-station flight time of eight hours and a 500 nm operational radius [7]. This program, however, was cancelled in 1998.

There are two tactical reconnaissance UAVs in the current Army and Navy inventory. The Hunter is a short-range UAV operated by the Army, and is designed for a maximum altitude of 15,000 ft with a maximum range of 144 nm. The on-station endurance is 11.6 hours. The Pioneer is a short-range, ship-launched tactical UAV operated by the Navy. It flies at a maximum altitude of 15,000 ft, to a maximum combat radius of 100 nm and has an on-station endurance of five hours [7].

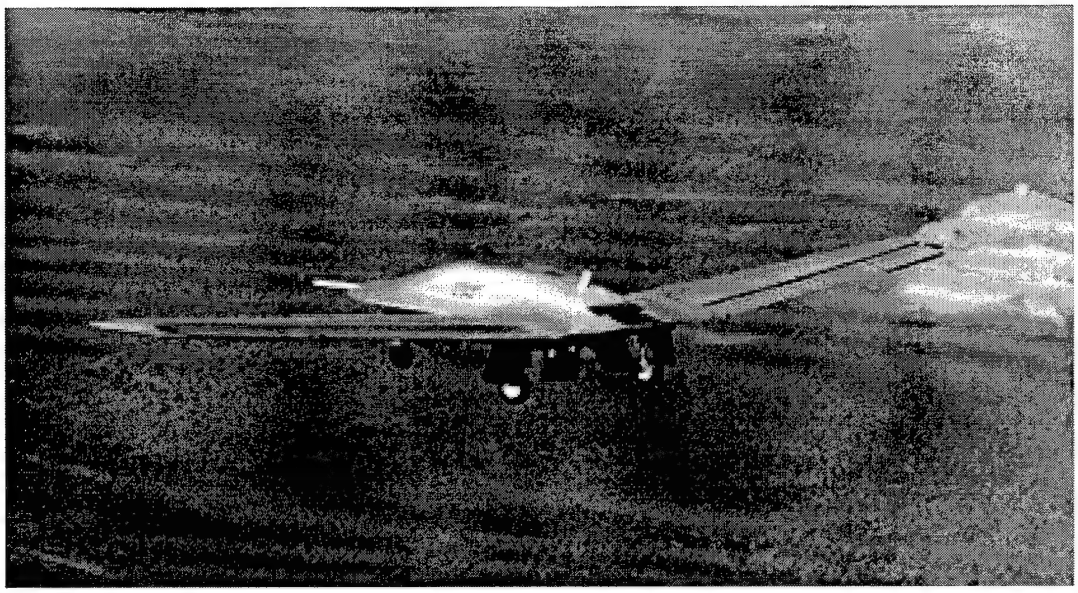

Figure 1.3 LO DarkStar UAV in flight

Only Global Hawk uses jet propulsion (Darkstar was cancelled in 1998), and none employs low-observable (stealth) technology. This factor was a major contributor to losing four Predators (three lost to surface-to-air missiles /SAMs/), six Hunters (four lost to SAMs), and four Pioneers (three lost to SAMs) during Operation Allied Force [7]. While fortunately all of these losses were calculated in dollars and not in human lives, the vulnerability of low-flying, non-stealthy UAVs remains a concern. This is why the Air Combat Command (ACC), the Air Force Research Laboratory (AFRL) and the Defense Advanced Research Projects Agency (DARPA) are currently conducting a joint unmanned combat aerial vehicle (UCAV) Advanced Technology Demonstration (ATD) program. In Phase II of the program (Engineering and Manufacturing Development, or EMD of the acquisition process) Boeing will develop two, low-observable technology (stealth) 8,000 lb, tailless, 34 ft wingspan, jet-powered UCAVs [7].

1.1.2 Issues in Low-Observability.

We have seen that most of the tactical UAVs in the Kosovo and Bosnia operations were lost due to enemy fire. We also know that an aircraft's survivability in a hostile environment can be greatly enhanced by employing stealth technology, which reduces the vehicle's radar cross section (RCS) compared to that of a similar category and size of aircraft. There are a number of ways to reduce an aircraft's RCS, among them are the use of radar wave absorbing materials and paints, radar wave directing surfaces, enclosed ordinance, stores or equipment, and hidden surface discontinuities (such as weapons, engines, antennas). In order to reduce the RCS of the aircraft's wing, the structural discontinuities caused by the aerodynamic control surfaces (ailerons, flaps, slats or spoilers) need to be reduced or eliminated. The flight control of the aircraft then will have to be accomplished by adaptive control using adaptive aerodynamic control surfaces. These surfaces (wings, horizontal and vertical tail) will have to be actuated so that they can generate the necessary increase in the lift coefficient required for a particular type of maneuver.

1.1.3 Adaptive Controls.

The idea of using aeroelastic control by deforming lifting surfaces was first implemented by the Wright brothers. They achieved control of the Wright flyer by warping the end of the lifting surfaces by the means of cables and pulleys. This control scheme, however, proved awkward due to the complexity of its design, and was ineffective at higher dynamic pressures due to the relatively primitive nature of the aircraft itself. Today, with more sophisticated tools and materials available, it is possible to realize the benefits of adaptive control, particularly through the use of strain actuation [16]. An adaptive airfoil equipped with strain actuators can then be used for

control by inducing twist, or camber in the wing, rather than using articulated control surfaces [16]. The induced twist and camber can then be regulated to produce the desired aerodynamic forces and moments.

1.2 Induced Strain Actuation

Induced strain actuation is the process by which actuation strain in the elements of a structure induces deformation of the overall structure. One of the most commonly used induced strain actuation methods is piezoelectricity, in which an applied electric field creates strain in the piezoelectric material. Shape-memory metal alloys (SMA), torque-tubes, magnetostrictives, electrostrictives, and piezoelectrics, in particular Lead-Zirconium-Titanate (PZT) piezoceramics have been used as actuators. It has many advantages over other types of actuation because the actuators are easily integrated within the load bearing structures by either bonding it onto the surface or embedding it in the structural element. [10].

A number of studies have been published on the analysis of strain actuation using PZTs as actuators. The majority of the research involved the deflection control of rectangular plates and beams using surface bonded piezoceramic elements. Crawley and Lazarus (1989) have developed analysis techniques for strain-actuated, plate-like adaptive structures, showing that induced strain actuation is an effective means for controlling those structures. The strain actuation was achieved by using composite materials, piezoceramics, and shape memory alloys. Their wind tunnel experiments demonstrated that sufficient static aeroelastic control can be developed using the adaptive structures [15]. Batra (1995) illustrated the use of PZTs as sensors and actuators to control the deflection of the cen-

troid of a rectangular plate subjected to a uniformly distributed load. To analyze the problem they developed a finite element model employing four-noded Lagrangian elements [4]. Crawley and Anderson (1990) modeled induced strain actuation of beam-like components of intelligent structures. They constructed a Bernoulli-Euler beam model of surface bonded, and embedded actuators, that included the extension and bending of the actuator. In order to resolve the uncertainty whether the surface bonded actuator they developed agrees with the Bernoulli-Euler beam model, they constructed a finite element model that included the extension, bending and shear in the actuator structure [8].

Because closed form solutions cannot be found for the majority of induced strain actuation problems, most of the work done with actual aerodynamic control surfaces dealt with the problem experimentally or used approximate solution methods [10]. Forster and Yang (1998) investigated the effects of using piezoceramic actuation in the flutter control of wing boxes. Assuming that the piezoceramic actuation can achieve the desired change in the natural frequency of the wing box, they demonstrated that significant savings in wing structural weight can be achieved [12]. Kudva, et. al. (1996) investigated the static adaptive control of aerodynamic surfaces with embedded shape memory alloys (SMA) providing antagonistic actuation. Their tests at NASA Langley in 1996 demonstrated an 8% increase in lift due to a wing twist of 1.25 deg [14]. Romeo, et. al. investigated the linear and nonlinear angle of twist of rectangular composite laminate torqueboxes, and contrasted the predicted values of twist with experimental results. They found good correlation between the theoretical analysis and the experimental results by considering the effects of the non-linear shear modulus caused by incomplete diagonal shear stress [24].

Relatively few papers approached the problem using direct analytical methods without resorting to finite element methods. The wing structure — composed of spars and skin — is generally modeled as a closed-, single-, or multiple-cell, thin-walled beam section. The torsion of the wing can be analyzed as torsion of the closed section thin-walled beam. Badir (1995) developed a variationally and asymptotically consistent theory in order to predict the static response of anisotropic, thin-walled, two-cell beams subjected to extensional loads, torsion and bending. One of the major advantages of his study was that the displacement field was not assumed a priori, and it emerges as the result of the asymptotic analysis of the shell energy [2]. Libove (1988) generalized the Bredt-Batho formula for doubly-symmetric, anisotropic shells. In order to reduce the complexity of the solution, Libove simplified the problem to circular, and doubly symmetric, high slenderness ratio, bi-convex tubes of unit thickness.

1.3 Scope and Approach

This thesis investigates the possibility of eliminating the articulated ailerons by equipping the aircraft with an adaptive wing that uses piezoceramic torsion actuation for roll control. For this effort, a specific UAV design using conceptual aircraft design methods is developed in order to obtain the wing structural parameters, such as spar heights, torque-box areas and skin thickness. The overall design is used to build a scale model for experimental scattering and RCS testing using the AFRL/SNA RCS evaluation facility. See reference [25] for details on the theoretical RCS computer simulation model and its comparisons with the experimental results. The selected wing design was a thin-walled, closed, three-section, box-beam construction. The shear flow solution for the torsion of

a single-cell, isotropic thin-walled box beam is going to be developed using the Bredt-Batho method. The technique is going to be expanded for the torsion solution of a closed, three-cell, isotropic box-beam. The classical theory will then be generalized to a single-cell isotropic and anisotropic model in order to account for elastic couplings present in modern laminated composite wing designs. To validate the accuracy of the generalized anisotropic solution, the generalized model isotropic result is compared with the Bredt-Batho results. The generalized anisotropic result will be compared to the results obtained by Romeo. To account for the PZT actuator lamina incorporated in the structure, a continuous PZT element was assumed to be embedded in the top and bottom surfaces of the single-cell box beam. The material elastic properties of the PZT-composite element are compared to those of the composite alone construction skin. The angular tip displacement due to torsion is compared to that of the composite only construction beam. The structure is strain actuated by applying an electric field to the PZT actuator lamina, and the generated twist angles will be compared to the angles generated by uniform torsion.

1.4 Overview

The current presented background information on current issues in UAV and low-observable technology. It also provided a review on some of the analytic and experimental work done on the subject of bending and torsion of beams, plates, and aerodynamic surfaces using piezoceramic strain actuation. Chapter II will detail the conceptual design of the proposed low-observable UAV in order to obtain the wing structural parameters, so that the wing structural geometry is based on a specific and realistic UAV design. It will identify the wing torquebox geometric dimensions for one specific gross weight UAV, as

well as those of the simplified torquebox in order to aid in the calculations presented in Chapters III and IV. This chapter will also include several other UAV designs based on maximum gross takeoff weight and wing aspect ratios in order to facilitate possible future extensions of this study to include trade studies of takeoff weight and piezoelectric strain actuation.

Chapter III includes the shear flow solution for the torsion of a closed, single-cell, thin-walled, isotropic box-beam, and the extension of Bredt-Batho theorem to a closed-section, three-cell, isotropic beam. The required applied moment, the resulting shear flows in the individual structural members, and the tip angle of twist is detailed.

Chapter IV derives the generalization of the Bredt-Batho theorem to a fully anisotropic, single-cell, asymmetric, thin-walled box beam through the modification of Libove's solution for the torsional displacement of closed-section, doubly-symmetric, single-cell, circular tubes. To predict the accuracy of the solution, the method is applied to the torquebox geometry, designed in Chapter II, by considering it as an isotropic single-cell beam, and the solution obtained is then compared to that of the isotropic thin-walled beam of Chapter III. The accuracy of the anisotropic torsion model is compared to the values published in reference [24] for the torsion of an anisotropic, rectangular box beam subjected to uniform cross-sectional moments.

Chapter V extends the results of Chapter IV to a fully anisotropic, single-cell, thin-walled box beam with PZT lamina embedded in the center of the top and the bottom skins. The material properties of the PZT-composite will modify the constitutive relations of Chapter IV, and the resulting tip twist angle due to uniform cross-sectional moment

acting on the single-cell box beam will be compared to those calculated from Chapter IV. Piezoelectric strain is then applied to the PZT-composite construction, anisotropic torque-box, and the resulting tip torsional displacement is recorded as a function of applied voltage and substrate lamina angle.

Chapter VI will detail the results obtained from Chapters III through V. Chapter VII will conclude and summarize the work included in this thesis, and will make recommendations as to the direction of further studies or theses on this subject.

II. Conceptual Design of Tactical UAV

I began to realize that there might be something after all to Newton's Laws.

Robert H.Goddard, 1902

2.1 Operational Requirements

The operational requirements for the proposed low-observable UAV were established in order to provide a design that bridges the gap between the high-endurance, high-weight, long-range Global Hawk, and the short-range, light-weight Predator. To establish realistic wing and torque box dimensions, some operational requirements were set, and six baseline UAVs were designed: three different takeoff weights, each with two different aspect ratios. All other design parameters (such as taper ratio, payload to gross weight percentage, etc.) were held constant. The aircraft operational requirements were set as:

- Gross Takeoff Weight of 5,000, 10,000, and 15,000 lb
- Useful Payload of 500, 1,000, and 1,500 lb
- Single-Engine Jet Propulsion
- Wing Aspect Ratio of 10 and 12
- Mission Altitude of 25,000 ft
- Endurance of 10 hours or more
- Range of 2,000 NM, or more
- Use of High Endurance Airfoil NLF(1)0215

2.2 Conceptual Design Philosophy

During conceptual design the engineer uses approximations to initially estimate the aircraft structural parameters and performance. For the initial estimates, conceptual design equations are used, which in turn are iterated until the required design parameters are satisfied. More iterations can improve the design, but they also considerably increase the time and level of effort required to achieve the required performance and structural parameters. The purpose of the designs for this study was to obtain structural as well as performance parameters that are realistic to the given applications at hand, and not necessarily to design an aircraft that is ready to fly. In the case of the design of a complete aircraft, the conceptual design is followed by the phases of preliminary, then detailed design. These phases further refine the performance and structural parameters by considering the effects of subsystems (cargo, engine size, landing gear fitting, etc.) on the overall design of the aircraft, and by considering the fulfillment of civilian (Federal Aviation Regulations or FARs set by the Federal Aviation Administration) or Military Standards (MILSTDs). For more detailed information about conceptual, preliminary and detailed aircraft design, the interested reader is referred to reference [22].

2.3 Initial Aircraft Sizing

The initial sizing of the low-observable, tailless, single-engine, jet UAV was proposed in order to facilitate the manufacturing of a scaled model to be used as part of comparative RCS study, as well as part of studying actuated wing torsion. The initial sizing was carried out in order to provide approximate aircraft structural data that is suitable for the purposes

Table 2.1 **Design Parameters**

Range (nm)	2,000	Wing Dihedral Angle (deg)	2
Endurance (hr)	10	Specific Fuel Consumption (SFC)	0.4
Aspect Ratio (AR)	12	Payload (W_{pl})(lb)	500
Taper Ratio (λ)	0.40	Fuel Weight Fraction (Wr_f)	0.45
Wing Thickness Ratio (t)	0.15	Empty Weight Fraction (Wr_e)	0.45
Cruise Speed (kts)	180	Pre-Flight Fraction (fr_1)	0.97
Stall Speed (kts)	80	Climb Weight Fraction (fr_2)	0.985
Oswald Efficiency (e)	0.8	Cruise Weight Fraction (fr_3)	0.870

of these studies, and it was not needed to be further refined by the methods of preliminary and detailed aircraft design. Therefore, only two sets of iterations were performed resulting in sufficiently accurate numbers for the purpose of the study.

2.3.1 Design Parameters. In order to achieve the desired performance, several conceptual structural ratios and performance factors were assumed based on accepted initial structural sizing ratios. Two aspect ratios (AR) of 10 and 12 were set, and an Oswald efficiency factor (which accounts for the span efficiency due to the non-elliptical lift distribution, as well as for the variations of the parasite drag with lift) of 0.80 was chosen for the low-speed, high L/D, low-wing aircraft configuration. The fuel-to-gross weight (FGW) ratio of 0.45 was assumed on the basis of FGW ratio of 0.35 of light business jets over 12,000 lb gross takeoff weight (GTW). The empty-to-gross weight (EGW) ratio of 0.45 was assumed on the basis of extensive composite structure, and the EGW of 0.55 of all-metal construction, light business jets over 12,000 lb GTW. The specific fuel consumption (SFC) of 0.4 was assumed on the basis of older, less efficient engines SFC of 0.5-0.6. Further refinement and optimization of these parameters via preliminary and detailed design is suggested as topic of future research. The design parameters are shown in Table (2.1). Using the design parameters and the aircraft weight fractions from Table (2.1), the various

aircraft and fuel weights can be calculated:

$$W_g = Gross\ Weight = \frac{W_{pl}}{1 - Wr_e - Wr_f} \tag{2.1}$$

$$W_e = Empty\ Weight = Wr_e W_g \tag{2.2}$$

$$W_f = Fuel\ Weight = Wr_f W_g \tag{2.3}$$

$$W_1 = Preflight\ Weight = fr_1 W_g \tag{2.4}$$

$$W_2 = Climb\ Weight = fr_2 W_1 \tag{2.5}$$

$$W_3 = Cruise\ Weight = fr_3 W_2 \tag{2.6}$$

2.3.2 Aerodynamic Data. The initial design calculated the wing surface area required for the given cruise conditions in standard atmosphere by accounting for the fuselage form (lift) factor F, the decrease of lift-curve slope due to compressibility (Mach) effects, finite wing and wing sweep effects, and the reduction of wing area by the fuselage. The wing area for the given stall speed was calculated and was found to be greater than that required for the cruise conditions. Because high-lift devices such as leading edge

Table 2.2 **Aerodynamic Data for NLF-0215 Airfoil**

C_{lmax}	1.7	a_0 (1/rad)	2π
α_{stall} (deg)	13	α_{0L} (deg)	-5.0
α_i (deg)	0	c_d	0.008

slats or slotted flaps are not considered due to the low RCS considerations, the wing area necessary for the slow flight (stall condition) was selected for the design. Although wing twist (wash-out) improves on the stall characteristics of an aircraft with tapered wings, this design did no select twist (as a function of span) in order to simplify the modeling of the RCS, ease of manufacturing, and simplified torsion. The aerodynamic data obtained from published airfoil data for the high-altitude, long endurance NLF(1)0215 airfoil are listed in Table (2.2), where C_{lmax} is the maximum profile (2-D) lift coefficient, α_{stall} is the profile (2-D) stall angle of attack (AOA), α_i is the wing incidence angle (arbitrarily set), a_0 is the profile (2-D) lift-curve slope, α_{0L} is the profile zero-lift AOA, and c_d is the 2-D profile drag coefficient at α_{0L}. Using these parameters, the approximate finite wing (3-D) lift-curve slope a_w, the Mach number correction factor β, and the lift curve slope corrected for compressibility effects η can be calculated via Eqns. (2.7) through (2.9).

$$a_w = \frac{ARa_0}{AR + \frac{2AR+4}{AR+2}} \tag{2.7}$$

$$\beta = \sqrt{1 - M_{cr}^2} \tag{2.8}$$

$$\eta = \frac{a_0 \frac{180}{\pi}}{2\frac{\pi}{\beta}} \tag{2.9}$$

Table 2.3 **Structural Reference Values**

Reference Wing Span, b_{ref} (ft)	42
Reference Wing Sweep, $\Omega_(ref)$ (rad)	$4.08 \cdot 10^{-3}$
Reference Wing Area, S_{ref} (ft^2)	151
Exposed Wing Area Ratio, Ratio	0.825
Fuselage Width, W_{fuse} (ft)	$\frac{1}{7}b_{ref}$
Maximum Wing Lift Coefficient, C_{Lmax}	1.52

2.3.3 Reference Parameters. In order to be able to continue with some of the performance parameter calculations, it was necessary to set some of the structural and performance parameters as reference parameters. These values were then updated through repeated iterations until the desired convergence was obtained. The reference values necessary for the further steps in the design are listed in Table (2.3). These reference values were used in calculating the fuselage form (lift) factor F, the lift curve slope for the entire aircraft a_w, the aircraft cruise lift coefficient $C_{Lcruise}$, the cruise wing loading L_w, and the total wing surface required for cruise, S_{cruise}. These were calculated using

$$F = 1.07\left(1 + \frac{W_f}{b_{ref}}\right)^2 \tag{2.10}$$

$$a_w = \frac{2\pi AR}{\sqrt{4 + \left(\frac{AR^2\beta^2}{\eta^2}\right)\left(1 + \frac{(tan(\Omega_{ref})^2}{\beta^2}\right) + 2}} \frac{S_{exp}}{S_{ref}} F \frac{\pi}{180} \tag{2.11}$$

$$C_{Lcruise} = a_w(\alpha_{cruise} - \alpha_{0L}) \tag{2.12}$$

$$L_w = \frac{1}{2} \cdot \rho \cdot v_{cr}^2 \cdot C_{Lcruise} \tag{2.13}$$

$$S_{cruise} = \frac{W_g}{L_w} \tag{2.14}$$

where ρ is the air density at mission altitudes, and S_{exp} is the exposed wing surface area not covered by the fuselage, given by

$$S_{exp} = Ratio \cdot S_{ref} \tag{2.15}$$

The wing area for cruise (S_{cruise}) obtained from Eqn. (2.14) will be compared to the wing area calculated from stall conditions.

2.3.4 Wing Area. Now that some of the structural as well as some of the aerodynamic performance parameters were determined for cruise conditions in Section 2.3.3, the same were calculated for stall speed at standard sea level conditions. The values obtained in this present section were then substituted into the reference values of Section 2.3.3, and were iterated. For the stall conditions at sea level, the wing loading, wing surface, wing span, wing chord lengths as well as thickness at the root and the tip, wing sweep angle, and the maximum lift coefficient due to the wing sweep were calculated:

$$L_w = \frac{1}{2} \cdot \rho_0 \cdot v_{cr}^2 \cdot C_{Lmax} \tag{2.16}$$

$$S_{stall} = \frac{W_g}{L_w} \tag{2.17}$$

$$b = \sqrt{AR \cdot S_{stall}} \tag{2.18}$$

$$c_{root} = \frac{2S}{b(1+\lambda)} \quad c_{tip} = \lambda \cdot c_{root} \tag{2.19}$$

$$t_{root} = t \cdot c_{root} \quad t_{tip} = t \cdot c_{tip} \tag{2.20}$$

$$\Omega = atan\left(\frac{2 \cdot c_{root}}{b}\right) \tag{2.21}$$

$$C_{Lmax} = 0.9 \cdot C_{lmax} \cdot cos(\Lambda) \tag{2.22}$$

where t is the wing profile thickness from Table (2.1), the factor 0.9 in Eqn. (2.22) is the generally accepted scaling factor, and Λ is the quarter-chord sweep angle given by

$$\Lambda = atan\left[3\frac{(1-\lambda)c_{root}}{2b}\right] \tag{2.23}$$

Using the values obtained from Eqns. (2.16) through (2.23), we can define the reference values for the exposed wing area S_{exp} and the parameter *Ratio*, discussed in Section 2.3.3. These were calculated by

$$x = \frac{b}{14}tan(\Omega) \tag{2.24}$$

$$c_{fuse} = c_{root} - 2x \tag{2.25}$$

$$S_{cov} = 2\left[\frac{1}{2}(c_{fuse} + c_{root})\frac{W_{fuse}}{2}\right] \tag{2.26}$$

$$S_{exp} = S - S_{cov} \tag{2.27}$$

$$Ratio = \frac{S_{exp}}{S} \tag{2.28}$$

where x is the decrease in the chord length due to the effects of the wing taper, c_{fuse} is the wing chord length at the fuselage-wing connection, S_{cov} is the wing area covered by the fuselage, S_{exp} is the exposed wing area not covered by the fuselage, and finally the parameter called *Ratio* is the value used in the initial calculations in Section 2.3.3.

2.3.5 Drag and Power Required. In order to calculate the endurance and range of the aircraft, the drag and power required at various flight phases and conditions must be determined. The results can also be used during the preliminary, then detailed design to narrow the selection of suitable engines, and later to select the appropriate engine for the aircraft as well as for the mission. To find the drag estimate during cruise and stall, we calculate the lift coefficients for both conditions. The drag coefficient estimate at cruise and at stall will be the sum of the parasitic and induced drag coefficients. The drag

coefficient at cruise is given by

$$C_{Dcruise} = C_d + \frac{C_{Lcruise}^2}{\pi e AR} \tag{2.29}$$

where e is the Oswald efficiency factor (see Section 2.3.1) and AR is the wing aspect ratio. The cruise lift coefficient in Eqn. (2.29) is given by

$$C_{Lcruise} = \frac{2W_2}{\rho v_{cr}^2 S} \tag{2.30}$$

Then, the drag estimate at cruise is obtained from

$$D_{cruise} = \frac{1}{2}\rho v_{cr}^2 C_{Dcruise} S \tag{2.31}$$

In unaccelerated, straight and level flight, the drag is equal to the thrust required. The power required is calculated by multiplying the drag (thrust required) by the cruise velocity.

$$P_R = D_{cruise} v_{cr} = T_R v_{cr} \tag{2.32}$$

The drag, thrust and power required for stall conditions can be readily calculated using Eqns. (2.29) through (2.32). For stall conditions, the values of C_{Lmax}, and $C_{Dcruise}$ are substituted, wherever appropriate.

2.3.6 Range and Endurance. For a jet powered aircraft, the specific fuel consumption (SFC) is defined as the weight of fuel consumed per unit thrust per unit time [13]. Because the fuel consumption of a jet airplane depends on the thrust produced by

the engine, the SFC for a jet airplane is defined as the thrust specific fuel consumption (TSFC), denoted by c_t. With the assumption that c_t is constant in time, for the endurance of the jet-powered aircraft we get :

$$E = \frac{1}{c_t}\frac{C_L}{C_D} ln\left(\frac{W_g}{W_3}\right)\left(\frac{1}{3600}\right) \tag{2.33}$$

Naturally, the lift and drag coefficients are for cruise conditions, W_g, and W_3 are as defined in Section 2.3.1. The division by 3600 was used to obtain the endurance in the customary units of hours, rather than seconds. For the background and the derivation of Eqn. (2.33), the interested reader is referred to reference [13].

The range of the jet powered aircraft is calculated from the modified Breguet range formula (see reference [13]). Assuming constant c_t, C_L, C_D, and ρ at cruise speed and conditions we have

$$R = 2\sqrt{\frac{2}{\rho S}}\frac{1}{c_t}\frac{C_L^{1/2}}{C_D}(W_g^{1/2} - W_3^{1/2})\frac{1}{6076} \tag{2.34}$$

Naturally, the lift and drag coefficients are for cruise conditions, W_g, and W_3 are as defined in Section 2.3.1. The division by 6076 was used to obtain the range in the customary units of nautical miles rather than units of feet.

2.3.7 Initial Sizing Summary. The initial sizing did not account for the loss of lift and increased drag due to the downforce generated by the longitudinal control surfaces (horizontal tail, and trailing edge elevator); the additional drag generated by the fuselage, or the lift lost due to positive dihedral and wing in-flight bending; the change

Table 2.4 **Initial Sizing Results**

Aircraft Parameter	Value	Aircraft Parameter	Value
W_g (lb)	5000	b(ft)	42.66
W_e (lb)	2250	c_{root} (ft)	5.08
W_f (lb)	2250	c_{tip} (ft)	2.03
W_1 (lb)	4850	Ω (deg)	13.39
W_2 (lb)	4780	$C_{Lmaxsweep}$	1.52
$a_{w\ wing}$ (1/deg)	0.09796	Λ(deg)	6.12
β	0.95	x (ft)	0.73
η	0.99	c_{fuse}	3.63
F	1.3976	S_{cov} (ft^2)	26.53
$a_{w\ a/c}$ (1/deg)	0.1108	S_{exp} (ft^2)	125.16
$C_{Lcruise}$	0.77	Ratio	0.82509
$L_{wcruise}$ (lb/ft^2)	38.19	$C_{Dcruise}$	0.0216
S_{cruise} (ft^2)	130.93	D_{cruise} (lb)	161.09
S_{exp} (ft^2)	125.16	P_R	48900
L_{wstall} (lb/ft^2)	32.96	E (hr)	13.73
S_{stall} (lb/ft^2)	151.69	R (nm)	2410

in the maximum lift coefficient due to the increase in the Reynolds number (Re). The initial sizing neither calculated, nor attempted to achieve any stability derivatives. As it was pointed out earlier, preliminary and detailed design must take these variables into consideration. Not accounting for these factors in the conceptual design phase does not reduce the validity of the model intended to be used in the proposed studies.

The results of the initial sizing after two sets of iterations are now summarized in Table (2.4). These values are presented for the 5,000 *lb* gross takeoff weight air vehicle.

2.4 Wing Sizing

2.4.1 Air Loads Estimates. The modeling of the system of aerodynamic loads acting on the aircraft at any given flight phase and atmospheric condition becomes increasingly complicated as our demand for accuracy grows. To develop a true represen-

tation of the acting forces and moments, extensive finite element packages (NASTRAN, ASTROS, PATRAN) are commercially available. However, for conceptual design purposes, calculating the forces and moments even to sliderule accuracy was more than adequate. As it was stressed before, this would not be satisfactory if prototyping is imminent. Preliminary and detailed design must address the loads more accurately. For initial structural sizing, however, the aerodynamic loads (forces and moments) acting on the wing can be closely approximated by the sum of distributed forces acting as point loads and concentrated moments. Therefore, the maximum lift force (vertical shear) is closely approximated by the expression

$$L = (FS)(LLF)W_g \tag{2.35}$$

where the variable FS is the Factor of Safety, and LLF is the Limit Load Factor. The FS is commonly set to FS=1.5 for manned, and FS=1.2 for unmanned aerial vehicles. The LLF (also abbreviated by n) is commonly set to n=3.8 for normal category, n=4.4 for utility, n=6.0 for aerobatic, and n=2.5-3 for transport category aircraft. Fighter aircrafts draw their own mission specialized LLF requirements. For definitions on aircraft categories, please refer to reference [22]. The maximum bending moment acting on the wing will be conceptually modeled as

$$M = \frac{L}{2}\frac{b}{4} \tag{2.36}$$

where L is obtained from Eqn. (2.35), and b is the wingtip to wingtip span. It is important to note while sizing the spars and the skin, that one wing carries only one half of L calculated from Eqn. (2.35).

2.4.2 Spar Web Sizing. In order to properly size the main and the rear spar of the wing, a location of 25%, and 70% were chosen respectively. The selection of the 25% chord location of the main spar followed the generally accepted practice, since the pitching moment about the quarter chord of the airfoil is independent of the angle of attack. The 70% chord location of the rear spar was chosen as to lessen the section's torsional stiffness by locating the two spars as close as practically acceptable. It was initially assumed that the main spar and the rear spar will carry 2/3 and 1/3 of the shear load respectively. A factor of safety (FS) of 1.2 was designated following the general practice for unmanned, low maneuverability vehicles. A limit load factor (LLF) of 2.5 was set, in the effort of designing the structure for a maximum of 2.5 g load factor. Finally, it was assumed that the main spar and the rear spar should carry 2/3 and 1/3 of the bending moment, respectively.

As a general procedure, the structural components were sized and then evaluated for over-, or underdesign by evaluating the margin of safety (MS). The MS is given by

$$MS = \frac{CriticalLoad}{ActualLoad} - 1 \tag{2.37}$$

where the critical load is the appropriate maximum shear, compressive or tensile force, or bending moment allowed to be acting on the member (driven by material properties). The actual load is the corresponding actual maximum load designed to be acting on the structure.

In aircraft wing spar analysis it is commonly assumed that the spar caps absorb all of the bending stress, and the web (that is extended to the full depth of the spar) carries all of the shear [22]. The actual load situation is (as always) somewhere in between; however, for conceptual design purposes, these assumptions are more than sufficiently accurate. It is also assumed that the shear is constant within the web, and therefore, the maximum shear stress equals the average shear stress. The thickness of the main spar web was determined using reference [21]. Using the maximum design load L_1, we have

$$t_{web1} = \frac{3}{2} \frac{L_1}{\tau_{smax} h_1} \tag{2.38}$$

where L_1 is the maximum load on the main spar, τ_{smax} is the maximum shear stress allowed (material properties), and h_1 is the height of the main spar web (given by profile parameters). The spar web will fail in buckling long before the actual material maximum shear stress is reached. In order to account for the critical shear buckling stress F_{scr}, the shear web buckling parameter K, and web aspect ratio r_{web} (a/b in reference) was selected from reference [22]. The critical shear buckling stress is given by

$$F_{scr} = KE \left(\frac{t_{web1}}{h_1} \right)^2 \tag{2.39}$$

where E is the material's Young's modulus. The actual shear stress in the spar web is calculated by

$$F_{sact} = \frac{L_1}{h_1 t_{web1}} \tag{2.40}$$

Table 2.5 **Spar Web Sizing**

Parameter	Main Spar	Rear Spar
Web Height (in)	8.4334	5.3035
Web Thickness (in)	0.072	0.049
Web Aspect Ratio, a/b	1.5	1.5
Shear Web Buckling Parameter, K	11	11
Area Moment of Inertia (in^4)	3.599	0.609
Critical Buckling Stress (psi)	8338	9765
Actual Stress (psi)	8234	9620
Margin of Safety	0.013	0.015

Then, as discussed above, the MS of the web is given by substituting Eqns. (2.39) and (2.40) into Eqn. (2.37), that is

$$MS_{web1} = \frac{F_{scr}}{F_{sact}} - 1 \tag{2.41}$$

The same procedure is repeated for the rear spar with the appropriate values of the maximum design load and spar height. Initially, the web thickness underestimated the required thickness. After evaluating the critical buckling load, a few iterations are necessary in order to obtain a mandatory positive margin of safety. In designing weight critical structures (such as aircraft), a 1-5% MS subject to the actual application at hand is generally accepted. For the main spar and rear spar, the MS was calculated to be 1.3%, and 1.5% respectively. The calculated values from Eqns. (2.38) through (2.41), including the values for the rear spar as well, are shown in Table (2.5).

2.4.3 Spar Cap Sizing. The spar caps are usually equal, or unequal length angle sections bolted (or riveted) onto the ends of the spar webs. Their purpose is to carry the bending loads (as was discussed in Section 2.4.2) and to provide attachment surface for securing the wing skin. The procedure for selecting the appropriate angle section was

to iteratively evaluate the necessary area moment of the spar (web and caps), and check whether it satisfies the required area moment of inertia calculated from the engineer's theory of bending (see reference [21]). The required moment of inertia for bending is

$$I_{req} = \frac{M}{\sigma_{max}} y \tag{2.42}$$

where M is the maximum bending moment acting on the spar, σ_{max} is the maximum material stress allowed, and y is the maximum distance from the web centerline to the top of the web. The combined area moment of inertia for the spar is given by

$$I_{spar} = I_{caps} + I_{web} \tag{2.43}$$

where the area moment of inertia for the caps (all four) is calculated using the parallel axis theorem

$$I_{caps} = 4[I_{angle} + A_{angle}(y - y_{angle})^2] \tag{2.44}$$

The angle properties must be iterated (different angle sections selected) until the inequality

$$I_{req} < I_{spar} \tag{2.45}$$

is satisfied.

Table 2.6 **Spar Cap Sizing**

Parameter	Main Spar	Rear Spar
Unequal Length Angle Section	3x2.5x3/16	3x2.5x3/16
Angle Section Area (in^2)	0.996	0.996
I_{angle} (in^4)	0.907	0.907
y_{angle} (in)	0.888	0.888
Angle thickness (in)	3/16	3/16
Radius of Gyration (in)	0.954	0.954
I_{caps} (in^4)	47.77	16.02
I_{spar} (in^4)	51.37	16.63
I_{req} (in^4)	44.97	14.14

The same procedure was repeated for both spars, and the angle sections were iterated until the inequality of Eqn. (2.45) was satisfied. The final selection of caps for both spars are shown in Table (2.6).

2.4.4 Skin Sizing. The theory of shear flows will be reviewed in Chapter III, Section 3.1.1. In the following discussion, it will be assumed the reader is familiar with the theory of shearflows, as well as the associated stresses and stress resultants. Also, reference [20] is a good resource for the following discussion.

To approximate the geometry of the torquebox, and to calculate the moment of inertia about the horizontal axis, the average skin length l_{ave}, and average spar height h_{ave} is calculated.

$$l_{ave} = \frac{l_{21}}{l_{22}} \tag{2.46}$$

$$h_{ave} = \frac{h_1}{h_2} \tag{2.47}$$

where l_{21} and l_{22} are the top and bottom skin lengths of the torquebox respectively, h_1 and h_2 are the main and rear spar heights, respectively. By summing the shearflow contributions all around the perimeter we get

$$q_{ij} = q_{(i-1,j-1)} + \frac{L}{2I} A_{cap} \frac{h_1}{2} \tag{2.48}$$

where q_{ij} is the shearflow in the different sections of the box beam, and L is the moment arm of the acting vertical shear (assumed acting at the geometric center of box the beam). The shear flow q_0 in the spar web can also be easily and very accurately approximated by

$$q_0 = \frac{T + 2A_0 q_1}{2A_0 + 2A_0} \tag{2.49}$$

where T is the acting moment due to the vertical shear, and A_0 is one half the enclosed area of the box beam. Because uniform torsion assumes the cross section is sufficiently braced against cross sectional deformation and warping, the rib spacing and skin panel aspect ratio (a/b) must be accounted for. Using the guidelines from reference [22], the shear buckling parameter K, and skin panel aspect ratio a/b is selected to be

$$K = 11 \quad ; \quad a/b = 1.6 \tag{2.50}$$

The critical shear stress for buckling of the flat skin is again given by Eqn. (2.39), and is supplemented by the critical shear stress for buckling of the curved skin F_{crit} given by

$$F_{crit} = F_{scr} + K_1 E \frac{t_{skin}}{r} \tag{2.51}$$

Table 2.7 **Skin Thickness Sizing**

Parameter	Value
Average Skin Length, l_{ave} (in)	28.536
Average Spar Height, h_{ave} (in)	6.868
Half Area of Torque Box, A_0 (in^2)	98
Area Moment of Inertia, I (in^4)	98.852
Approximate Shearflow, q_1 (lb/in)	271
Radius of Skin Curvature, r (in)	30
Flat Plate Critical Shear Stress, F_{scr} (psi)	4118
Curved Plate Critical Shear Stress, F_{crit} (psi)	5782
Actual Skin Shear Stress, f_s (psi)	5687
Margin of Safety, MS	0.017

where $K_1 = 0.1$ is given as empirical factor, and r is the radius of curvature for the skin panel. The skin shear is then calculated by

$$f_s = \frac{q_1}{t_{skin}} \tag{2.52}$$

where q_1 is the shearflow calculated from Eqn. (2.48), and t_{skin} is the initial guess for the skin thickness. The Eqns. (2.51) through (2.52) must be iterated until

$$F_{crit} > f_s \tag{2.53}$$

The measure of merit is again going to be the margin of safety, calculated by

$$MS_{skin} = \frac{F_{crit}}{f_s} - 1 \tag{2.54}$$

The results of the skin thickness calculations and iterations for the 5000 lb gross takeoff weight UAV are presented in Table (2.7).

2.5 Wing Torque Box Identified

2.5.1 Three-Cell, Thin-Walled Torque Box. In order to facilitate the shearflow calculations of Chapter III, Section 3.1 and Section 3.2, all of the geometric properties of the wing box had to be identified. In order to do this conveniently, a Matlab subroutine called 'AREA' was written to calculate the areas of the first, second, and third closed sections of the three-cell beam. The subroutine is conveniently called by a driver program, to determine the total skin lengths of the nose section, the upper and lower center section, as well as the upper and lower skin lengths of the trailing edge section. The corresponding enclosed areas, A_1, A_2, and A_3 are also calculated. It is also necessary to determine the actual heights h_1, and h_2 of the main and rear spar respectively at their corresponding locations, previously determined in Section 2.4.2. It is important to realize that the height of the main or rear spar is not going to be the actual dimensional distance from the nose multiplied by the profile percent thickness. That would lead to erroneous results. To avoid this, the subroutine INTERP was written, which is used by the subroutine AREA in a two-step iterative linear interpolation scheme in order to accurately locate the positions and calculate the heights of the main and rear spars.

The driver program can also call a subroutine called PLOTPROFILE that will actually draw a picture representation of the NLF(1)-0215F high-altitude, high-endurance airfoil. The airfoil data is stored in the subroutine NLF0215. The subroutines AREA, INTERP, PLOTPROFILE, and NLF0215 are included in Appendix A. The non-dimensional airfoil shape is shown in Figure (2.1). A dimensional plot of the NLF(1)-0215F profile with the wing root as well as at the wing tip is included in Appendix A.

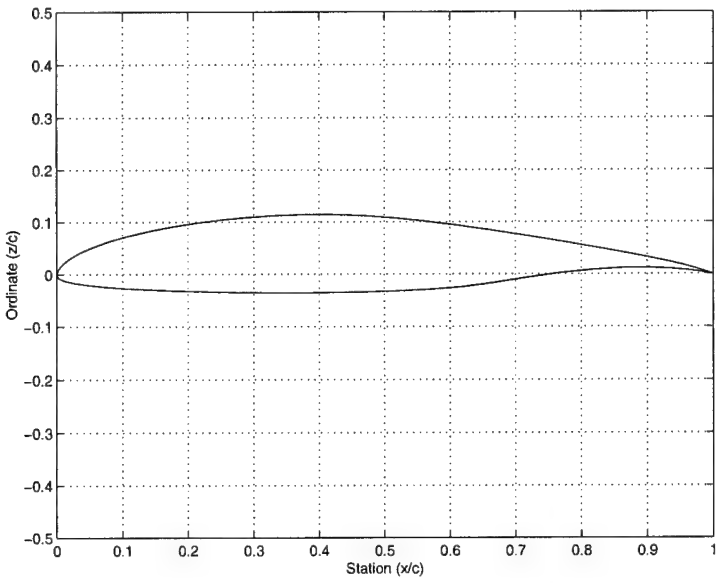

Figure 2.1 The NLF(1)-0215F High-Endurance Airfoil Profile

2.5.2 Simplified, Single-Cell, Thin-Walled Torque Box. Developing the three-cell closed section torque box in Section 2.5.1 will aid in the calculations of shear flows, torques, and twist angles in Chapter III. The development of a more general solution in Chapter IV would not have been possible without a simplified geometric representation of the center, closed-section, single-cell torque box (with area A_2). This is due to the fact that the mathematical representation of the curvatures of the upper and lower surfaces of A_2 are not practical to obtain for the purposes of the calculations that follow. Because the length of the torque box ($c_{root} = c_r$) is much greater than its maximum thickness ($t_r = 0.15c_r$), and the radius of curvature of both the bottom and top surfaces (l_{21}, and l_{22}) of the single-cell center section are much greater than 1 ($r >> 1$), it is reasonable to approximate these surfaces with straight lines.

Though the lengths l_{21} and l_{22} are not equal to each other (as it was determined from the subroutine AREA), their difference $l_{21} - l_{22}$ is much less than the length of the

torque box; therefore, it will be estimated that

$$d = \frac{1}{2} c_r (c_2 - c_1) \tag{2.55}$$

where c_r is the chord length of the wing root, c_1 is the percent chord location of the main spar ($c_1 = 0.25c_r$), c_2 is the percent chord location of the rear spar ($c_2 = 0.75c_r$), and d is the calculated half-distance between the main and the rear spars. Because $h_1 \neq h_2$, the path-length correction factor T was found that will relate the actual lengths of the top and bottom surfaces to the horizontal half-distance (d) between the spars. Using the Pythagorean theorem we get

$$T = \sqrt{1 + \left(\frac{h_2 - h_1}{4d}\right)^2} \tag{2.56}$$

With all this information already at hand, the simplified geometry of the single-cell, closed section center torque box of the 5000 *lb* gross takeoff weight, AR=12 UAV is now identified in Table (2.8). Figure (2.2) shows the simplified single-cell thin-walled torque-box dimensions. The equations for all four surfaces (two skins and two spars) in terms of the path-length coordinate s (that is using $x(s)$, and $y(s)$) will be identified in Chapter IV, Section 4.1.1.

2.6 Design Summary (Aircraft baseline)

After completing the design for the 5000 lb, AR=12 configuration aircraft, the gross weight W_g and the aspect ratio AR of the aircraft was changed, and the process of con-

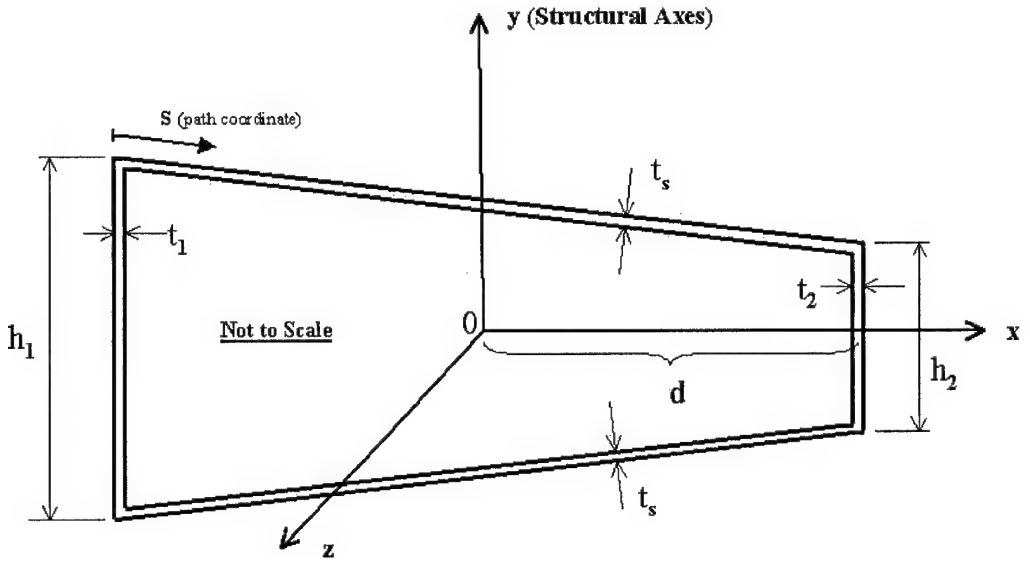

Figure 2.2 Single-cell Torquebox Geometry

Table 2.8 **Simplified Torque Box Dimensions**

Parameter	Value
Main Spar Height, h_1 (in)	8.4334
Rear Spar Height, h_2) (in)	5.3035
Main Spar Thickness, t_1 (in)	0.072
Rear Spar Thickness, t_2 (in)	0.048
Top Surface Length l_{21} (in)	27.7732
Bottom Surface Length l_{22} (in)	29.2992
Skin Thickness, t_s (in)	0.048
Spars Half-Distance, d (in)	13.7160
Path Length Correction Factor, T	1.00162

ceptual design was repeated for the remaining aircrafts using identical design parameters listed in Table (2.1). Six overall designs were accomplished in order to facilitate future weight versus actuation requirements trade studies. The baseline aircraft parameters calculated via the iterative process detailed in Section 2.3 are listed in Table (2.9). The wing structural parameters calculated via the iterative process detailed in Section 2.4 are listed in Table (2.10). Five scale models of the finished design were manufactured by AFIT for the purpose of monostatic RCS testing in the AFRL/SNA facility. The models were

Table 2.9 **Aircraft Baseline Designs**

Gross Weight (lb)	5,000	10,000	15,000	5,000	10,000	15,000
Aspect Ratio	12	12	12	10	10	10
Empty Weight (lb)	2250	4500	6750	2250	4500	6750
L/D	29.66	29.27	28.86	26.36	25.92	25.47
Endurance (hr)	13.7	13.5	13.3	12.18	11.96	11.77
Range (nm)	2410	2643	2801	2143	2341	2473
Wingspan (ft)	42.66	53.04	59.12	39.0	48.48	54.03
Wing Area (ft^2)	151.69	234.46	291.24	151.07	235.05	291.97
Root Chord (ft)	5.08	6.31	7.04	5.57	6.93	7.72
Tip Chord (ft)	2.03	2.53	2.82	2.23	2.77	3.09
Root Thickness (ft)	0.76	0.95	1.06	0.84	1.04	1.16
Tip Thickness (ft)	0.30	0.38	0.42	0.33	0.42	0.46

Table 2.10 **Wing Structure Baseline Designs**

Gross Weight (lb)	5,000	10,000	15,000	5,000	10,000	15,000
Aspect Ratio	12	12	12	10	10	10
l1(in)	31.5955	39.2456	43.7859	34.6431	43.1018	48.0153
l21 (in)	27.7732	34.4978	38.4889	30.4521	37.8875	42.2065
l22 (in)	29.2992	36.3933	40.6036	32.1253	39.9692	44.5256
l31 (in)	18.6520	23.1681	25.8484	20.4511	25.4445	28.3451
l32 (in)	17.4096	31.6249	24.1267	19.0888	23.7497	26.4571
h_1 (in)	8.4334	10.4754	11.6873	9.2469	11.5047	12.8161
h_2 (in)	5.3035	6.5876	7.3497	5.8151	7.2349	8.0597
A_1 (in^2)	91.9370	141.8475	176.5664	110.5282	171.0918	212.3232
A_2 (in^2)	229.1889	353.6102	440.1609	275.5348	426.5133	529.2986
A_3 (in^2)	38.5871	59.5351	74.1071	46.3900	71.8093	89.1146
t_{skin} (in)	0.048	0.058	0.064	0.047	0.056	0.062
t_{web1} (in)	0.072	0.098	0.117	0.075	0.101	0.120
t_{web2} (in)	0.049	0.067	0.079	0.051	0.069	0.082

manufactured with and without articulated ailerons to measure and compare the effects of wing discontinuities on RCS scattering. The fuselage, chime, and wing-body interface were designed by AFRL/SNA using low-observable design code. The results of the test will be compared to the scattering code developed and published in reference [25]. A picture of one finished model is presented in Figure (2.3).

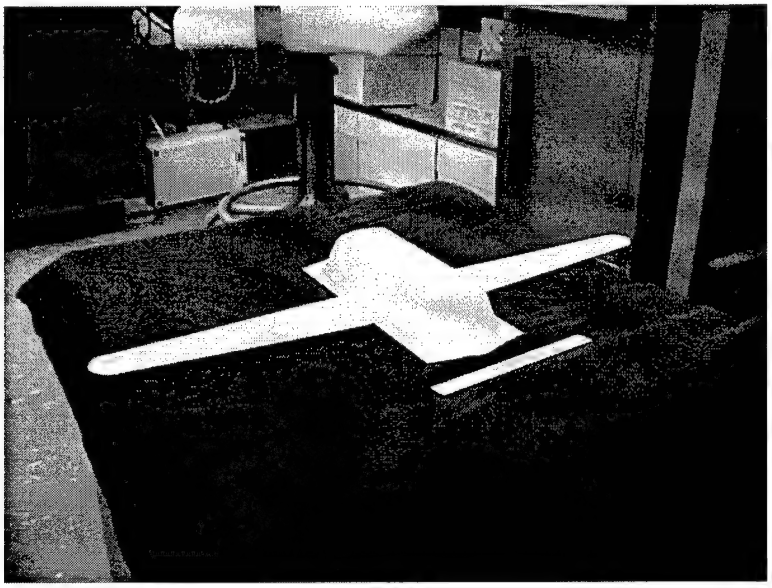

Figure 2.3 Scale Model of Prototype UAV for RCS Testing

III. Torsion of Box Beams

There will be no more accidents!

Gen. Westover, Assistant Chief Air Corps, ordering to stop airmail plane crashes, 1934

3.1 Single-Cell Beam Torsion

3.1.1 Shear Flows in Thin Webs. The shear flow q in a thin-walled structural element is defined as the product of the shear stress σ_s at the thin wall centerline and the thickness t of the element:

$$q = \sigma_s t \tag{3.1}$$

The unit of shear flow is force per unit length. The value of q in a closed, single-cell section subjected to torsion alone is constant along the section, regardless of the thickness t [18]. It is often necessary to obtain the resultant force on a curved web in which the shear flow q is constant along the length of the web. The differential element ds shown Figure (3.1) has horizontal and vertical components dz and dy. The force on this element is qds. The horizontal force F_z is

$$F_z = \int_0^z q\mathrm{d}z = qz \tag{3.2}$$

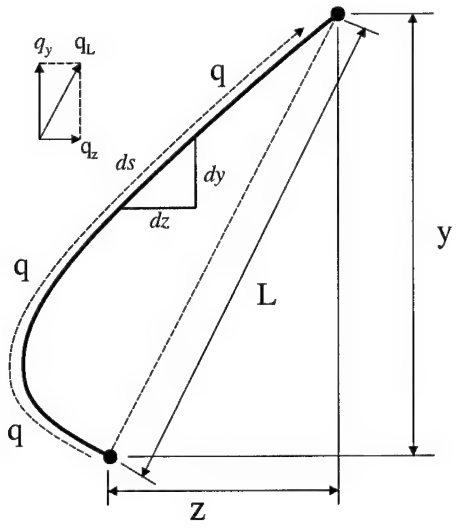

Figure 3.1 Differential Element (Open Section)

where z is the horizontal distance between the ends of the web. The vertical force F_y acting on the element is

$$F_y = \int_0^y q\mathrm{d}y = qy \tag{3.3}$$

where y is the vertical distance between the ends of the web. While Eqns. (3.1) and (3.2) are independent of the shape of the web, the total torsional moment of the resultant force depends on the shape of the web. The induced moment by the shear flow along the web is

$$M = \int_s qr\mathrm{d}s = \int_A 2q\mathrm{d}A = 2q\int_A \mathrm{d}A = 2Aq \tag{3.4}$$

where A is the total area enclosed by the web.

For closed, single-section beams, the constant shear flow q around the circumference of the web has no horizontal or vertical resultant force, since by Eqns. (3.1) and (3.2) the horizontal and vertical distances between the end points of the web are zero. The resultant of the shear flow is a torque (moment) equal to the applied external moment M, taken about an arbitrary axis perpendicular to the cross section. Thus,

$$M = \sum 2(\Delta A)q = 2Aq \tag{3.5}$$

where A represents the total area enclosed by the web.

The angle of twist per unit length of the closed, single-cell web is given by the Bredt-Batho formula for torsional displacement:

$$\theta = \frac{1}{2AG_0} \sum \frac{q\Delta s}{t^*} \tag{3.6}$$

where G_0 is the arbitrarily selected reference shear modulus of one of the structural materials used, and

$$t^* = \frac{G(s)}{G_0} t \tag{3.7}$$

The quantity t^* is the modulus weighted thickness, and $G(s)$ is the shear modulus of the web section. In case of multi-material construction, G is expressed as $G(s)$ because the value of G becomes a function of the circumferential coordinate s. The practical application of the formula implies that there is no warping constraint on the cross section, and it is

adequately stiffened internally against distortion; that is, the shape of the cross section is preserved, neglecting any Poisson's ratio effects [19].

3.1.2 Torsion of the Single-Cell Section.

Revisiting the geometry of the torque-box developed in Chapter II, we can apply the Bredt-Batho formula directly by using Eqn. (3.6). Because the shear flow q is constant around the cross section, and the material properties are identical in all sections of the web, we can derive by inspection the formula for the geometry of the single-cell section:

$$\theta = \frac{1}{2AG_0}\left[\frac{ql_1}{\frac{G_s}{G_0}t_s} + \frac{qh_2}{\frac{G_0}{G_0}t_2} + \frac{ql_2}{\frac{G_s}{G_0}t_s} + \frac{qh_1}{\frac{G_0}{G_0}t_1}\right] \tag{3.8}$$

where l_1 and l_2 are the lengths of the top and bottom skins of the torque box; h_1 and h_2 are the heights of the main and rear spars; t_s, t_1 and t_2 are the thickness of the skin, main, and rear spar, respectively; and G_s and G_0 are the shear moduli of the skin and spars, respectively. Using the known applied moment M, we can solve for q from Eqn. (3.5)

$$q = \frac{M}{2A} \tag{3.9}$$

By factoring out q and substituting Eqn. (3.9) into Eqn. (3.8), we obtain

$$\theta = \frac{M}{4A^2G}\left[\frac{4Td}{t_s} + \frac{h_2}{t_2} + \frac{h_1}{t_1}\right] \tag{3.10}$$

where we used the relation $l_1 \approx l_2 = 2Td$, where T and d are as defined in Chapter II.

In order to automate the calculations of Eqns. (3.9) through (3.10), a Matlab routine was written, and is included in Appendix B. The routine calculates the moment required for, and the shear flow generated by a given angle of twist. The code can be easily modified by interested readers to calculate the angle of twist generated by a given concentrated cross sectional moment, as well as the resulting shear flow.

3.2 Multi-Cell Beam Torsion

3.2.1 Torsion of the Multi-Cell Section. The solution for the torsional displacement of the thin-walled beam developed in Section 3.1 is directly applicable to multi-cell beams. However, sections with multiple cells are statically indeterminate. In order to solve for the angular displacement, we must enforce the condition of continuity of rotation, that is, the angular twist of all the cells must be the same:

$$\theta_1 = \theta_2 = \ldots = \theta_n \tag{3.11}$$

where θ_i is given by the now familiar formula

$$\theta_i = \frac{1}{2A_iG_0}\Sigma\frac{q_i\Delta s}{t^*} \tag{3.12}$$

The modulus weighted thickness t^* is as defined by Eqn. (3.7); however, in order to keep the notation as clutter free as possible, t^* will be substituted using Eqn. (3.7).

In order to solve for the shear flows q_i in the different sections of the multi-cell beam, we must first enforce the continuity condition of Eqn. (3.11). Using the three cells of the beam shown in Figure (3.2), by inspection we can write

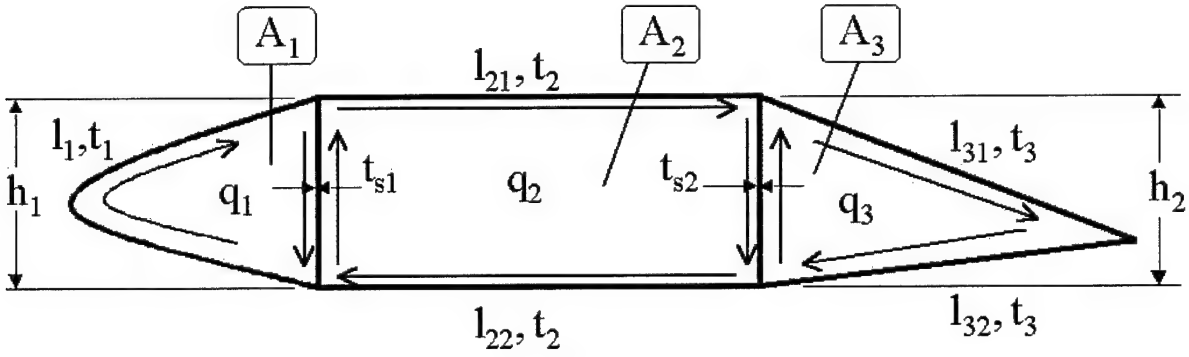

Figure 3.2 Three-Cell Beam (Closed Section)

$$\theta_1 = \frac{1}{2A_1G_0}\left[\frac{q_1 l_1}{\frac{G_s}{G_0}t_1} + \frac{h_1(q_1 - q_2)}{\frac{G_0}{G_0}t_{s1}}\right] \tag{3.13}$$

$$\theta_2 = \frac{1}{2A_2G_0}\left[\frac{q_2 l_{21}}{\frac{G_s}{G_0}t_2} + \frac{h_2(q_2 - q_3)}{\frac{G_0}{G_0}t_{s2}} + \frac{q_2 l_{22}}{\frac{G_s}{G_0}t_2} + \frac{h_1(q_2 - q_1)}{\frac{G_0}{G_0}t_{s1}}\right] \tag{3.14}$$

$$\theta_3 = \frac{1}{2A_3G_0}\left[\frac{q_3 l_{31}}{\frac{G_s}{G_0}t_3} + \frac{q_3 l_{32}}{\frac{G_s}{G_0}t_3} + \frac{h_2(q_3 - q_2)}{\frac{G_0}{G_0}t_{s2}}\right] \tag{3.15}$$

where the structural variables are as defined in Chapter II, t_i are the skin thickness of the corresponding closed section ($i = 1, 2, 3$), and t_{si} is the main and rear spar thickness ($i = 1, 2$) respectively. The variables q_1, q_2, and q_3 are the shear flows in the nose, middle,

and tail sections of the three-cell beam, respectively. Enforcing the continuity condition of $\theta_1 = \theta_2$, and solving for q_1 in terms of q_2 and q_3 we get (after some heavy algebra)

$$q_1 = \frac{\frac{A_1}{A_2}\left[\frac{l_{21}}{G^* t_2} + \frac{h_2}{t_{s2}} + \frac{l_{22}}{G^* t_2} + \frac{h_1}{t_{s1}}\right] q_2 + \frac{h_1}{t_{s1}} q_2 - \frac{h_2}{t_{s2}} q_3}{\frac{l_1}{G^* t_1} + \frac{h_1}{t_{s1}} + \frac{A_1 h_1}{A_2 t_{s2}}} \tag{3.16}$$

Notice that by arbitrarily selecting the spar's shear modulus G as the reference shear modulus G_0, we can use the simplification $G_0/G_0 = 1$ and $G_s/G_0 = G^*$. By enforcing the next continuity condition $\theta_2 = \theta_3$, then by substituting for q_1 using Eqn. (3.16), and solving for q_3 in terms of q_2, we obtain, after some considerable algebra

$$q_3 = \frac{C_1 C_2 - \frac{h_1}{t_{s1}} C_4 - (\frac{h_1}{t_{s1}})^2}{C_2 C_3 + \frac{h_2}{t_{s2}} - \frac{h_1 h_2}{t_{s1} t_{s2}}} q_2 \tag{3.17}$$

where the constants C_1, C_2, C_3, and C_4 are given by

$$C_1 = \frac{l_{21}}{G^* t_2} + \frac{h_2}{t_{s2}} + \frac{l_{22}}{G^* t_2} + \frac{h_1}{t_{s1}} + \frac{A_2 h_2}{A_3 t_{s2}} \tag{3.18}$$

$$C_2 = \frac{l_1}{G^* t_1} + \frac{h_1}{t_{s1}} + \frac{A_1 h_1}{A_2 t_{s1}} \tag{3.19}$$

$$C_3 = \frac{A_2}{A_3}\left(\frac{l_{31}}{G^* t_3} + \frac{l_{32}}{G^* t_3} + \frac{h_2}{t_{s2}}\right) \tag{3.20}$$

$$C_4 = \frac{A_1}{A_2}\left(\frac{l_{21}}{G^* t_2} + \frac{h_2}{t_{s2}} + \frac{l_{22}}{G^* t_2} + \frac{h_1}{t_{s1}}\right) \tag{3.21}$$

We are now ready to solve for q_1 in terms of q_2. Let's name the constant in front of q_2 in Eqn. (3.17) to be S_3. Take Eqn. (3.17) and substitute it into Eqn. (3.16) to get

$$q_1 = \frac{C_4 + \frac{h_1}{t_{s1}} - \frac{h_2}{t_{s2}} S_3}{C_2} q_2 \tag{3.22}$$

Again, let's name the constant multiplying q_2 in Eqn. (3.22) as S_1.

In order to solve for the individual shear flows in the sections, we use the extended version of Eqn. (3.5), that is

$$M = \sum(2Aq_i) = 2A_1q_1 + 2A_2q_2 + 2A_3q_3 \tag{3.23}$$

Because we solved for q_1 and q_3 in terms of q_2, we can substitute Eqns. (3.16) and (3.17) into Eqn. (3.23) while using the convenient constants S_1 and S_3.

$$M = 2(A_1S_1 + A_2 + A_3S_3)q_2 \tag{3.24}$$

From this we can readily obtain the shear flow q_2

$$q_2 = \frac{M}{2(A_1S_1 + A_2 + A_3S_3)} \tag{3.25}$$

where the applied moment M is given by

$$M = G_0J^*\theta = (GJ)_{eff}\theta \tag{3.26}$$

In Eqn. (3.26) the quantity $G_0 J^*$ is called the torsional stiffness of the section, J^* is the St. Venant's constant for uniform torsion given by

$$J^* = \frac{4A^2}{\oint \frac{1}{t^*} \mathrm{d}s} \tag{3.27}$$

Substituting Eqn. (3.7) for the modulus weighted thickness t^* we get

$$J^* = \frac{4A^2}{G_0 \oint \frac{1}{G(s)t(s)} \mathrm{d}s} \tag{3.28}$$

from which we obtain the effective torsional stiffness

$$G_0 J^* = (GJ)_{eff} = \frac{4A^2}{\oint \frac{1}{G(s)t(s)} \mathrm{d}s} \tag{3.29}$$

In order to find the effective torsional stiffness of the three-section beam, we first need to evaluate the effective torsional stiffness of each section. The combined effective torsional stiffness is given by the sum of the individual torsional stiffnesses.

$$(GJ)_{eff_1} = \frac{4A_1^2}{\frac{l_1}{G_s t_1} + \frac{h_1}{G_0 t_{s1}}} \tag{3.30}$$

$$(GJ)_{eff_2} = \frac{4A_2^2}{\frac{l_{21}}{G_s t_2} + \frac{h_2}{G_0 t_{s2}} + \frac{l_{22}}{G_s t_2} + \frac{h_1}{G_0 t_{s1}}} \tag{3.31}$$

$$(GJ)_{eff_3} = \frac{4A_3^2}{\frac{l_{31}}{G_s t_3} + \frac{l_{32}}{G_s t_3} + \frac{h_2}{G_0 t_{s2}}} \tag{3.32}$$

Then the effective torsional stiffness $(GJ)_{eff}$ for the three-cell beam can be calculated by using Eqn. (3.29)

$$(GJ)_{eff} = (GJ)_{eff_1} + (GJ)_{eff_2} + (GJ)_{eff_3} \tag{3.33}$$

We now have arrived at the final solution of the torsion of the three-cell beam section. The required moment (in units of *in-lb*) to generate a given angle of twist θ (in units of radians), and the resulting shear flows (force per unit length, in this case lb/in) can be calculated using the following relations.

$$M = (GJ)_{eff}\theta \tag{3.34}$$

$$q_2 = \frac{M}{2(A_1S_1 + A_2 + A_3S_3)} \tag{3.35}$$

$$q_1 = S_1 q_2 \tag{3.36}$$

$$q_3 = S_3 q_2 \tag{3.37}$$

To automate the calculations of Eqns. (3.5) through (3.37), a Matlab program called SHEARFLOW3CELL was written to calculate the shear flow and moment required to generate a given tip twist angle for the given geometry single-cell, closed-section box beam.

The code was extended to calculate the individual shear flows in the three sections of the closed box beam, as well as the moment required to generate the given tip twist angle. By running the program, a direct comparison can be made between the effectiveness of the single-cell and the three-cell beam in resisting torsional moments. The Matlab program is included in Appendix B.

IV. Generalized Torsion Solution

There will be no more flying!

Maj Byron Q. Jones, Eastern Airmail Zone Commander, responding to Westover, 1934

4.1 Homogeneous Isotropic Single-Cell Beam

4.1.1 Geometry and Loading. While the shear-flow solution of the one, or multi-cell torque box is useful due to its relative simplicity, it only applies to isotropic beams. It also applies to specially orthotropic construction, meaning that at least one of the axes elastic symmetry is parallel to the longitudinal axis of the thin-walled beam [17]. One disadvantage of the method is that it does not account for applied loads other than the applied torque acting on the cross section. Therefore, in this section, we extend the Bredt-Batho theorem by generalizing the method developed by Libove (see ref [17]) and develop an analytical solution for the torsional displacement of the fully isotropic, thin-walled, linearly elastic, single-cell box beam in the presence of a full complement of air loads. The theory assumes that no cross-sectional warping occurs (shape of the cross section is preserved), and that the longitudinal strains vary linearly over the cross section (linearly elastic). In order to evaluate the validity, as well as the accuracy of the solution, in Section 6.1 we will check the isotropic solution against the shear-flow solution developed in Chapter III.

Let this beam segment be subjected to a system of external loads consisting of forces and moments applied at the end center of the cross section as shown in Figure (4.1). These

forces and moment may be the result of applied thrust (longitudinal or vertical), vertical and horizontal shear due to lift and drag respectively, twisting moment due to external stores or strain actuation, as well as bending moment due to lift or structural weight. In

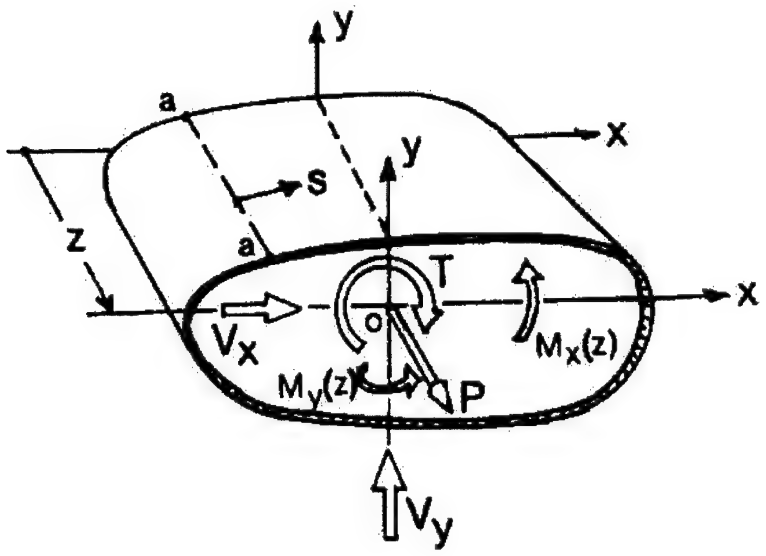

Figure 4.1 Forces and Moments Applied to Closed Section [17]

the actual cross section there may be distributed forces and moments; however, these will be approximated by concentrated forces and moments acting on the section. By taking a differential segment dz of the cross section, the applied loads will be assumed constant within dz, but will be different from one segment to the next. In effect, the spanwise varying loads are approximated by piecewise uniform forces and moments.

For simplicity, only a single cell beam is considered. The beam is assumed anisotropic, so that normal stress at a point tends to generate shear strain (γ) and longitudinal strain (ϵ) as well. The cross-sectional shear flows tend to produce longitudinal strain and shear strain. This interaction between normal stress and shear strains is called elastic coupling.

Before we can start on the solution, we have to establish the cross sectional geometry of the beam, and define the equations of the walls of the section. Establishing the exact geometry of the actual airfoil's center torque box is not an impossible task; however, it would not serve a very useful purpose as it would yield prohibitively lengthy symbolic results throughout the analysis. Therefore, a generalized, simplified geometry is used that approximates the actual geometry of the torque box as a generic trapezoid, defined in Chapter II.

Let the x-y coordinate system be defined with its origin in the geometric center of the trapezoid cross section. In addition, let the s coordinate be defined as the clockwise "path-length coordinate" around the perimeter of the trapezoid, starting from the upper left-hand corner ($s = 0$). Then, it can be shown that for the four sides of the trapezoid torque box we can define $y(s)$ and $x(s)$ as

$$y(s) = \begin{cases} \frac{h_2-h_1}{4dT}(s - Td) + \frac{1}{4}(h_2 + h_1) & : \quad Top\ Side \\ 2Td - s + \frac{1}{2}h_2 & : \quad Right\ Side \\ -\left[\frac{h_2-h_1}{4dT}(3Td - s + h_2) + \frac{1}{4}(h_2 + h_1)\right] & : \quad Bottom\ Side \\ s - 4Td - h_2 - \frac{1}{2}h_1 & : \quad Left\ Side \end{cases} \tag{4.1}$$

$$x(s) = \begin{cases} \frac{s}{T-d} & : \quad Top\ Side \\ d & : \quad Right\ Side \\ 3d - \frac{1}{T}(s - h_2) & : \quad Bottom\ Side \\ -d & : \quad Left\ Side \end{cases} \tag{4.2}$$

The clockwise path coordinate s around the perimeter is piecewise continuous. The discontinuities in $y(s)$ at the respective values of s (at the corners of the trapezoid; see below) also serve as the limits of integrations for all the integrals developed below. For the sake of simplicity, these limits will be abbreviated wherever appropriate by the following definitions. Starting from the upper left-hand corner ($s = 0$), these limits are

$$\begin{aligned} s_1 &= 2dT & s_2 &= 2dT + h_2 \\ s_3 &= 4dT + h_2 & s_4 &= 4dT + h_2 + h_1 \end{aligned} \tag{4.3}$$

4.1.2 Constitutive Relations. In order to arrive at any meaningful and relatively simple solution, the walls of the box beam are assumed to be thin enough, so that they can be viewed as membranes in plane stress ($\sigma_{33} = 0$). In order to keep the solution general, the method will be applied to a torque box made of walls of non-unit thickness. The solution can also be easily modified by interested readers to unit thickness. This can be achieved by simply assuming $t = 1$, thereby eliminating all the wall thickness dependencies in the equations. We can also assume that the normal stress resultant per unit length N_s along the s direction is negligible [17]. This way the state of plane stress can be described for the element as a shear flow q, and a tension flow N, both having units of force per unit depth. Figure (4.2) shows the differential element and the state of stress of the differential element. The normal strain ϵ and shear strain γ (both unitless) are related by the constitutive relations

$$\epsilon = \alpha_1 N \frac{1}{t} + \alpha_2 q \frac{1}{t} \tag{4.4}$$

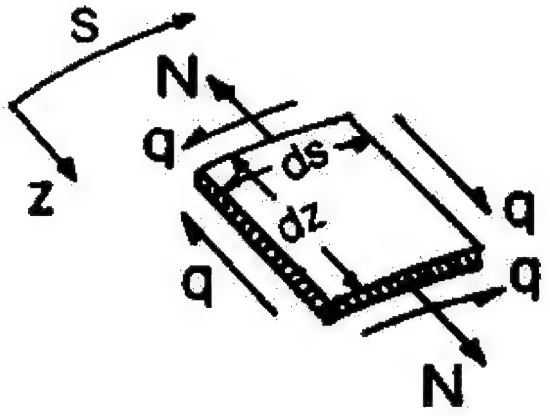

Figure 4.2 State of Stress of Differential Wall Element [17]

$$\gamma = \alpha_2 N \frac{1}{t} + \alpha_4 q \frac{1}{t} \tag{4.5}$$

where t is the wall thickness, and α_1, α_2, and α_4 are elastic constants yet to be defined. We can solve for N and γ by rearranging Eqns. (4.4) and (4.5) to get

$$N = \beta_1 \epsilon \, t + \beta_2 q \tag{4.6}$$

$$\gamma = -\beta_2 \epsilon + \beta_4 q \frac{1}{t} \tag{4.7}$$

where β_i are given by

$$\beta_1 = \frac{1}{\alpha_1} \tag{4.8}$$

$$\beta_2 = \frac{-\alpha_2}{\alpha_1} \tag{4.9}$$

$$\beta_4 = \alpha_4 - \frac{\alpha_2^2}{\alpha_1} \tag{4.10}$$

To determine the elastic constants α_1, α_2, and α_4 we need to write the full anisotropic strain-stress (constitutive) equations for plane stress ($\sigma_{33} = 0$):

$$\epsilon = S_{11} N \frac{1}{t} + S_{12} N_s \frac{1}{t} + S_{14} q \frac{1}{t} \tag{4.11}$$

$$\epsilon_s = S_{12} N \frac{1}{t} + S_{22} N_s \frac{1}{t} + S_{24} q \frac{1}{t} \tag{4.12}$$

$$\gamma = S_{14} N \frac{1}{t} + S_{24} N_s \frac{1}{t} + S_{44} q \frac{1}{t} \tag{4.13}$$

where S is the matrix inverse of the elasticity matrix, called the compliance matrix. By ignoring the transverse strain ϵ_s, setting the transverse tension flow N_s to zero, and comparing with Eqns. (4.4) and (4.5) we get

$$\alpha_1 = S_{11} \tag{4.14}$$

$$\alpha_2 = S_{14} \tag{4.15}$$

$$\alpha_4 = S_{44} \tag{4.16}$$

Therefore, by determining the compliance matrix S for the given material we also determine the coupling elastic constants α_2, and β_2.

4.1.3 Analysis.

4.1.3.1 Preliminary Considerations.

We can establish the differential equations of equilibrium for the differential element

$$\frac{\partial q}{\partial z} = 0 \tag{4.17}$$

$$\frac{\partial q}{\partial s} + \frac{\partial N}{\partial z} = 0 \tag{4.18}$$

From Eqn. (4.17) we can see that the shear flow $q(s)$ is a function of s only. Integrating Eqn. (4.18) we get

$$q(s) = q_0 - \int_0^s \frac{\partial N}{\partial z}\,\mathrm{d}x \tag{4.19}$$

Figure (4.3) represents the differential cross section dz of the single cell beam, indicating the longitudinal shear flow q_0 at $s = 0$, and the differential change in the tension flow N with dz. In the classical theory of isotropic, homogeneous, thin-walled beams, the

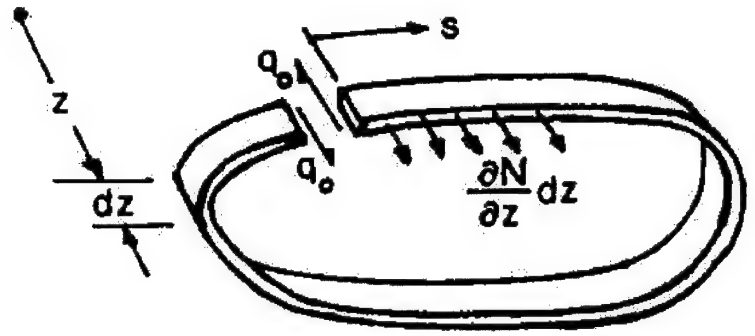

Figure 4.3 Shear Flow and Change in Tension Flow with dz [17]

cross-sectional normal stress is assumed to vary linearly with x and y [17]. That is,

$$\epsilon = \epsilon_0 - yK_x - xK_y \tag{4.20}$$

where ϵ_0, K_x, and K_y are functions of z. This formulation assumes only linear midplane translational strain ϵ_0 in the z coordinate direction, as well as linear curvatures (or also called rotations in some literature) K_x and K_y of the cross section at z around the x and y coordinate axes, respectively. In this way the warping functions are ignored from the displacement formulation that will lead to less accurate answer for the torsional displacement. See reference [1] for accounting for bi-quadratic warping functions and the qualitative improvement they yield in the results. Let's substitute Eqn. (4.20) into Eqn. (4.6) and differentiate with respect to z to get

$$N = \beta_1 t(\epsilon_0 - yK_x - xK_y) + \beta_2 q \tag{4.21}$$

$$\frac{\partial N}{\partial z} = \beta_1 t(\epsilon_0' - yK_x' - xK_y') \tag{4.22}$$

Substituting Eqn. (4.22) into Eqn. (4.19) we get

$$q(s) = q_0 - \int_0^s \beta_1 t(\epsilon_0' - yK_x' - xK_y')\mathrm{d}s \tag{4.23}$$

We can simplify Eqn. (4.23) by declaring

$$q(s) = q_0 - \epsilon_0' a_1(s) + K_x' a_2(s) + K_y' a_3(s) \tag{4.24}$$

where

$$a_1(s) = \int_0^s \beta_1 t \,\mathrm{d}s \tag{4.25}$$

$$a_2(s) = \int_0^s y\beta_1 t \,\mathrm{d}s \tag{4.26}$$

$$a_3(s) = \int_0^s x\beta_1 t \,\mathrm{d}s \tag{4.27}$$

Equations 4.25 through 4.27 are solved individually and consecutively for all four surfaces of the trapezoid, yielding four equations for each $a_i(s)$ equation. Each surface will have its own contribution that is added to the contribution of all surfaces previously evaluated. The method of solving Eqns. (4.25) through (4.27) is demonstrated via $a_1(s)$.

The solution of $a_2(s)$ and $a_3(s)$ follows the same technique.

$$a_1(s)^t = \int_0^s \beta_1 t_s \mathrm{d}s \tag{4.28}$$

$$a_1(s)^r = \int_0^{2dT} \beta_1 t_s \mathrm{d}s + \int_{2dT}^s \beta_1 t_2 \mathrm{d}s \tag{4.29}$$

$$a_1(s)^b = \int_0^{2dT} \beta_1 t_s \mathrm{d}s + \int_{2dT}^{2dT+h_2} \beta_1 t_2 \mathrm{d}s + \int_{2dT+h_2}^s \beta_1 t_s \mathrm{d}s \tag{4.30}$$

$$a_1(s)^l = \int_0^{2dT} \beta_1 t_s \mathrm{d}s + \int_{2dT}^{2dT+h_2} \beta_1 t_2 \mathrm{d}s + \int_{2dT+h_2}^{4dT+h_2} \beta_1 t_s \mathrm{d}s + \int_{4dT+h_2}^s \beta_1 t_1 \mathrm{d}s \tag{4.31}$$

where t_s, t_1, and t_2 are the thickness of the top and bottom skin, the main spar (left side) and rear spar (right side), respectively. The superscripts t, r, b, and l of $a_i(s)$ are for the top, right, bottom, and left sides respectively. To solve Eqns. (4.28) through (4.31) I suggest the use of any symbolic solver algorithms currently available, such as MathCad, Matlab or Mathematica. The symbolic results of Eqns. (4.28) through (4.31) are relatively simple and will not be reproduced here.

4.1.3.2 Equations of Static Equivalence.

At any cross section of the beam, the longitudinal force per unit length N must be statically equivalent to the cross-sectional extension force P, the cross sectional bending moment about the x axis M_x, and the cross sectional bending moment about the y axis M_y [17]. By using Eqn. (4.21) to

eliminate N from the integrals, we get

$$P = \oint N \mathrm{d}s = \oint [\beta_1 t(\epsilon_0 - yK_x - xK_y) + \beta_2 q]\mathrm{d}s \tag{4.32}$$

$$M_x = -\oint yN\mathrm{d}s = -\oint y[\beta_1 t(\epsilon_0 - yK_x - xK_y) + \beta_2 q]\mathrm{d}s \tag{4.33}$$

$$M_y = -\oint xN\mathrm{d}s = -\oint x[\beta_1 t(\epsilon_0 - yK_x - xK_y) + \beta_2 q]\mathrm{d}s \tag{4.34}$$

In order to express these equations in a matrix form, let's first write out Eqns. (4.32) through (4.34):

$$\begin{aligned}
\epsilon_0 \oint \beta_1 t\mathrm{d}s - K_x \oint y\beta_1 t\mathrm{d}s - K_y \oint x\beta_1 t\mathrm{d}s &= P - \oint \beta_2 q\mathrm{d}s && (4.35)\\
-\epsilon_0 \oint y\beta_1 t\mathrm{d}s + K_x \oint y^2\beta_1 t\mathrm{d}s + K_y \oint xy\beta_1 t\mathrm{d}s &= M_x + \oint y\beta_2 q\mathrm{d}s && (4.36)\\
-\epsilon_0 \oint x\beta_1 t\mathrm{d}s + K_x \oint xy\beta_1 t\mathrm{d}s + K_y \oint x^2\beta_1 t\mathrm{d}s &= M_y + \oint x\beta_2 q\mathrm{d}s && (4.37)
\end{aligned}$$

After multiplying the last two equations by -1, we can write them in a more manageable matrix form

$$\begin{bmatrix} b_{11} & b_{12} & b_{13} \\ b_{21} & b_{22} & b_{23} \\ b_{31} & b_{32} & b_{33} \end{bmatrix} \begin{Bmatrix} \epsilon_0 \\ K_x \\ K_y \end{Bmatrix} = \begin{Bmatrix} P - Q_1 \\ -M_x - Q_2 \\ -M_y - Q_3 \end{Bmatrix} \tag{4.38}$$

where the b matrix is made up of the following elements:

$$\begin{aligned} b_{11} &= \oint \beta_1 t \mathrm{d}s \quad & b_{12} &= -\oint y\beta_1 t \mathrm{d}s \quad & b_{13} &= -\oint x\beta_1 t \mathrm{d}s \\ b_{21} &= \oint y\beta_1 t \mathrm{d}s \quad & b_{22} &= -\oint y^2\beta_1 t \mathrm{d}s \quad & b_{23} &= -\oint xy\beta_1 t \mathrm{d}s \\ b_{31} &= \oint x\beta_1 t \mathrm{d}s \quad & b_{32} &= -\oint xy\beta_1 t \mathrm{d}s \quad & b_{33} &= -\oint x^2\beta_1 t \mathrm{d}s \end{aligned} \tag{4.39}$$

We can certainly solve $[b_{ij}]$ by hand, but they are best left to computer symbolic solvers. It is important that we observe these integrals are full path integrals, and the limits of integrations are as defined in Eqn. (4.3). Due to the asymmetry about the y axis (we defined the cross section of the torque box as a trapezoid), the b matrix is not diagonal. The off-diagonal elements are all zero, except $b_{13} = -b_{31} \neq 0$. Also, to complete the solution of Eqn. (4.38), we have

$$Q_1 = \oint q\beta_2 \mathrm{d}s \quad , \quad Q_2 = \oint y\beta_2 q \mathrm{d}s \quad , \quad Q_3 = \oint x\beta_2 q \mathrm{d}s \tag{4.40}$$

However, for the homogeneous, isotropic case, $Q_i = 0$, because the coupling elastic constant $\alpha_2 = 0$; therefore, $\beta_2 = 0$. In the non-homogeneous, anisotropic case discussed later (see Section 4.2), the S compliance matrix is fully populated, and $\alpha_2 \neq 0$; therefore, $\beta_2 \neq 0$.

In order to solve for the unknown functions ϵ_0 (longitudinal strain in the z direction), K_x (rotation about the x axis) , and K_y (rotation about the y axis) of Eqn. (4.20) we invert

$[b_{ij}]$ to get $[a_{ij}]$. That is

$$\begin{Bmatrix} \epsilon_0 \\ K_x \\ K_y \end{Bmatrix} = \begin{bmatrix} a_{11} & a_{12} & a_{13} \\ a_{21} & a_{22} & a_{23} \\ a_{31} & a_{32} & a_{33} \end{bmatrix} \begin{Bmatrix} P - Q_1 \\ -M_x - Q_2 \\ -M_y - Q_3 \end{Bmatrix} \tag{4.41}$$

Differentiating Eqn. (4.41) with respect to z ($P = const$, $\mathrm{d}M_x/\mathrm{d}z = -V_x = const$, $\mathrm{d}M_y/\mathrm{d}z = -V_y = const$), we get

$$\begin{Bmatrix} \epsilon_0' \\ K_x' \\ K_y' \end{Bmatrix} = \begin{bmatrix} a_{11} & a_{12} & a_{13} \\ a_{21} & a_{22} & a_{23} \\ a_{31} & a_{32} & a_{33} \end{bmatrix} \begin{Bmatrix} 0 \\ V_y \\ V_x \end{Bmatrix} \tag{4.42}$$

The shear flows $q(s)$ must be statically equivalent to the applied moment M [20]. Here we define the quantity $p(s)$ as the perpendicular distance from the origin to the point on the cross section defined by the path coordinate s. In case of the trapezoid cross section, $p(s) = const$ for all sides. For the left and right sides $p(s) = d$. For the top and bottom sides, $p(s)$ can be very closely approximated by $p(s) = \frac{1}{4}(h_1 + h_2)$. Because $p(s)$ is a measure of distance, $p(s) = d$ for the left side as well as for the right side. Using Eqn. (4.24) the expression for the applied moment can is written as

$$M = \oint p(s) \left[q_0 - \epsilon_0' a_1(s) + K_x' a_2(s) + K_y' a_3(s) \right] \mathrm{d}s \tag{4.43}$$

from which we can directly solve for q_0 by

$$\oint p(s)q_0 \mathrm{d}s = M + \epsilon_0' \left(\oint p(s)a_1(s)\mathrm{d}s \right) - K_x' \left(\oint p(s)a_2(s)\mathrm{d}s \right) - K_y' \left(\oint p(s)a_3(s)\mathrm{d}s \right) \tag{4.44}$$

$$q_0 = \frac{1}{\oint p(s)\mathrm{d}s} \left[M + \epsilon_0' a_4 - K_x' a_5 - K_y' a_6 \right] \tag{4.45}$$

where the constants a_4, a_5, and a_6 are given by

$$a_4 = \oint p(s)a_1(s)\mathrm{d}s \tag{4.46}$$

$$a_5 = \oint p(s)a_2(s)\mathrm{d}s \tag{4.47}$$

$$a_6 = \oint p(s)a_3(s)\mathrm{d}s \tag{4.48}$$

The quantity $\frac{1}{\oint p(s)\mathrm{d}s}$ in Eqn. (4.45) is the reciprocal of twice the torque box area, that is

$$\frac{1}{\oint p(s)\mathrm{d}s} = \frac{1}{2A} \tag{4.49}$$

4.1.4 Rate of Twist. The classical theory of thin-walled beams relate the rate of twist of a cell to the shear strains in the wall of the cell [26]. Because we are determining the static deformation of the section, the rate refers to the change of the angle

along the longitudinal coordinate z, as opposed to the change of angle in time. We write the relation as

$$\frac{\mathrm{d}\phi}{\mathrm{d}z} = \frac{1}{2A}\oint \gamma(s)\mathrm{d}s \tag{4.50}$$

where $\phi(s)$ is the angle of twist. In order to define the shear strain $\gamma(s)$, we need to revisit Eqn. (4.7), reproduced here for convenience:

$$\gamma = -\beta_2\epsilon + \beta_4 q\frac{1}{t} \tag{4.51}$$

The longitudinal strain ϵ was defined by Eqn. (4.20), and the shear flow $q(s)$ was given in Eqn. (4.24). Using these two equations in Eqn. (4.7), we have

$$\gamma(s) = -\beta_2(\epsilon_0 - yK_x - xK_y) + \beta_4\left[q_0 - \epsilon_0' a_1(s) + K_x' a_2(s) + K_y' a_3(s)\right]\frac{1}{t} \tag{4.52}$$

Substituting Eqn. (4.52) into Eqn. (4.50), we get

$$\frac{\mathrm{d}\phi}{\mathrm{d}z} = \frac{1}{2A}\left[-\epsilon_0 c_{11} + K_x c_{21} + K_y c_{31} + q_0 d_1 + \epsilon_0' d_2 + K_x' d_3 + K_y' d_4\right] \tag{4.53}$$

where the constants d_i are given by

$$d_1 = \oint \beta_4\frac{1}{t}\mathrm{d}s \tag{4.54}$$

$$d_2 = -\oint a_1(s)\beta_4\frac{1}{t}\mathrm{d}s \tag{4.55}$$

$$d_3 = \oint a_2(s)\beta_4 \frac{1}{t} \mathrm{d}s \tag{4.56}$$

$$d_4 = \oint a_3(s)\beta_4 \frac{1}{t} \mathrm{d}s \tag{4.57}$$

The methodology solving Eqns. (4.54) through (4.57) follows the technique outlined in Eqns. (4.28) through (4.31). For example, solving for d_2 for each side of the trapezoid, we must use the corresponding expression for $a_1(s)$ from Eqns. (4.28) through (4.31), and the corresponding value for the wall thickness $t(s)$. That is

$$\begin{aligned} d_2 = \; & - \int_0^{2dT} a_1^t(s)\beta_4 \frac{1}{t_s} \mathrm{d}s \\ & - \int_{2dT}^{2dT+h_2} a_1^r(s)\beta_4 \frac{1}{t_2} \mathrm{d}s \\ & - \int_{2dT+h_2}^{4dT+h_2} a_1^b(s)\beta_4 \frac{1}{t_s} \mathrm{d}s \\ & - \int_{4dT+h_2}^{4dT+h_2+h_1} a_1^l(s)\beta_4 \frac{1}{t_1} \mathrm{d}s \end{aligned} \tag{4.58}$$

The constants c_{ij} in Eqn. (4.53) are all identically zero for the isotropic case, because the coupling elastic constant β_2 is zero. Therefore, the equation for the rate of twist for the single-cell isotropic thin-walled beam can be simplified from Eqn. (4.53) as

$$\boxed{\frac{\mathrm{d}\phi}{\mathrm{d}z} = \frac{1}{2A}\left(q_0 d_1 + \epsilon_0' d_2 + K_x' d_3 + K_y' d_4\right)} \tag{4.59}$$

where the constants d_i are known through Eqns. (4.54) through (4.57), the constant shear flow q_0 is given by Eqn. (4.45), and the constants ϵ_0', K_x', and K_y' are found from Eqn. (4.42).

4.1.5 Isotropic Case Identified.

The motivation behind developing the homogeneous, isotropic solution using the full anisotropic methodology was to be able to check the result and accuracy of the solution. The answer from the single-cell torsion solution (see Chapter III) will serve as a 'yardstick' for the result obtained from the homogeneous, single-cell torsion solution.

4.2 Non-homogeneous Anisotropic Single Cell Beam

4.2.1 Considerations.

The definition of non-homogeneous cross-section in this context means that the coupling elastic constant β_2, and therefore α_2 are functions of the path length coordinate s. Due to the non-zero (and also not 90 degrees) composite fiber orientation angle θ, the elastic coupling constant β_2 will change sign as the fiber angle changes sign with respect to the z structural axis. That is, the angle θ between the structural axis z and the principal fiber direction is greater than zero if the fiber is rotated with respect to the z axis in a positive sense in the right-handed coordinate system. The positive rotation is defined as the direction of the vector cross product of these two axes that define the plane of the rotation angle θ. If the fiber is wound continuously around the box beam we have:

$$\beta_2 \begin{cases} > 0 \quad : \quad s_0 \leq s \leq s_1 \\ > 0 \quad : \quad s_1 \leq s \leq s_2 \\ < 0 \quad : \quad s_2 \leq s \leq s_3 \\ < 0 \quad : \quad s_3 \leq s \leq s_4 \end{cases} \tag{4.60}$$

where the limits s_i are identified by Eqn. (4.3).

4.2.2 Analysis. Because the method of analysis outlined in Section 4.1 is derived for a fully anisotropic case, then applied to an isotropic example, all the steps outlined in that section apply to the current, non-homogeneous, anisotropic solution. In Eqn. (4.40) we found the integrals that define Q_1, Q_2, and Q_3. In this case, these constants are not zero, because the elastic coupling constant β_2 is not equal to zero. This comes from the fact that the compliance matrix S is fully populated; therefore, $\alpha_2 = S_{14} \neq 0$. Because α_1 is always non-zero, using Eqn. (4.9), the constant β_2 is defined and non-zero.

Recall that up until Eqn. (4.52), none of the formulas involve β_2; therefore, the results obtained in Section 4.1 remain valid. From Eqn. (4.40) we have

$$\begin{aligned} q_0 \oint \beta_2 \mathrm{d}s - \epsilon_0' \oint a_1(s)\beta_2 \mathrm{d}s + K_x' \oint a_2(s)\beta_2 \mathrm{d}s + K_y' \oint a_3(s)\beta_2 \mathrm{d}s &= Q_1 \\ q_0 \oint y\beta_2 \mathrm{d}s - \epsilon_0' \oint y a_1(s)\beta_2 \mathrm{d}s + K_x' \oint y a_2(s)\beta_2 \mathrm{d}s + K_y' \oint y a_3(s)\beta_2 \mathrm{d}s &= Q_2 \\ q_0 \oint x\beta_2 \mathrm{d}s - \epsilon_0' \oint x a_1(s)\beta_2 \mathrm{d}s + K_x' \oint x a_2(s)\beta_2 \mathrm{d}s + K_y' \oint x a_3(s)\beta_2 \mathrm{d}s &= Q_3 \end{aligned} \tag{4.61}$$

which we can write in matrix notation as

$$\begin{bmatrix} c_{11} & c_{12} & c_{13} & c_{14} \\ c_{21} & c_{22} & c_{23} & c_{24} \\ c_{31} & c_{32} & c_{33} & c_{34} \end{bmatrix} \begin{Bmatrix} q_0 \\ \epsilon_0' \\ K_x' \\ K_y' \end{Bmatrix} = \begin{Bmatrix} Q_1 \\ Q_2 \\ Q_3 \end{Bmatrix} \tag{4.62}$$

where the elements of the c matrix are now defined as

$$\begin{array}{llll} c_{11} = \oint \beta_2 \mathrm{d}s & c_{12} = -\oint a_1(s)\beta_2 \mathrm{d}s & c_{13} = \oint a_2(s)\beta_2 \mathrm{d}s & c_{14} = \oint a_3(s)\beta_2 \mathrm{d}s \\ c_{21} = \oint y\beta_2 \mathrm{d}s & c_{22} = -\oint y a_1(s)\beta_2 \mathrm{d}s & c_{23} = \oint y a_2(s)\beta_2 \mathrm{d}s & c_{24} = \oint y a_3(s)\beta_2 \mathrm{d}s \\ c_{31} = \oint x\beta_2 \mathrm{d}s & c_{32} = -\oint x a_1(s)\beta_2 \mathrm{d}s & c_{33} = \oint x a_2(s)\beta_2 \mathrm{d}s & c_{34} = \oint x a_3(s)\beta_2 \mathrm{d}s \end{array} \tag{4.63}$$

Finding c_{ij} by the path integrals requires some clarification. For example, c_{23} is summed clockwise around the perimeter, starting from $s = 0$. For each consecutive side of the trapezoid, we must use the corresponding expression for $a_2(s)$. Therefore, the constant c_{23} is given by

$$\begin{aligned} c_{23} = & \int_0^{s_1} \left[\frac{h_2 - h_1}{4dT}(s - Td) + \frac{1}{4}(h_2 + h_1) \right] \beta_2 a_2^t(s) \mathrm{d}s + \\ & + \int_{s_1}^{s_2} (2Td - s + \frac{1}{2}h_2)\beta_2 a_2^r(s) \mathrm{d}s + \\ & + \int_{s_2}^{s_3} - \left[\frac{h_2 - h_1}{4dT}(3Td - s + h_2) + \frac{1}{4}(h_2 + h_1) \right] (-\beta_2) a_2^b(s) \mathrm{d}s + \\ & + \int_{s_3}^{s_4} (s - 4Td - h_2 - \frac{1}{2}h_1)(-\beta_2) a_2^l(s) \mathrm{d}s \end{aligned} \tag{4.64}$$

where the limits of integrations s_i are given by Eqn. (4.3), and the superscripts on $a_2(s)$ refer to the top, right, bottom, and left sides of the trapezoid, respectively. Observe that the sign of β_2 changes on the bottom and the left sides of the trapezoid. This is the effect of the non-homogeneous construction, when the bottom side is the mirror image of the top side, that is, the fiber orientation angle on the bottom surface (with respect to the right-handed structural coordinate system) is equal and opposite to that of the top surface [17]. For the same reason, the sign of β_2 changes from the right side to the left side. The solution for the rest of the c matrix follows the same procedure, without exceptions.

4.2.3 Rate of Twist.

The rate of twist of the homogeneous single-cell section was developed in Section 4.1.4. Equations (4.50) and (4.53) remain valid in this case, except now we must account for the constants c_{ij} as well. Because the functions Q_i are not zero, we first need to solve for ϵ_0, K_x, and K_y. From Eqn. (4.41) we have

$$\begin{Bmatrix} \epsilon_0 \\ K_x \\ K_y \end{Bmatrix} = \begin{bmatrix} a_{11} & a_{12} & a_{13} \\ a_{21} & a_{22} & a_{23} \\ a_{31} & a_{32} & a_{33} \end{bmatrix} \begin{Bmatrix} P - Q_1 \\ -M_x - Q_2 \\ -M_y - Q_3 \end{Bmatrix} \tag{4.65}$$

where Q_i are given by Eqn. (4.62). Once we perform the matrix multiplications, we can substitute Q_i into Eqn. (4.41) and obtain the expressions for ϵ_0, K_x, and K_y. The final format of Eqn. (4.65) will be

$$\epsilon_0 = a_{11}(P - Q_1) - a_{12}(M_x + Q_2) - a_{13}(M_y + Q_3) \tag{4.66}$$

$$K_x = a_{21}(P - Q_1) - a_{22}(M_x + Q_2) - a_{23}(M_y + Q_3) \tag{4.67}$$

$$K_x = a_{31}(P - Q_1) - a_{32}(M_x + Q_2) - a_{33}(M_y + Q_3) \tag{4.68}$$

Now that ϵ_0, K_x, and K_y are given by Eqns. (4.66) through (4.68), ϵ_0', K_x', and K_y' are determined by Eqn. (4.42), the constants c_{ij} are given by Eqn. (4.63), the constants d_i are known by Eqns. (4.54) through (4.57), we can write the rate of twist for the non-

homogeneous, anisotropic, single-cell section as

$$\boxed{\frac{\mathrm{d}\phi}{\mathrm{d}z} = \frac{1}{2A}\left(-\epsilon_0 c_{11} + K_x c_{21} + K_y c_{31} + q_0 d_1 + \epsilon_0' d_2 + K_x' d_3 + K_y' d_4\right)} \tag{4.69}$$

4.3 Discussion

To evaluate Eqns. (4.8) through (4.69) simultaneously for the given geometry is a formidable as well as lengthy task. The evaluation of the full and the partial path integrals could easier be done by using symbolic solvers. The symbolic results of Eqns. (4.8) through (4.69) were entered into a Matlab subroutine called ANISOTORSION_COMPZ that calculates the tip twist angle of the non-homogeneous (see Section 4.2) anisotropic, single-cell, closed-section box beam. This code can also be used to calculate the tip twist of a homogeneous anisotropic beam, since in this case the coupling constant β_2 is zero (see Section 4.1.3.2).

Another Matlab subroutine called LAYUP [23] was applied in order to calculate the engineering properties of the fully anisotropic composite-laminate, single-cell, closed section box beam, so that the stiffness and compliance matrices of the laminae in the 1-2 principal axes can be transformed into the x-y-z structural axes of the laminate, and sent to the subroutine ANISOTORSION_COMPZ.

A driver program called COMPL_ANISO_COPMZ was written in order to define the material properties in the 1-2 principal axes of the anisotropic composite lamina materials of choice. All three subroutines and programs are listed in Appendix C.

V. Induced Strain Actuation

5.1 Single-Cell Beam with PZT Lamina

5.1.1 PZT-Composite Layup. In order to produce induced strain in the top and the bottom surfaces of the single-cell box beam, a single layer of continuous-sheet PZT lamina is incorporated in the composite laminate of the top and the bottom surfaces of the beam as shown in Figure (5.1). In addition to the assumptions made in Section 4.1.1, it is assumed that the PZT layer is perfectly bonded within the host structure, that is no slip, disbond, or shear-lag is accounted for. The PZT lamina, when used as an actuator

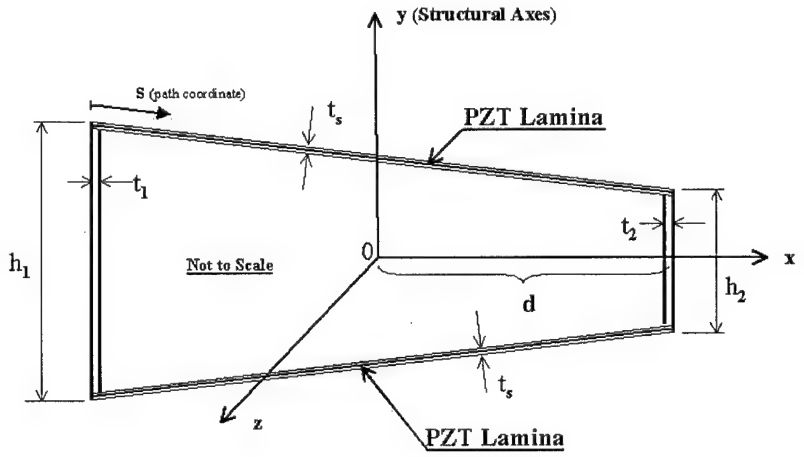

Figure 5.1 Torque Box with Embedded Piezoelectric Lamina

under tension, pulls the host structure inward; when under compression, it pushes the host structure outward. If the top PZT lamina is subjected to an electric field that creates compression, while the bottom PZT lamina experiences tension, the entire single-cell beam will be subjected to a pitching moment about the negative z structural axis. This way the beam is torqued nose up, and the angle-of-attack increases. If the electric fields are

switched on the PZT laminae, the moment changes direction, and the beam is subjected to a positive torque that pitches the beam nose down. See Figure (5.2) for a simplified representation of the PZT actuation of a generic (geometry is not related to the simplified trapezoid section) host structure.

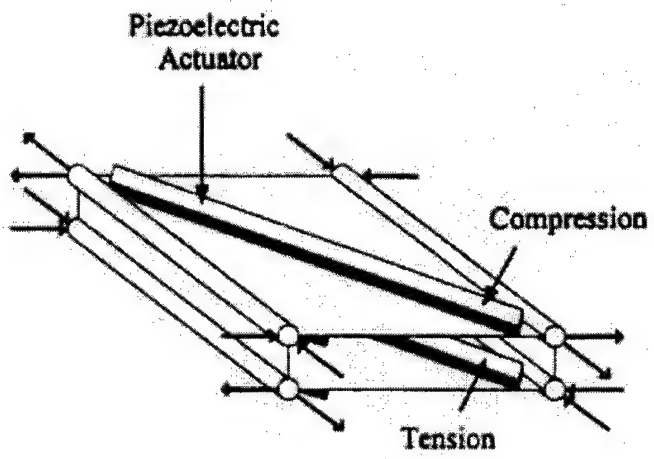

Figure 5.2 Piezoelectric Lamina Configuration [12]

To achieve high PZT actuator effectiveness, a PZT lamina with high piezoelectric constant (strain coefficient) d_{33} must be selected. If d_{33} of the PZT is small, a large voltage is required to produce strain in the PZT. If d_{33} is large, a small amount of voltage is sufficient to produce the necessary strain [9]. The PZT must also have high Young's modulus of elasticity E compared to the host structure, so that a large fraction of the strain produced by the electric field can be transferred to the host structure [9].

Piezo-fiber composites are becoming more readily available, as well as less expensive. For this study, two PZT fibers were considered, with almost identical material properties. The first PZT lamina selected is an Active Fiber Composite (AFC) PZT 5H fibers with thermosetting epoxy resin matrix and etched copper/Kapton interdigitated electrodes. A

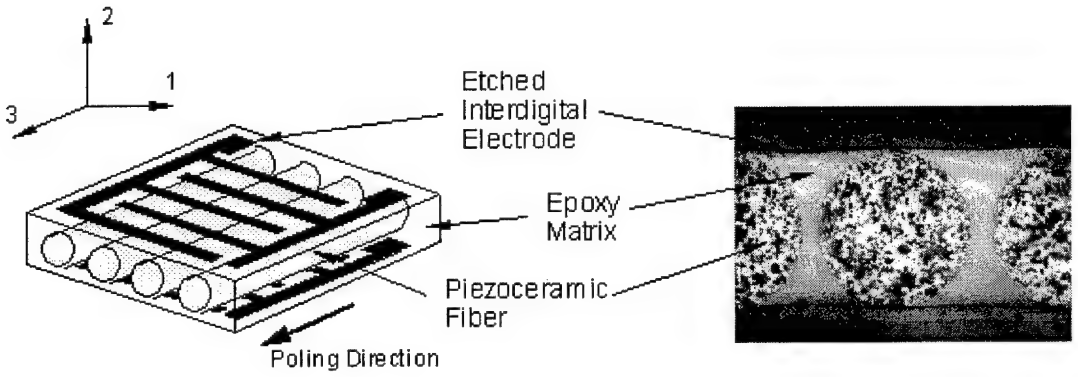

Figure 5.3 Diagram and Cross-section of the AFC Lamina [5]

Table 5.1 **PZT-Fiber Composites**

Fiber Type	E_1 (Msi)	E_2 (Msi)	G_{12} (Msi)	ν_{12}	t (in)	d_{33} (pm/V)	d_{31} (pm/V)
AFC Lamina	4.6786	2.4173	0.5802	0.30	0.0065	180	-50
G-1195 PZT	5.4389	2.0305	0.5511	0.30	0.0080	$200-400$	$0.1d_{33}$

representative example of the AFC PZT is illustrated in Figure (5.3). The other is a generic piezo-fiber composite from reference [3]. The material properties of the two PZT composites are summarized in Table (5.1).

Before attempting to derive the torsional formula for this PZT-composite beam, we have to incorporate the PZT engineering properties into the those of the composite laminate alone. We achieve this by modifying the Matlab routine used for calculating the engineering properties of the laminate alone so that it accounts for the single ply of PZT. For sake of simplicity, but without any loss of generality, the PZT lamina was applied to the center of the laminate by replacing the middle composite layer.

5.1.2 Constitutive Relations. The plane stress constitutive relations (strain-stress) of Section 4.1.2 have to be modified to account for the PZT layer, that may not have the same material properties as the composite lamina. Therefore, we write

Eqns. (4.4) through (4.5) with the PZT strain (ϵ_p), and the PZT shear (γ_p) in the material principle directions

$$\epsilon = \alpha_1 N \frac{1}{t} + \alpha_2 q \frac{1}{t} + \epsilon_p \tag{5.1}$$

$$\gamma = \alpha_2 N \frac{1}{t} + \alpha_4 q \frac{1}{t} + \gamma_p \tag{5.2}$$

Using the same argument preceeding Eqns. (4.6) and (4.7) we have

$$N = \beta_1 \epsilon \; t + \beta_2 q - \beta_1 \epsilon_p \; t \tag{5.3}$$

$$\gamma = -\beta_2 \epsilon + \beta_4 q \frac{1}{t} + \beta_2 \epsilon_p + \gamma_p \tag{5.4}$$

where all the constants evaluated to be the same as defined in Eqns. (4.8) through (4.10). Writing the full anisotropic strain-stress (constitutive) equations for plane stress and comparing them to Eqn. (5.1), we obtain the same results as in Eqns. (4.14) and (4.16). Therefore, the addition of the PZT term in the Eqns. (5.1) and (5.2) did not change our coupling coefficients defined previously in Eqns. (4.8) and (4.10).

5.1.3 Analysis.

5.1.3.1 Preliminary Considerations.

By establishing the same differential equations of equilibrium considered in Section 4.1.3.1, and using Eqns. (4.17) and

(4.20), we obtain the expression for the force per unit length N, namely

$$N = \beta_1 t(\epsilon_0 - yK_x - xK_y) + \beta_2 q - \beta_1 \epsilon_p \, t \tag{5.5}$$

Differentiating with respect to z, we get

$$\frac{\partial N}{\partial z} = \beta_1 t(\epsilon_0' - yK_x' - xK_y') - \beta_1 \epsilon_p' t \tag{5.6}$$

where the derivative of the piezoelectric strain with respect to the spanwise coordinate z is zero as long as uniform voltage is applied to the PZT lamina. That is

$$\epsilon_p' = \frac{\partial \epsilon_p}{\partial z} = 0 \tag{5.7}$$

With this assumption, we obtain the expression for $\partial N/\partial z$

$$\frac{\partial N}{\partial z} = \beta_1 t(\epsilon_0' - yK_x' - xK_y') \tag{5.8}$$

that is identical to the result derived in Section 4.1.3.1, Eqn. (4.22). Therefore, the rest of the derivation for Eqns. (4.24) through (4.31) is as outlined before.

5.1.3.2 Equations of Static Equivalence. The cross sectional loadings will now have to be modified to account for strain actuation as well. Equations (4.32) through (4.34) are written in a form

$$P = \oint N \mathrm{d}s = \oint [\beta_1 t(\epsilon_0 - yK_x - xK_y) + \beta_2 q - \beta_1 \epsilon_p t] \mathrm{d}s \tag{5.9}$$

$$M_x = -\oint yN\mathrm{d}s = -\oint y[\beta_1 t(\epsilon_0 - yK_x - xK_y) + \beta_2 q - \beta_1 \epsilon_p t]\mathrm{d}s \tag{5.10}$$

$$M_y = -\oint xN\mathrm{d}s = -\oint x[\beta_1 t(\epsilon_0 - yK_x - xK_y) + \beta_2 q - \beta_1 \epsilon_p t]\mathrm{d}s \tag{5.11}$$

that can be written as (see also Eqn. (4.38))

$$\begin{bmatrix} b_{11} & b_{12} & b_{13} \\ b_{21} & b_{22} & b_{23} \\ b_{31} & b_{32} & b_{33} \end{bmatrix} \begin{Bmatrix} \epsilon_0 \\ K_x \\ K_y \end{Bmatrix} = \begin{Bmatrix} P - Q_1 + Z_1 \\ -M_x - Q_2 + Z_2 \\ -M_y - Q_3 + Z_3 \end{Bmatrix} \tag{5.12}$$

where the $[b]$ matrix is given by Eqn. (4.39), and the quantities Z_i are given by

$$Z_1 = \oint \beta_1 \epsilon_p t\mathrm{d}s \qquad Z_2 = \oint y\beta_1 \epsilon_p t\mathrm{d}s \qquad Z_3 = \oint x\beta_1 \epsilon_p t\mathrm{d}s \tag{5.13}$$

The full path integrals of Eqn. (5.13) must be evaluated the same way we treated the path integral in Eqn. (4.58). In doing so we find

$$Z_1 = 4\beta_1 t_s \epsilon_p T d \qquad Z_2 = 0 \qquad Z_3 = 0 \tag{5.14}$$

Evaluating the derivatives of Eqn. (5.14) with respect to z we arrive to

$$Z_1' = 0 \qquad Z_2' = 0 \qquad Z_3' = 0 \tag{5.15}$$

After rearranging Eqn. (5.12), and differentiating, we get

$$\begin{Bmatrix} \epsilon_0' \\ K_x' \\ K_y' \end{Bmatrix} = \begin{bmatrix} a_{11} & a_{12} & a_{13} \\ a_{21} & a_{22} & a_{23} \\ a_{31} & a_{32} & a_{33} \end{bmatrix} \begin{Bmatrix} 0 \\ V_y \\ V_x \end{Bmatrix} \tag{5.16}$$

which is identical to Eqn. (4.42).

5.1.4 Rate of Twist. In light of the results of Section 5.1.3, all equations apply until Eqn. (4.50), which is reproduced here as

$$\frac{\mathrm{d}\phi}{\mathrm{d}z} = \frac{1}{2A} \oint \gamma(s) \mathrm{d}s \tag{5.17}$$

where the shear strain is given by

$$\gamma = \alpha_2 N \frac{1}{t} + \alpha_4 q \frac{1}{t} + \gamma_p \tag{5.18}$$

This can also be written as

$$\gamma = -\beta_2 \epsilon + \beta_4 q \frac{1}{t} + \beta_2 \epsilon_p + \gamma_p \tag{5.19}$$

which is Eqn. (5.4) from Section 5.1.2. Substituting from Eqns. (4.20) and (4.24), we get

$$\gamma(s) = -\beta_2(\epsilon_0 - yK_x - xK_y) + \beta_4 \left[q_0 - \epsilon_0' a_1(s) + K_x' a_2(s) + K_y' a_3(s)\right] \frac{1}{t} + \beta_2 \epsilon_p + \gamma_p \tag{5.20}$$

which modifies Eqn. (4.53) to

$$\frac{\mathrm{d}\phi}{\mathrm{d}z} = \frac{1}{2A}\left[-\epsilon_0 c_{11} + K_x c_{21} + K_y c_{31} + q_0 d_1 + \epsilon_0' d_2 + K_x' d_3 + K_y' d_4 + c_{11}\oint \epsilon_p \mathrm{d}s + \oint \gamma_p \mathrm{d}s\right] \tag{5.21}$$

where the constants d_i are as given by Eqns. (4.54) through (4.57). The full path integral of the piezoelectric strain γ_p is evaluated the way it was demonstrated for c_{23} of Eqn. (4.64). Assuming PZT lamina only in the skins, we obtain

$$\oint \gamma_p(s)\mathrm{d}s = 4\gamma_p T d \tag{5.22}$$

$$\oint \epsilon_p(s)\mathrm{d}s = 4\epsilon_p T d \tag{5.23}$$

where ϵ_p and γ_p is the PZT strain and shear in the structural axes, respectively. For a homogeneous cross section, all c_{ij} are zero, therefore

$$\boxed{\frac{\mathrm{d}\phi}{\mathrm{d}z} = \frac{1}{2A}\left(q_0 d_1 + \epsilon_0' d_2 + K_x' d_3 + K_y' d_4 + 4\gamma_p T d\right)} \tag{5.24}$$

5.2 Non-homogeneous PZT-Composite Beam

5.2.1 Analysis. For a non-homogeneous cross section, we follow Section 4.2. Because all Q_i's are still defined in the PZT composite case the same way they were in the composite-only case, Eqns. (4.60) through (4.63) still hold.

5.2.2 Rate of Twist. Recall that for the non-homogeneous cross section, $c_{ij} \neq 0$. However, Eqn. (4.65) is now extended with the summation of the longitudinal

strain terms, Z_i. That is,

$$\begin{Bmatrix} \epsilon_0 \\ K_x \\ K_y \end{Bmatrix} = \begin{bmatrix} a_{11} & a_{12} & a_{13} \\ a_{21} & a_{22} & a_{23} \\ a_{31} & a_{32} & a_{33} \end{bmatrix} \begin{Bmatrix} P - Q_1 + Z_1 \\ -M_x - Q_2 + Z_2 \\ -M_y - Q_3 + Z_3 \end{Bmatrix} \tag{5.25}$$

where Z_i are given by Eqn. (5.13). Using the results of Eqn. (5.14) we can evaluate Eqn. (5.25) and get

$$\epsilon_0 = a_{11}(P - Q_1 + Z_1) - a_{12}(M_x + Q_2) - a_{13}(M_y + Q_3) \tag{5.26}$$

$$K_x = a_{21}(P - Q_1 + Z_1) - a_{22}(M_x + Q_2) - a_{23}(M_y + Q_3) \tag{5.27}$$

$$K_y = a_{31}(P - Q_1 + Z_1) - a_{32}(M_x + Q_2) - a_{33}(M_y + Q_3) \tag{5.28}$$

where $Z_2 = Z_3 = 0$ as per Eqn. (5.14). Now that ϵ_0, K_x, and K_y are given by Eqns. (5.26) through (5.28), ϵ_0', K_x', and K_y' are determined by Eqn. (5.16), the constants c_{ij} are given by Eqn. (4.63), the constants d_i are known by Eqns. (4.54) through (4.57), we can write the rate of twist for the non-homogeneous, anisotropic, single-cell section as

$$\boxed{\frac{\mathrm{d}\phi}{\mathrm{d}z} = \frac{1}{2A}\left(-\epsilon_0 c_{11} + K_x c_{21} + K_y c_{31} + q_0 d_1 + \epsilon_0' d_2 + K_x' d_3 + K_y' d_4 + 4\epsilon_p T d c_{11} + 4\gamma_p T d\right)} \tag{5.29}$$

5.3 *Determining the PZT Strain Tensor*

Using Eqn. (5.29) we can determine the angle of twist due to PZT actuation of the non-homogeneous, anisotropic, single-cell beam with PZT actuator lamina embedded in the laminate center of the top and bottom skins. All variables and coefficients of Eqn. (5.29) are known through the derivation presented in Chapters IV and V, except the PZT strain ϵ_p, and the PZT shear γ_p. Before calculating the twist angle due to an applied electric field (Voltage), we need to find ϵ_p and γ_p of the PZT. Because the PZT actuator lamina is at an angle with respect to the material axes of the torquebox, we first need to determine ϵ_p and γ_p in the PZT lamina principal axes, then transform these strain and shear to the structural axes.

For the sake of preserving the conventions for the directions of piezoelectric actuation, let's rename our principal 1-2-3 (fiber-transverse-out of plane) composite-fiber material directions to 3-1-2 (fiber-transverse-out of plane) composite-PZT material directions, as demonstrated in Figure (5.4). This way we can retain the subscripts on all the piezoelectric, and electric field coefficients to be introduced in the following section.

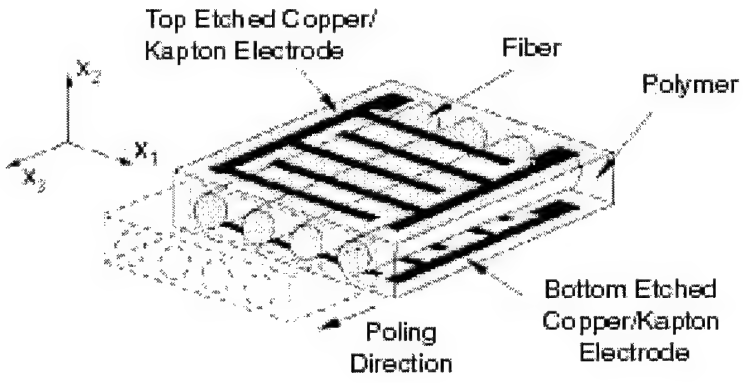

Figure 5.4 Diagram, and Principal Axes of the AFC lamina [5]

5.3.1 *Piezoelectric Strain Coefficients.*

According to the notation of IEEE Standard 176-1978, the linear, coupled electro-mechanical constitutive relations are

$$\begin{aligned} D &= \epsilon^T E + dT \\ S &= d_t E + s^E T \end{aligned} \tag{5.30}$$

where the independent variable stress (T) and electric field (E) and the dependent variables strain (S) and electric displacement (D) are related by the dielectric coefficient (ϵ^T), piezoelectric coefficient (d), and the compliance matrix (S^E) [8]. For piezoelectric materials of unit thickness the relation between actuation strain and the applied electric field (E_1, E_2, E_3 in the principal 1-2-3 directions respectively) is given by

$$\Lambda = \begin{bmatrix} 0 & 0 & d_{31} \\ 0 & 0 & d_{31} \\ 0 & 0 & d_{33} \\ 0 & d_{15} & 0 \\ d_{15} & 0 & 0 \\ 0 & 0 & 0 \end{bmatrix} \begin{Bmatrix} E_1 \\ E_2 \\ E_3 \end{Bmatrix} \tag{5.31}$$

The coefficients d_{31}, d_{33}, and d_{15} are the piezoelectric strain coefficients (or constants). The constant d_{33} characterizes the strain in the material principal fiber direction, and the constant d_{31} characterizes the strain in the material transverse direction. In accordance with the assumptions and restrictions made on the analysis in Section 4.1.2, and to simplify

the relations of Eqn. (5.31) we set

$$E_1 = E_2 = 0 \tag{5.32}$$

Therefore, the PZT strain tensor $\epsilon_{1,2,3}$ in the principal directions is expressed by

$$\left[\epsilon_{1,2,3}\right] = \begin{bmatrix} d_{31} & 0 & 0 \\ 0 & d_{31} & 0 \\ 0 & 0 & d_{33} \end{bmatrix} \left\{E_3\right\} \tag{5.33}$$

where E_3 is given by the applied voltage divided by the PZT lamina characteristic distance.

If the piezoelectric constants are of opposite signs, the applied electric field creates extension in one direction (positive constant), and contraction (negative constant) in the other. If the constants are of the same sign, the electric field will induce extension or contraction simultaneously in both principal directions. For the 45-degree PZT layup used in the study (see Figure (5.2)), a PZT lamina with positive d_{33}, and negative d_{31} could generate torsion of the beam more effectively, since the mechanical strains on the top and bottom surfaces are of the opposite signs. Which beam is going to produce more angular twist; however, is also going to depend on the numerical values of the piezoelectric coefficients. The higher the coefficient, the greater the induced strain.

For the AFC lamina, the piezoelectric coefficients d_{33} and d_{31} are given as material parameters. For the G-1195 PZT lamina, a single constant is inadequate to relate strain to the electric field. From a series of elastically-constrained piezoceramics tests, it was determined that the value of d_{33} depends on the level of induced strain [8]. This is the

strain that appears in the PZT lamina when it is embedded in a structure, and it is due to the piezoelectric actuation. Therefore, a secant piezoelectric coefficient will be defined as

$$d_{33}^{*} \equiv \frac{\Lambda_1}{E_3} \tag{5.34}$$

where Λ_1 is the actuation strain (that physically causes induced strains, and can be due to piezoelectricity, electrostriction, or even thermal expansion) in the transverse direction. An approximate linear relation can be set up between the induced strain and the applied electric field, using Fig A.1 from reference [10]. Another linear approximation for the appropriate value of the piezoelectric constant can be found from Figure 7, of reference [8]. The value of the transverse piezoelectric constant d_{31} can be approximated as 10% of d_{33}. The maximum value for Λ_1 is selected as the maximum strain so that depoling of the PZT fibers is avoided [3].

Depoling of the fibers can occur if the applied voltage V becomes greater than the coercive field E_c. During the manufacture of piezoceramics, a coercive electric field is applied across the fibers to align the PZT crystals into an initial polarization. If the applied voltage during operations is greater than this electric field in the opposite direction, depoling of the fibers can take place, and repoling in the opposite direction will occur. If the applied field is aligned with the initial poling direction, depoling will not take place even if the applied electric field exceeds the coercive field. Therefore, the maximum voltage applicable to the AFC lamina will be $\pm$1000 V [5]. For the G-1195 PZT lamina, the applicable voltage per thickness is $\pm$750-1000 Vmm [8],[15]. Considering the thickness of

the G-1195 PZT lamina listed in Table (5.1), the maximum voltage that can be applied is ±200V.

Now that all the pieces of information about the piezoelectric coefficients in the material principal axes are given for both PZT laminae through Table (5.1) and Eqn. (5.34), using the appropriate coordinate transformations we find the PZT strain tensor ϵ_{st} in the structural directions.

5.3.2 PZT Strain Tensor Transformation. Figure (5.5) illustrates the coordinate rotation from the material principal directions into the structural directions. The principal fiber direction of the PZT-composite is represented by the principle direction 3, and the structural spanwise direction is given by z. The principal axes 3-1-2 are rotated

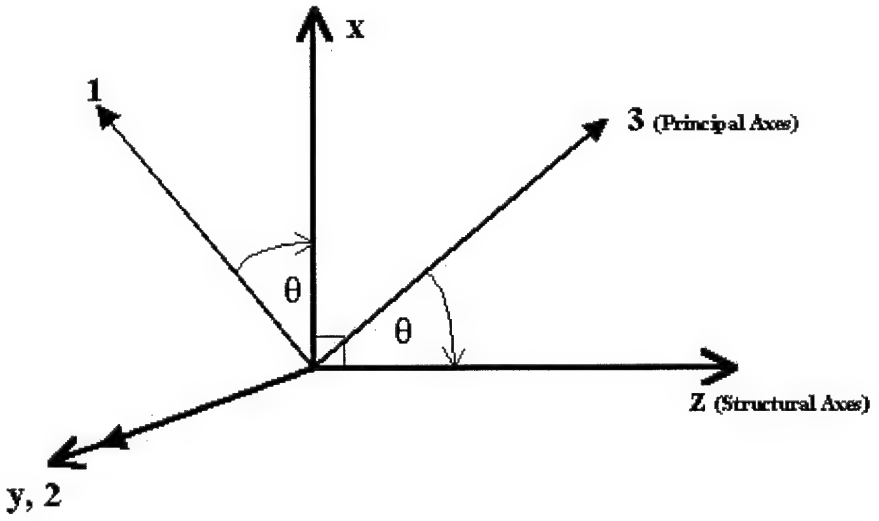

Figure 5.5 PZT Strain Tensor Coordinate Transformation

by angle $-\theta$ about the 2 axis into the structural axes. Then, the principle-to-structural

transformation (a '–2' rotation) matrix C is given by

$$\left[C\right] = \begin{bmatrix} cos(\theta) & 0 & sin(\theta) \\ 0 & 1 & 0 \\ -sin(\theta) & 0 & cos(\theta) \end{bmatrix} \tag{5.35}$$

The principle-to-structural strain tensor transformation, using Eqns. (5.33) and (5.35) is given by

$$\left[\epsilon_{st}\right] = \left[C\right]^{-1} \begin{bmatrix} d_{31} & 0 & 0 \\ 0 & d_{31} & 0 \\ 0 & 0 & d_{33} \end{bmatrix} \left[C\right] E_3 \tag{5.36}$$

After the transformation, we obtain the PZT strain tensor, as well as the PZT strain and shear ϵ_p and γ_p in the structural axes

$$\left[\epsilon_{st}\right] = \begin{bmatrix} \epsilon_x & 0 & \epsilon_{xz} \\ 0 & \epsilon_y & 0 \\ \epsilon_{zx} & 0 & \epsilon_z \end{bmatrix} \tag{5.37}$$

where

$$\begin{aligned} \epsilon_z = \epsilon_p &= \left[d_{31}sin^2(\theta) + d_{33}cos^2(\theta)\right] E_3 \\ \epsilon_{xz} = \epsilon_{zx} = \gamma_p &= \left[d_{31}cos(\theta)sin(\theta) - d_{33}sin(\theta)cos(\theta)\right] E_3 \end{aligned} \tag{5.38}$$

are to be used in Eqn. (5.29).

5.4 Discussion

5.4.1 Composite-PZT Beam Torsion. Evaluating Eqns. (5.9) through (5.38) — simultaneously for the given geometry and composite-PZT construction — is a formidable as well as lengthy task. The evaluation of the full-, and the partial-path integrals could easier be done by using symbolic solvers. The symbolic solutions of Eqns. (5.9) through (5.29) were found using MathCad, and were entered into a Matlab subroutine called ANISOTORSION_PZT that calculates the tip twist angle of the non-homogeneous (see Section 4.2) anisotropic, single-cell, closed-section box beam with a single layer of PZT lamina in the geometric center of the composite laminate, subjected to a uniform cross sectional-moment about the structural z axis. This code can also be used to calculate the tip twist of a homogeneous anisotropic beam subjected to the same conditions, since in this case the coupling constant β_2 is zero (Section 4.1.3.2).

The Matlab subroutine called LAYUP of Section 4.3 is used by the program ANISOTORSION_PZT without modifications.

A driver program called COMPL_ANISO_PZT was written in order to define the material properties in the 1-2 principal axes of the composite and PZT lamina materials of choice. It also defines the single-cell torquebox geometry obtained from the program AREA of Chapter II, and establishes the desired loading conditions. Both codes are listed in Appendix D.

5.4.2 PZT Strain Actuation. The Matlab subroutine called ANISOTORSION_PZT_E calculates the tip twist angle of the non-homogeneous (see Section 4.2), anisotropic, single-cell, closed-section box beam with a single layer of PZT lamina in the

geometric center of the composite laminate, subjected to a uniform electric field E_3 applied in the principal PZT fiber direction due to an applied voltage V. The twist angles are calculated for a range of fiber orientation angles, input by the user. This code can also be used to calculate the tip twist of a homogeneous anisotropic beam subjected to the same conditions, since in this case the elastic coupling constant β_2 is zero (see Section 4.1.3.2).

The program ANISOTORSION_PZT_E uses the LAYUP subroutine of Section 4.3 without modifications.

The transformation of the PZT strains and shears in the principal axes into the strains and shears in the structural axes is accomplished by the subroutine TRANSFORM. Its inputs are the PZT principal strain tensor, and the PZT rotation angle with respect to the structural axes. It outputs the strain tensor in the structural axes.

A driver program called COMPL_ANISO_PZT_E was written in order to define the material properties in the principal axes of the composite and PZT lamina materials of choice. It also defines the piezoelectric properties of the PZT lamina in the 3-1 principal axes and establishes the desired loading conditions. All three programs and subroutines are listed in Appendix E.

VI. Results and Discussion

6.1 Single-, and Three-Cell, Isotropic Beam

As was discussed in Chapter III, the Matlab code SHEARFLOW3CELL was run in order to gather data on the concentrated torsional moment required, and the resulting shear flows in the spars and skins of the single-, and three-cell closed section, isotropic (aluminum) torque box. The material properties of the 2024-T3 aluminum are listed in Table (6.1). The code was run with the original geometric properties of the 2-D profile, obtained from the Matlab code AREA (see Appendix A) for angles 2 to 10 degrees with 2-degree increments. Interested users can of course change the imposed twist angles and investigate the relationship between the angle of twist, moment and shear flows required. For the given angles, Table (6.2) summarizes the results. The tabulated values of the required moments versus twist angles are also shown (and the linear relationship can be better observed) in Figure (6.1). Comparing the moments required to generate the angle of twist for the single-cell beam to that of the three-cell beam it is evident, that in order to generate a given angular twist, a larger moment is required for the three-cell beam than for the single-cell beam. This is due to the increased torsional stiffness (see Eqn. (3.29)) of the multi-cell beam, compared to that of the single-cell beam. This is the reason why multi-cell

Table 6.1 **Isotropic Material Properties**

Aluminum 2024 T3		
Young's Modulus E (Msi)	Shear Modulus G (Msi)	Poisson's Ratio ν
10.4	3.86	0.33

Table 6.2 **Single-, and Three-Cell Torque Box Results**

	Single Cell		Three Cell			
Twist Angle (deg)	Shearflow (lb/in)	Moment (ft-lb)	q1 (lb/in)	q2 (lb/in)	q3 (lb/in)	Moment (ft-lb)
2.0	170.6	6517	129.7	165.9	63.9	8733
4.0	341.2	13033	259.3	331.7	127.7	17467
6.0	511.8	19550	388.9	497.6	191.6	26200
8.0	682.4	26067	518.6	663.5	255.5	34934
10.0	853.0	32583	648.3	829.4	319.3	43667

sections are more resistive to torsion. Another important observation from Table (6.2) is

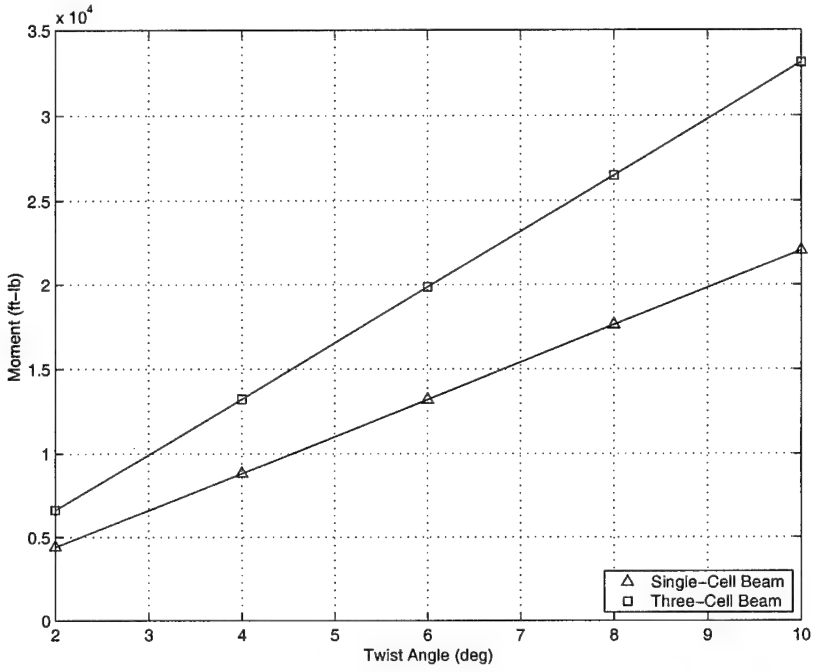

Figure 6.1 Required Moments for Single-, and Three-Cell Beam Torsion

presented in Figure (6.2). Here, the shear flows generated in the single-cell section, as well as the shear flows generated in all three sections of the three-cell beam are plotted against the imposed twist angles. It can be seen that for a given twist angle the highest skin shear flow is generated in the single-cell beam. This is due to the fact that all the shear is carried by this one section. All the shear flows in the three-cell beam are lower, because a larger

Table 6.3 **Simplified Single-Cell Torquebox Results**

	Single Cell	
Twist Angle (deg)	Shearflow (lb/in)	Moment (ft-lb)
2.0	140.3	4404
4.0	280.5	8808
6.0	420.7	13213
8.0	561.0	17617
10.0	701.2	22021

combined area of three cells is available to resist torsion. The nose and the tail sections of the three-cell beam enclose the smallest areas (see Table (2.10)), and the shear flows generated will be the least here. The shear flow in the midsection of the three-cell beam is less, but almost equal to that of the single-cell beam. Because the enclosed area of the mid section is the largest of the three cells, it will take up most of the shear load generated by the torsion.

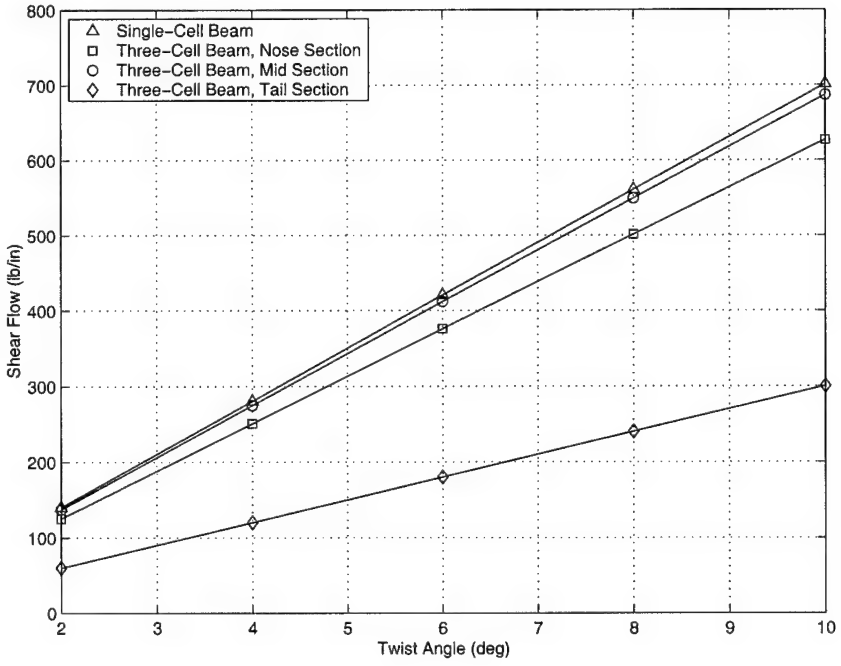

Figure 6.2 Shear Flows for Single-, and Three-Cell Beam Torsion

To check the accuracy of the solution derived in Section 4.1, it is necessary to use the simplified torquebox geometry calculated in Section 2.5.2 for obtaining the moments and shearflows for a given twist angle. See Table (2.5) for the dimensions and wall thickness of the simplified torquebox. Running the Matlab code SHEARFLOW3CELL (see Appendix B) and concentrating on the results for the (now simplified dimension) single-cell torquebox, we obtain the moments and shearflows, listed in Table (6.3).

6.2 Generalized Torsion Solution

6.2.1 Single-Cell, Isotropic Beam. In order to check the accuracy of the non-homogeneous, anisotropic solution developed in Section 4.2 for the torsional deflection of the single-cell torquebox, we can apply it to the isotropic, homogeneous case, developed in Section 4.1. The scope of the analysis covered only the applied concentrated cross-sectional moment, and it did not consider the other distributed forces and moments that may act upon the section (see Figure (4.1)). As was discussed in Section 4.1.3.2, in case of the homogeneous isotropic beam, the coupling elastic constants $\beta_2 = 0$, and $\alpha_2 = 0$. The Matlab program COMPL_ANISO_COPMZ, along with its subroutine ANISOTORSION_COMPZ (see Appendix C) was run for the isotropic (aluminum) case by setting the material properties to those of isotropic aluminum and by using the moments required to achieve the angle of twists from Table (6.3). The results were then tabulated in Table (6.4) along with the results obtained from the shearflow solution (see Table (6.3)).

The amount of twist calculated via Libove's method for the isotropic single-cell beam corresponded well to the angles obtained from the shearflow solution using the Matlab

Table 6.4 **Libove's Method for Single Cell Isotropic Beam**

	Shearflow Results	Libove's Method
Applied Moment (ft-lb)	Twist Angle (deg)	Twist Angle (deg)
4404	2.0	1.938
8808	4.0	3.875
13213	6.0	5.813
17617	8.0	7.750
22021	10.0	9.688

code SHEARFLOW3CELL (Appendix B). While the trend conserves the linearly elastic assumption made in Section 4.1.1 and demonstrates a linearly increasing deflection angle with increasing applied moment, it is only 3.1% less than the deflection angles set for the shearflow solution.

6.2.2 Single-Cell, Anisotropic Beam. To verify the accuracy of the fully anisotropic solution of Section 4.2 the results were compared to the linear case derived and experimentally tested by Romeo, et. al. in reference [24]. The authors also expanded the theory to include non-linear twist effects due to the non-linear effective shear modulus of the skin panels [24]. They used a graphite/epoxy, single-cell, rectangular cross-section, composite torquebox under pure torsion. The M40/914, $[45_2/-45_2/0_2/90_2]_s$ laminate was applied once on the top and bottom skins, and twice on the main and rear spars. The geometric and material properties of the torquebox are listed in Table (6.5). This geometry was substituted into the Matlab code COMPL_ANISO_COMPZ, which was run with the subroutine ANISOTORSION_COMPZ for several values of the applied moments listed in reference [24]. The results — tabulated in Table (6.6) — were in good agreement with the results published by Romeo.

Table 6.5 **Composite Material Properties and Geometry**

Carbon/Epoxy M40/914 Vicotex						
E_1 (Msi)	E_2 (Msi)	G_{12} (Msi)	ν_{12}	L (in)	H (in)	t_{skin} (in)
30.4	1.0	0.6	0.31	28.35	5.24	0.08

Table 6.6 **Composite Beam Torsion Verification.**

Applied Moment (ft-lb)	Skin Thickness (in)	Romeo's Method Twist Angle (deg)	Libove's Solution Twist Angle (deg)
2950	0.08	0.210	0.235
3688	0.08	0.275	0.294
4425	0.08	0.320	0.353

Having verified the accuracy of the torsion solution developed in Chapter IV by applying it to both the isotropic and anisotropic case, the program COMPL_ANISO_COPMZ was run for a fully anisotropic case using the original baseline, simplified torquebox dimensions of Section 2.5.2, by selecting the material properties of the graphite-epoxy composite listed in Table (6.7). The code was then run with its subroutines LAYUP, and ANISOTORSION_COMPZ in order to calculate the engineering properties of the composite laminate in the structural axes, to determine the composite compliance matrix S in the structural axes, and to calculate the angle of twist of the anisotropic, composite, single-cell beam. A composite laminate of Carbon/Epoxy (AS4/3501-6) with arbitrary lamina fiber orientation angles of [0/ θ /45 /-θ /0] was chosen, with a standard lamina thickness of 0.005 inch. The relevant material properties of the lamina are included in Table (6.7); however, for more information on the material, please refer to reference [11]. By varying the

Table 6.7 **Composite Material Properties**

Carbon/Epoxy AS4/3501-6				
Young's Modulus		Shear Modulus	Poisson's Ratios	
E_1 (Msi)	E_2 (Msi)	G_{12} (Msi)	ν_{12}	ν_{21}
20.6	1.50	1.04	0.27	0.02

Table 6.8 **Composite Beam Torsion. M=4404 ft-lb.**

Composite Laminate	Total Thickness (in)	Twist Angle (deg)
[0 15 45 −15 0]	0.025	4.940
[0 30 45 −30 0]	0.025	3.651
[0 45 45 −45 0]	0.025	3.513
[0 60 45 −60 0]	0.025	4.132
[0 75 45 −75 0]	0.025	4.950
[0 90 45 −90 0]	0.025	5.340

composite lamina angle θ from 0 to 90 degrees with 2-degree increments, several different fiber-orientation laminates were run to investigate how the different laminae angles affect the torquebox twist angles. Table (6.8) summarizes the tip twist angles of several selected laminate construction beams subjected to M=4404 ft-lb of cross-sectional moment. Any other distributed or concentrated forces and moments acting on the beam segment were assumed to be zero. The results are also plotted in Figure (6.3) showing the familiar pattern of the change in the angle of tip-twist due to the change in the single lamina angle θ.

Comparing the results shown in Tables (6.4) and (6.8) we come to the conclusion that the model composite laminate construction torquebox — subjected to the same cross-sectional moment — twists more than the isotropic (aluminum) beam. This is due to the fact that while the graphite-epoxy composite laminate has greater stiffness than the aluminum, we only used a five-ply, 0.025 inch thick composite laminate, compared to the aluminum beam wall thickness of 0.072 inch, 0.049 inch, and 0.048 inch for the main spar, rear spar, and skin thickness respectively, which resulted in lower torsional stiffness compared to the aluminum beam. The composite wall thickness can be increased by

increasing the number of laminae or the laminates up to the point where it satisfies the design stress requirements without a single lamina failure.

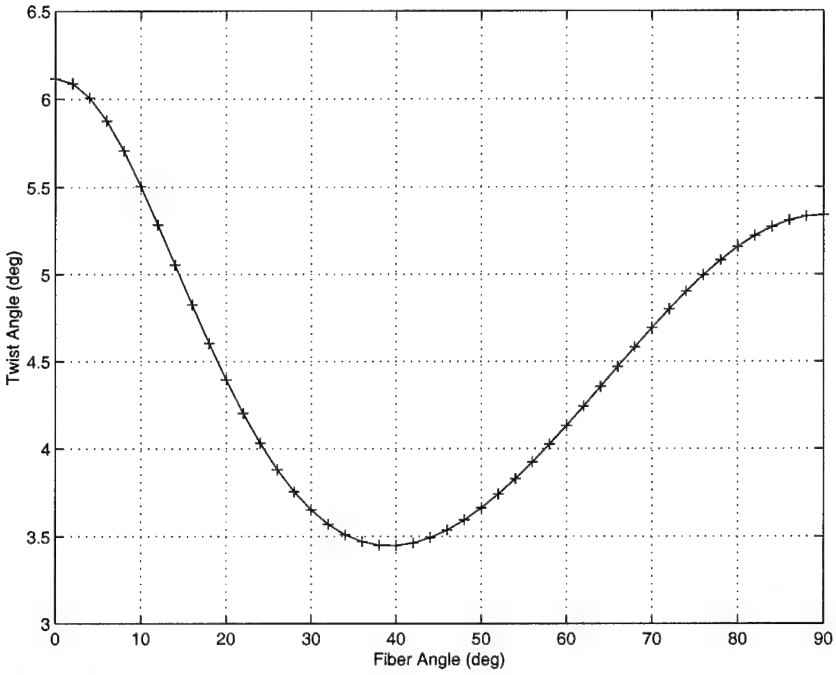

Figure 6.3 Twist Angles for the All-Composite Torquebox

6.2.3 Single-Cell, Anisotropic Composite-PZT Beam. The Matlab code COMPL_ANISO_PZT, developed in Section 5.1 to calculate the twist angle of the anisotropic composite beam, was modified so that a layer of PZT embedded in the geometric center (mid-plane) of the laminate can be accounted for while calculating the engineering properties of the laminate in the structural axes. This was achieved by ordering the laminate material properties in the material principal directions into a vector, containing the PZT material properties (E,G,ν) as an element. Because the PZT layer was assumed to be embedded in the symmetric center of the laminate, the PZT material properties were placed in the middle of the vector. The two PZT actuator laminae consid-

ered were introduced in Section 5.1.1. The mechanical properties of the AFC lamina — in form of compliance and plane-stress stiffness matrix — were obtained from a combination of experimental stress-strain, and clamped-actuation testing by Bent, et. al. [5]. These plane-stress compliance values were used to calculate the material properties of the AFC lamina in the principal directions. The material properties of the G-1195 PZT lamina were obtained from reference [3], [8], and [10]. The engineering properties of both PZT laminae in the structural directions were again obtained via the LAYUP subroutine. For more details, please refer to the Matlab code COMPL_ANISO_PZT included in Appendix D.

According to the argument made in Section 5.1.1, the PZT lamina was assumed to be at a 45 degree angle with respect to the structural z axis (see Figure (5.2)), simply replacing one layer of the graphite/epoxy lamina. Because the engineering properties of the composite-PZT laminate are different — in the material 1-2 axes, as well as in the structural z-x axes — than those of the graphite-epoxy composite laminate alone, it was necessary to calculate all the elastic coupling coefficients separately for the composite and composite-PZT hybrid laminate. Therefore, in addition to the compliance coefficients α_1, α_2, and α_3 of the composite laminate, we will have α_{p1}, α_{p2}, and α_{p3} for the hybrid composite-PZT laminate. Similarly, we obtain the values of the elastic coupling coefficients β_{p1}, β_{p2}, and β_{p3} for the composite-PZT laminate. These coefficients had to be substituted in the appropriate locations in all the partial and full-path integrals detailed in Chapter IV. These integrals were solved symbolically using MathCad, and the results were transferred to the Matlab subroutine ANISOTORSION_PZT. This subroutine, when called by the driver program COMPL_ANISO_PZT, calculates the tip twist angle due to a cross-sectional moment of M=4404 ft-lb of the single-cell, closed-section, anisotropic torquebox with PZT

Table 6.9 **PZT-Composite Beam Torsion. M=4404 ft-lb.**

	AFC Composite		G-1195 PZT	
Composite Laminate	Total Thickness (in)	Twist Angle (deg)	Total Thickness (in)	Twist Angle (deg)
[0 PZT 0]	0.0165	18.3149	0.015	19.8341
[0 15 PZT −15 0]	0.0265	6.3218	0.025	6.6210
[0 30 PZT −30 0]	0.0265	6.7207	0.025	6.8166
[0 45 PZT −45 0]	0.0265	6.6154	0.025	6.6587
[0 60 PZT −60 0]	0.0265	8.2119	0.025	8.3173
[0 75 PZT −75 0]	0.0265	10.4376	0.025	10.7839
[0 90 PZT −90 0]	0.0265	11.5805	0.025	12.1206

actuator lamina embedded in the center layer of the top and bottom skin graphite-epoxy composite laminate. The program was run for the same composite laminate construction detailed in Table (6.8) with the center 45-degree graphite-epoxy layer substituted with one layer of PZT lamina of the same orientation. Again, the two PZT-composite laminae used for comparisons were detailed in Section 5.1.1. The fiber orientation angle θ of the graphite-epoxy lamina was varied as before (see Table (6.8)), and the results are tabulated in Table (6.9) and plotted in Figure (6.4).

Both the AFC and the G-1195 PZT-Composite beam demonstrated comparable twist angles for identical cross–sectional moment for all values of the changing lamina angle. However, both beams — with the PZT layer embedded — exhibited greater tip twist angles for a given substrate lamina orientation angle than the composite–alone construction beam. This leads to the conclusion that both PZT actuator laminae, when embedded in the center of the composite laminate, lowered the beam's torsional stiffness, compared to that of the composite–alone laminate, resulting in greater beam tip twist angles. The reduction of beam stiffness was expected since the stiffness of both actuator laminae are one fourth of the stiffness of the substrate graphite/epoxy, and the shear modulus of both laminae are

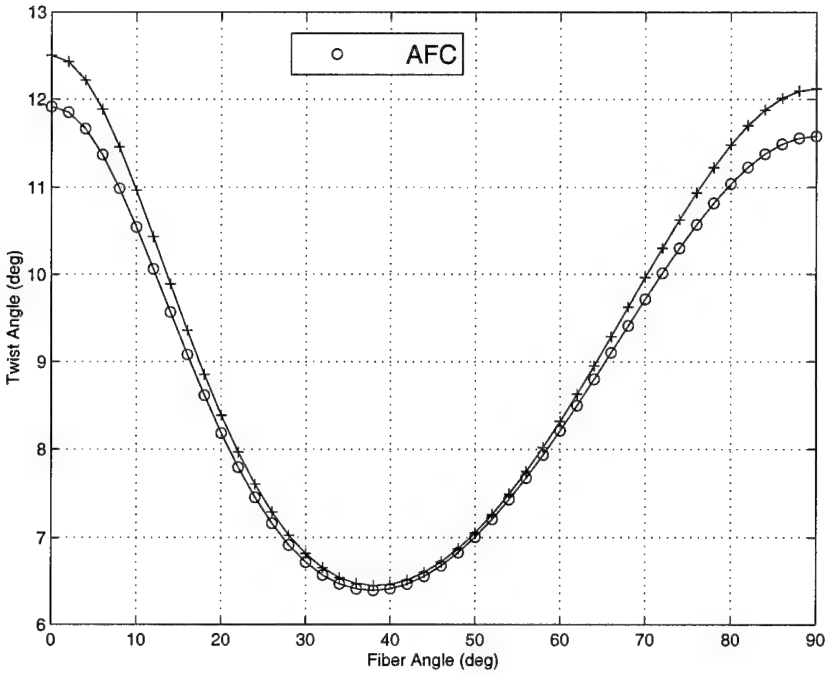

Figure 6.4 Twist Angles for the PZT-Composite Torqueboxes

an order of magnitude less than that of the substrate composite. While only static torsion is considered, the reduction in torsional stiffness may very well be a desirable effect, since a lower electric field is necessary to generate the desired angles. When dynamic effects are also considered, lowering the beam's torsional stiffness could significantly lower the wing's flutter velocity.

6.2.4 Single-Cell, Anisotropic, Composite-PZT Beam with Strain Actuation.

The driver code COMPL_ANISO_PZT was modified in order to account for the piezoelectric actuation of the embedded PZT lamina. The actuation was achieved by applying an electric field E_3 in the PZT lamina poling direction (see Figure (5.3), or Figure (5.4)). The piezoelectric strain and shear generated by the electric field was accounted for by extending the constitutive relations and re-deriving Libove's method in Section 5.2.

Table 6.10 **Strain Actuation Twist Angles - AFC Laminate**

Composite Laminate	Applied Voltage (V)				
	100	250	500	750	1000
[0 15 45 −15 0]	0.0299	0.0748	0.1495	0.2243	0.2991
[0 30 45 −30 0]	0.0270	0.0674	0.1348	0.2022	0.2696
[0 45 45 −45 0]	0.0282	0.0704	0.1409	0.2113	0.2818
[0 60 45 −60 0]	0.0323	0.0807	0.1615	0.2422	0.3229
[0 75 45 −75 0]	0.0375	0.0936	0.1873	0.2809	0.3746
[0 90 45 −90 0]	0.0400	0.0999	0.1998	0.2997	0.3996

The solution was coded as the Matlab subroutine ANISOTORSION_PZT_E. The piezoelectric strain tensor in the material principal 3-1 axes was transformed to the structural z-x axes by the Matlab subroutine TRANSFORM, using the methods of Section 5.3.

The Matlab code COMPL_ANISO_PZT_E was run for the AFC and G-1195 PZT laminate cases, using several values of the applied electric field E_3, and substrate lamina orientation angles. The results for the strain actuation of the AFC laminate beam are tabulated in Table (6.10), and — using the variable lamina angle θ as the parameter — the tip twist angles were plotted against the applied voltage in Figure (6.5). The linear trend is conserved, and the effect of the lamina angle on the tip twist for a given applied voltage is conveniently observed. For any given lamina angle θ, an increase in the applied voltage increases the beam tip twist angle. For a given applied voltage, the tip twist angle decreases until the lamina angle reaches 30 degrees. Further increase in the lamina angle increases the tip twist, indicating that the host structure's torsional stiffness is reduced when the lamina angle is greater than 30 degrees. To better observe the effect of the variable angle lamina, and to more accurately determine the variable substrate angle where the minimum twist occurs, the tip twist angles of the AFC laminate torquebox were also plotted against the variable lamina angle θ in Figure (6.6), using the applied voltage

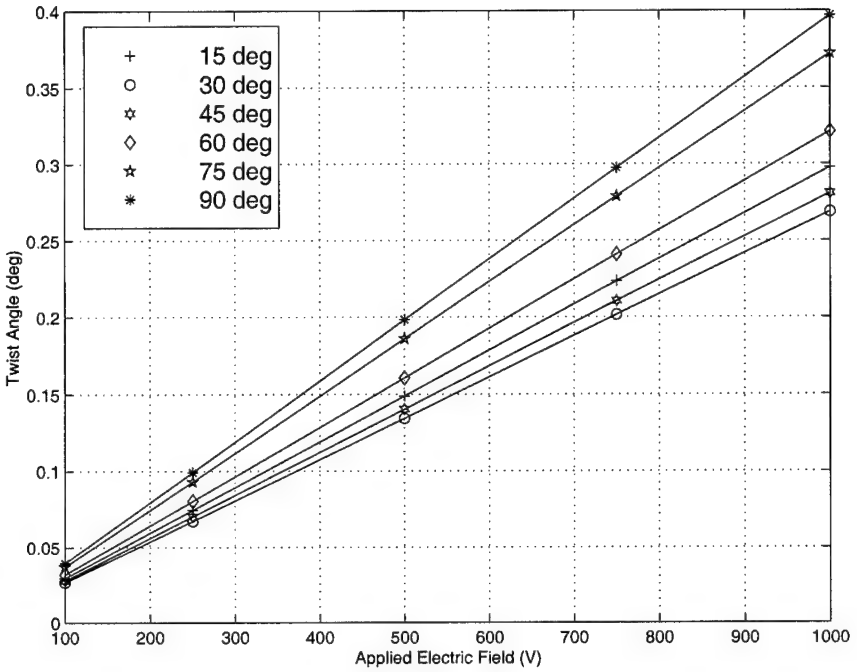

Figure 6.5 Twist Angles Due to Strain Actuation - AFC Laminate

as the parameter. The plot demonstrates how the variable lamina angle affects the tip twist for a given value of applied voltage. By inspection, the minimum twist for any given applied voltage occurs at approximately θ=33 degrees. Any increase or decrease in the lamina orientation angle will result in an increase in the tip twist angle.

The results for tip torsion, using the G-1195 PZT–composite hybrid laminate, are tabulated in Table (6.11). The tip twist angles are greater than those of the AFC laminate beam, and they correspond well to the trend observed in Table (6.10). This is partly attributed to the piezoelectric constants of the G-1195 lamina which are significantly greater than those of the AFC lamina (see Table (5.1)). The tip twist angles of the G-1195 PZT laminate torquebox are again plotted against the applied voltage in Figure (6.7), using the variable substrate lamina angle θ as the parameter. The linear trend is not conserved as before, because the induced strain increase with applied electric field, which in turn

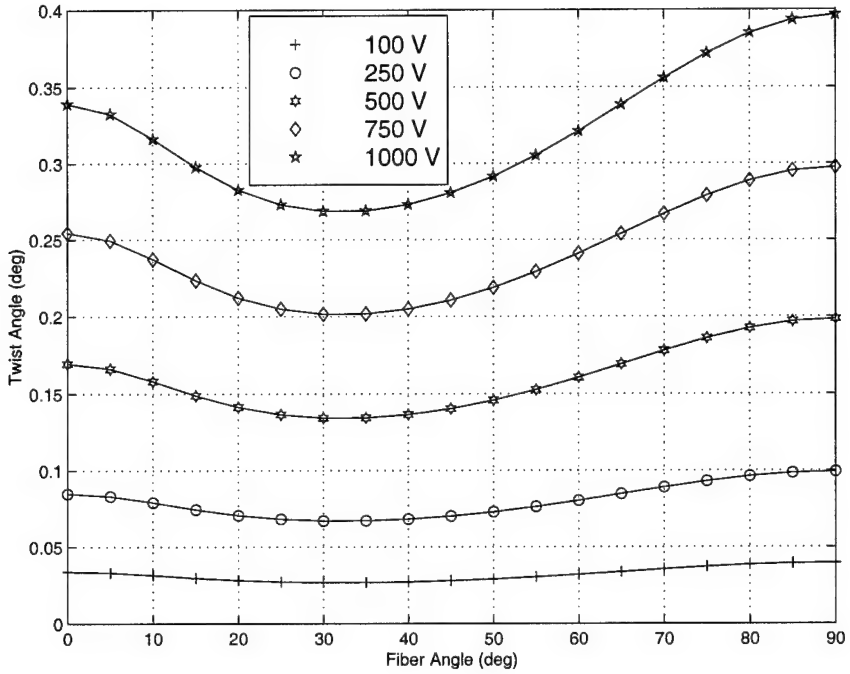

Figure 6.6 Twist Angles Due to Strain Actuation - AFC Laminate

Table 6.11 **Strain Actuation Twist Angles - G-1195 PZT Laminate**

Composite Laminate	Applied Voltage (V)				
	50	75	100	150	200
[0 15 45 −15 0]	0.1184	0.1899	0.2695	0.4533	0.6698
[0 30 45 −30 0]	0.0992	0.1590	0.2257	0.3796	0.5609
[0 45 45 −45 0]	0.1071	0.1718	0.2438	0.4101	0.6060
[0 60 45 −60 0]	0.1340	0.2149	0.3050	0.5130	0.7579
[0 75 45 −75 0]	0.1676	0.2688	0.3816	0.6418	0.9484
[0 90 45 −90 0]	0.1840	0.2951	0.4188	0.7044	1.0409

increase the value of the piezoelectric constant in the poling (d_{33}) direction. For any given substrate lamina angle, the tip twist angle increases with increasing applied voltage, while for a given applied voltage, the tip twist angle decreases until the lamina angle reaches 30 degrees. Similar to the AFC laminate case, further increase in the lamina angle increases the tip twist, indicating that the host structure's torsional stiffness is reduced when the composite lamina angle is greater than 30 degrees.

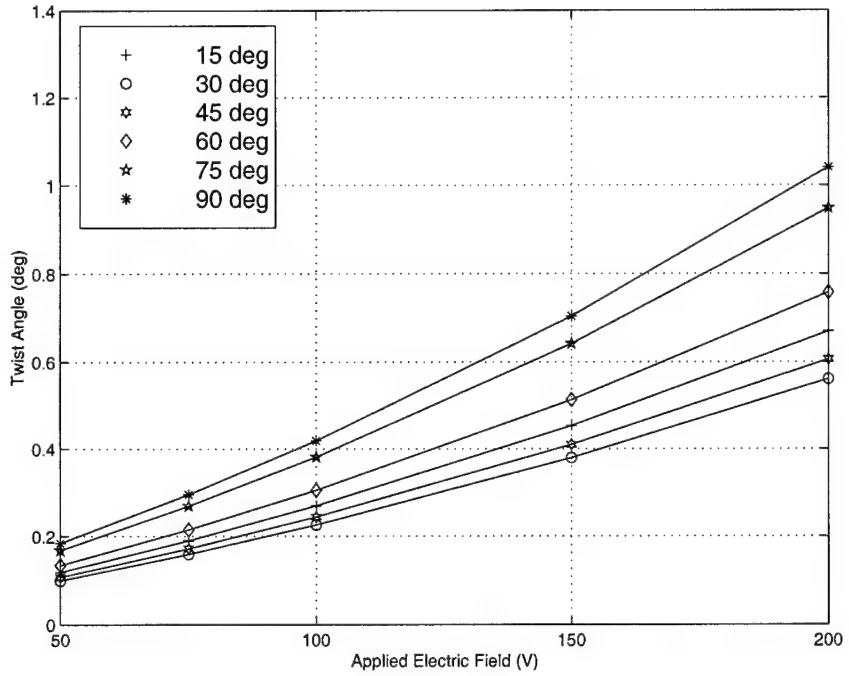

Figure 6.7 Twist Angles Due to Strain Actuation - G-1195 PZT

The tip twist angles of the G-1195 PZT laminate torquebox were also plotted against the variable lamina angle θ in Figure (6.8), using the applied voltage as the parameter. The plot demonstrates how the variable lamina angle affects the tip twist for a given value of applied voltage. By inspection, the minimum twist for any given applied voltage occurs at approximately θ=33 degrees. Any increase or decrease in the lamina orientation angle will result in the increase of the tip twist angle. The recorded tip twist angles for a given applied voltage again proved to be greater for the composite lamina orientation angle of 90 degrees, than at 0 degrees. The same result was observed when using the AFC actuator lamina.

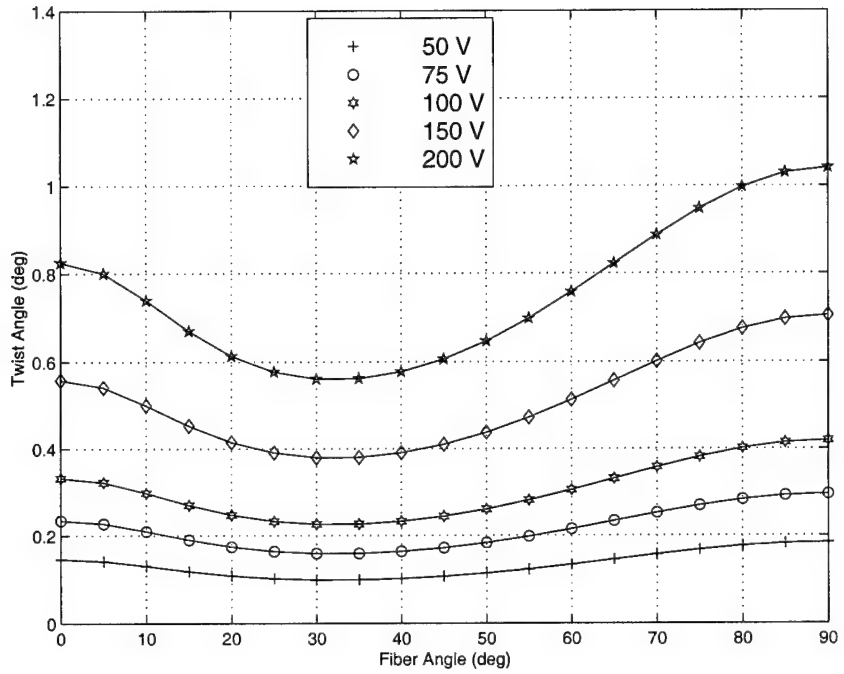

Figure 6.8 Twist Angles Due to Strain Actuation - G-1195 PZT

6.3 Discussion

The results presented for the single-, as well as the three-cell isotropic beam well demonstrated the effects of the higher torsional stiffness afforded by the multiple cell section, resulting in less tip twist. When less torsional displacement is desired, the multiple-cell construction offers better results; however, the enclosed area will be greater, requiring a larger structure. The solutions to the isotropic, single-cell trapezoid torquebox (see Table (6.3)) were prepared to verify the accuracy of the anisotropic torsion model, when applied to full isotropy.

The solution to the torsion of the single-cell, trapezoid cross-section, anisotropic beam — simplified to isotropic material properties — matched the results obtained from the isotropic solution within 3.1%. The results proved the validity of the torsion model, when used with a uniform cross-sectional moment acting on the section. The full aniso-

tropic model — with cross section and other dimensions modified to match the torquebox dimensions of reference [24] — predicted torsional displacements close to those calculated by the linear theory presented by reference [24] (see Table (6.6)). The anisotropic torsion model predicted higher angular tip displacements than those listed in reference [24]. The difference can be attributed to the approximation used in reference [24] by extending the Bredt-Batho theorem of isotropic beams to approximate the twist of anisotropic beams. Both linear models, however, underpredict the experimentally determined tip twist angles of the anisotropic beam due to assuming linear strains and rotations (Eqns. (4.20) and (5.5)), as well as constant shear stiffness. The accuracy of the method of Romeo, et. al. will increase when the incomplete diagonal shear stress field in panels operating in the post-buckling phase is accounted for [24]. While the model of anisotropic, single-cell beam torsion — derived in Chapter IV — offers higher fidelity in the linear regime, its accuracy can further be increased by accounting for non-linear translational strains, as well as non-linear curvatures about the structural axes. The accuracy can be even further increased by accounting for warping functions of various degrees (linear, or non-linear), as was discussed in Section 4.1.3.1.

The PZT lamina was embedded in the host structure (substrate), and the engineering properties of the hybrid laminate were recalculated so that the modified compliance values could be used to calculate the material elastic coupling coefficients. Both PZT laminae (the AFC of reference [5], and the G-1195 PZT lamina of reference [3]) were accounted for by using their respective material elastic and piezoelectric properties. The torquebox tip-torsion angles due to the applied voltage were recorded, tabulated, and presented in a parametric plot, using first the variable composite ply angle, then the applied voltage

as a parameter. The strain actuation plots of the AFC PZT lamina, using the composite substrate lamina angle as parameter demonstrated a linear relation between applied voltage and twist angle. The strain actuation plots of the G-1195 PZT lamina, using the composite substrate lamina angle as a parameter, demonstrated a non-linear relation between applied voltage and twist angle. This was due to the piezoelectric constant, which is a function of the induced strain of the PZT lamina. The results probably still underpredicted any experimental results due to the arguments made in the previous paragraph. Also, the angles obtained due to strain actuation are most probably insufficient to provide adequate aerodynamic control of the UAV designed in Chapter II at any airspeed within the flight envelope. The roll authority provided by the above strain actuation results can be evaluated by any available theory, such as lifting-line theory, or numerical (panel) methods.

The variation of twist angle as a function of the composite substrate lamina angle — using the applied voltage as a parameter — produced patterns similar to those obtained from the torsion of the pure composite beam, and the torsion of the PZT-composite beam Sections 6.2.2 and 6.2.3. The minimum twist angle due to constant voltage strain actuation of both PZT laminated torqueboxes occurred at the composite substrate angle of approximately 33 degrees.

Comparing the results tabulated in Tables (6.11) and (6.10), and plotted in Figures (6.6) and (6.8), the torquebox using the G–1195 PZT lamina achieved higher twist angles with lower applied voltages than the torquebox equipped with the AFC lamina. Though both piezoelectric constants of the G–1195 lamina are positive (creating strains of equal signs for a given applied electric field), they are considerably greater than those of the AFC lamina. This confirms the statement made in Section 5.1, that the PZT lamina of

high d_{33} will require less voltage to produce the necessary strains. The results also validate the claim that the higher the stiffness the larger the fraction of the strain produced by the electric field that is transferred to the host structure. That is, the actuator lamina will be compressed less, while the substrate will be strained more.

VII. Conclusions and Recommendations

7.1 Summary

This thesis detailed a method of analyzing and modeling a fully anisotropic, single-cell, closed-section, generic trapezoid cross-section torquebox under torsional deformation, using a full complement of air loads. The conceptual design of a proposed low-observable, medium-range and endurance reconnaissance UAV was accomplished in order to develop the baseline geometry for the three-cell, as well as the single-cell, isotropic wing torquebox, as well as to provide prototype dimensions for the RCS comparative study in reference [25]. The simplified single-cell torquebox dimensions were generated by assuming equal length, flat-surface wing skins between the spars as to facilitate the derivation of the fully anisotropic torsion model. The single-cell beam dimensions were then used to determine the uniform twisting moment required to generate the given amount of tip twist angles of the isotropic torquebox, as predicted by the Bredt-Batho theorem.

A torsion model was then derived for both the homogeneous and non-homogeneous anisotropic structures. The fully anisotropic case was developed based on modifying Libove's method using a thin-walled, linearly elastic, fully anisotropic, trapezoid cross-section beam. The accuracy of the torsion solution using a fully isotropic case was compared to the solution obtained for isotropic beam torsion using the Bredt-Batho theorem. The fully anisotropic case (modified to a rectangular, non-constant thickness cross-section box beam) was compared to the results published by Romeo, et. al. for anisotropic laminate box beams.

The investigation extended the analysis to include a PZT-composite actuator lamina in the mid-plane of the composite host structure's skin, and to model the piezoceramic actuation through applied piezoceramic strain and shear. The effect of the PZT-composite lamina on the torsional stiffness of the torquebox was demonstrated by applying a uniform cross-sectional moment to the hybrid composite torquebox.

The modeling of the piezoceramic actuation was accomplished by extending Libove's method derived for the anisotropic composite torquebox, to include piezoelectric strain and shear in the strain-stress constitutive relations. The torsional model was then re-derived to include the effect of PZT strain and shear present in the top and bottom skin surfaces. The PZT embedded surfaces were strain actuated by applying an electric field to the PZT actuators, inducing torsion of the host structure. The voltage generated tip torsion of the torquebox was verified by recording the angles of twist due to a range of applied voltages. The veracity of the solution was demonstrated by varying the lamina angle of two layers of the graphite-epoxy composite, and the resulting tip torsion angles were recorded.

The trend of twist angles versus substrate lamina angles corresponded to the trend observed for the composite beam torsion due to applied moment. The torsion of the torquebox due to strain actuation using two different PZT laminae were compared.

7.2 Conclusions

This research has covered a span of over six months, starting from the conceptual design and iteration of the proposed UAV. The shearflow solution to the closed-section, single-cell and three-cell isotropic torquebox torsion was developed by using the easily

applicable Bredt-Batho theorem. The derivation of the anisotropic torsion model, however, was achieved only after overcoming considerable conceptual as well as algebraic difficulties in establishing the appropriate mathematical boundary conditions and correct limits of integration for the simplified single-cell torquebox. Some difficulty was encountered in arriving at the correct plane-stress constitutive elements that were used to model the strain and shear of the composite laminate. The generating of the correct symbolic solutions of over 30 partial, as well as the full-path integrals for the piecewise continuous surfaces — that were indispensable to develop the code that automated the solution — was a particularly slow and tedious process, after which the nature of the research process became painfully obvious:

> *The research process is extremely non-linear if not discontinuous. A year's or decade's worth of work can pay off in one day. ... Be patient and persistent [6]*

Once the process was automated via the Matlab routines, the numerical results for the different cases became easier to generate.

Nevertheless, the procedure had to be completely repeated for the PZT-composite laminate case, since the plane-stress constitutive equations were modified to account for the PZT lamina, as well as for the PZT strain and shear. Once the PZT-composite solution to the integrals were completed using the appropriate elastic coupling coefficients of the composite, and that of the PZT-composite hybrid laminate, the existing Matlab routines had to be modified accordingly in order to account for the respective changes in the path integrals. Only then it became routine to generate, run, and record sample cases to test the applicability of the torsion model of the anisotropic PZT actuated composite laminate.

The model was developed in a way that is easily modified to include different composite materials, any different PZT actuator laminas, as well as any trapezoid cross-section areas (that can include rectangles, squares, or even to approximate plates), thereby providing an extremely fast and convenient tool for initial theoretical prediction of torquebox torsion in the linear regime.

7.3 Recommendations

The thesis achieved the goals set out in Section 1.3; however, it could be further expanded by investigating several other issues that are relevant to the topic of beam torsion. The study can be continued by establishing the shear-moment diagram of any desired flight condition for any of the UAV designs of Chapter II, and the incremental shear forces and bending moments along the span can be imposed upon the single-cell isotropic, or anisotropic torquebox. Strain actuation can be added to the structure if so desired. The angle of twist for a given particular, or range of loading condition can be calculated.

Also, the torqueboxes can be designed to the given maximum flight loads, so that actual composite skin and spar thickness, along with their respective lamina orientation can be used for calculating the constitutive relations, as well as the angles of twist. The design methods of Section 2.4 will have to be abandoned, as they only apply to isotropic materials.

The single-cell torquebox solution can also be expanded by considering a three-cell (or other multi-cell) beam. This can be achieved by supplementing the equations of static equivalence of Section 4.1.3.2 by the compatibility equations that require equal amount

of rotations for all sections. The PZT elements then can be applied to the surfaces of interest, and a full complement of shear loads, bending moments and strain actuation can be assumed along the span by using the methods of Chapters IV and V.

After obtaining the solution to the multi-cell torquebox, the six UAV designs developed can be used to conduct trade studies for PZT actuation requirements for different takeoff weights, aspect ratios, etc. Relations can be determined between maximum gross takeoff weight and strain actuation power requirements, given certain design variables (such as AR, wingspan, etc.) are held constant.

Once the trade studies are completed, the results could be extrapolated within a reasonable range (to be determined) and the entire process could be automated, so that intermediate values of the independent variable (weight, AR, wingspan, etc.) can be linked to the dependent variables (actuation strain, power required, etc.).

Finally, the author recommends an experimental verification of the results obtained, by constructing two trapezoid torqueboxes of any desired dimension (although I recommend the two to be the same in dimensions to ease the burden as well as lessen the expense of manufacturing), one specimen with, the other without the PZT-composite actuator. The experiment would then draw conclusions about the accuracy of the results presented in Chapter VI, as well as make suggestions for possible corrections and improvements.

Appendix A. Airfoil Profile Parameters Codes

```
function[A1,l1,A2,l21,l22,A3,l31,l32,h1,h2]=area(c11,c22,c);

%Written by Capt Peter Cseke, Jr. - Fall 1999 - AFIT/ENY
%Calculates the geometric properties of the airfoil profile
%Inputs:  NLF0215.m subroutine for airfoil input data
%         interp.m subroutine for interpolating values
%Outputs: Geometric properties of airfoil (areas, skin lengths, spar heights)

%Call the profile function for non-dimensional data
[xcupper,zcupper,xclower,zclower]=NLF0215(xcupper,zcupper,xclower,zclower);

%Count the length of the vectors for the x coordinates
%(=length of y coordinates)
nupper=length(xcupper);
nlower=length(xclower);

croot=c;
c1=c11*croot;
c2=c22*croot;

%Calculate the dimensional parameters from chord and profile data
xcupper=xcupper.*croot; zcupper=zcupper.*croot;
xclower=xclower.*croot; zclower=zclower.*croot;

%*****************************************************************
%Calculate the nose cone upper area (dA1up), and upper skin length (dl1up)

u=1;
```

```
dA1up=0.0;
dl1up=0.0;
while xcupper(u)<=c1
   x1=xcupper(u);
   x2=xcupper(u+1);
   y1=abs(zcupper(u));
   y2=abs(zcupper(u+1));
   x=x1+(x2-x1)/2;
   [y]=interp(x1,x2,x,y1,y2);

   if x2>c1
      dA1up=dA1up+(c1-x1)*y;
      dl1up=dl1up+sqrt((c1-x1)^2+(y-y1)^2);
   else
      dA1up=dA1up+(x2-x1)*y;
      dl1up=dl1up+sqrt((x2-x1)^2+(y-y1)^2);
   end

   u=u+1;
end

%Reset counter so that first index starts where we left off
u=u-1;
dA1up; %Display result if so desired
dl1up; %Display result if so desired

%Calculate the nose cone lower area (dA1low) and lower skin length (dl1low)

j=1;
dA1low=0.0;
dl1low=0.0;
while xclower(j)<=c1
   x1=xclower(j);
   x2=xclower(j+1);
```

```
   y1=abs(zclower(j));
   y2=abs(zclower(j+1));
   x=x1+(x2-x1)/2;
   [y]=interp(x1,x2,x,y1,y2);

   if x2>c1
      dA1low=dA1low+(c1-x1)*abs(y);
      dl1low=dl1low+sqrt((c1-x1)^2+(y-y1)^2);
   else
      dl1low=dl1low+sqrt((x2-x1)^2+(y2-y1)^2);
      dA1low=dA1low+(x2-x1)*abs(y);
   end

   j=j+1;
end
j=j-1;       %Reset counter so that first index starts where we left off
xclower(j);  %Display result if so desired
dA1low;      %Display result if so desired
dl1low;      %Display result if so desired

%Calculate the sum of the nose cone areas (dA1) and skin lengths (l1)
A1=dA1up+dA1low
l1=dl1up+dl1low

%*****************************************************************
%Calculate main torque box upper area (dA2up) and upper skin length (l21)
dA2up=0.0;
l21=0.0;
 while xcupper(u)<=c2
   x1=xcupper(u);
   x2=xcupper(u+1);
   y1=zcupper(u);
   y2=zcupper(u+1);
   x=x1+(x2-x1)/2;
```

```
   [y]=interp(x1,x2,x,y1,y2);

   if x2>c2                    %If beyond spar, go back so no overestimate occurs
      dA2up=dA2up+(c2-x1)*y;
      l21=l21+sqrt((c2-x1)^2+(y-y1)^2);
   else
      dA2up=dA2up+(x2-x1)*y;
      l21=l21+sqrt((x2-x1)^2+(y2-y1)^2); %Otherwise calculate area and add to sum
   end

   u=u+1;
end
u=u-1;          %Reset counter so that first index starts where we left off
xcupper(u);     %This is the value of the x coordinate where we left off above
dA2up           %Display result if so desired
l21             %Display result if so desired

%Calculate main torque box lower area (dA2low) and lower skin length (l22)
dA2low=0.0;
l22=0.0;

while xclower(j)<=c2
   x1=xclower(j);
   x2=xclower(j+1);
   y1=abs(zclower(j));
   y2=abs(zclower(j+1));
   x=x1+(x2-x1)/2;
   [y]=interp(x1,x2,x,y1,y2);

   if x2>c2
      dA2low=dA2low+(c2-x1)*abs(y);
      l22=l22+sqrt((c2-x1)^2+(y-y1)^2);
   else
      dA2low=dA2low+(x2-x1)*abs(y);
```

```
      l22=l22+sqrt((x2-x1)^2+(y2-y1)^2);
   end

   j=j+1;
end
%j=j-1;        %Reset counter so that first index starts where we left off

%The total area is the some of the upper and lower areas
A2=dA2up+dA2low

%*****************************************************************************
%Calculate trailing edge torque box upper area (A3) and upper skin length (l31)
dA3up=0.0;
l31=0.0;

while u<=nupper-1
   x1=xcupper(u);
   x2=xcupper(u+1);
   y1=zcupper(u);
   y2=zcupper(u+1);
   x=x1+(x2-x1)/2;
   [y]=interp(x1,x2,x,y1,y2);
   dA3up=dA3up+(x2-x1)*y;
   l31=l31+sqrt((x2-x1)^2+(y2-y1)^2);
   u=u+1;
end

%Calculate trailing edge torque box lower area (A3) and lower skin length (l32)
dA3low=0.0;
l32=0.0;
while j<=nlower-1
   x1=xclower(j);
   x2=xclower(j+1);
   y1=abs(zclower(j));
```

```
   y2=abs(zclower(j+1));
   x=x1+(x2-x1)/2;
   [y]=interp(x1,x2,x,y1,y2);
   %In case of reflexed lower surface:  If lower surface below chord y<0, and
   %incremental area is added (-*-=+).  If lower surface above chord y>0, and
   %incremental area is subtracted (-*+=-)
   dA3low=dA3low-(x2-x1)*y;
   l32=l32+sqrt((x2-x1)^2+(y2-y1)^2);
   j=j+1;
end
dA3low;  %Display result if so desired
l32      %Display result if so desired
A3=dA3up+dA3low

%*****************************************************************************
%Find spar heights (h1 and h2)
m=1;                                    %Upper xc loop variable initialized
n=1;                                    %Lower xc loop variable initialized

%Start with h1:
while xcupper(m)<=c1                    %Find main spar location (=c1) on upper xc
   if xcupper(m)<=c1 & xcupper(m+1)>=c1  %Find if around main spar location
      x1=xcupper(m);
      x2=xcupper(m+1);
      y1=zcupper(m);
      y2=zcupper(m+1);
      [y11]=interp(x1,x2,c1,y1,y2);      %Interpolate for upper spar height
   end
   m=m+1;
end

while xclower(n)<=c1                    %Find main spar location (=c1) on lower xc
   if xclower(n)<=c1 & xclower(n+1)>=c1  %Find if around main spar location
      x1=xclower(n);
```

```
      x2=xclower(n+1);
      y1=zclower(n);
      y2=zclower(n+1);
      [y12]=interp(x1,x2,c1,y1,y2);      %Interpolate for lower spar height
   end
   n=n+1;
end
y11
y12
h1=y11+abs(y12)                          %Calculate main spar height

%Continue with h2:
p=1;                                     %Upper xc loop variable initialized
q=1;                                     %Lower xc loop variable initialized
while xcupper(p)<=c2                     %Find rear spar location (=c2) on upper xc
   if xcupper(p)<=c2 & xcupper(p+1)>=c2  %Find if around rear spar location
      x1=xcupper(p);
      x2=xcupper(p+1);
      y1=zcupper(p);
      y2=zcupper(p+1);
      [y21]=interp(x1,x2,c2,y1,y2);      %Interpolate for upper rear spar height
   end
   p=p+1;
end

while xclower(q)<=c2                     %Find rear spar location (=c2) on lower xc
   if xclower(q)<=c2 & xclower(q+1)>=c2  %Find if around rear spar location
      x1=xclower(q);
      x2=xclower(q+1);
      y1=zclower(q);
      y2=zclower(q+1);
      [y22]=interp(x1,x2,c2,y1,y2);      %Interpolate for lower rear spar height
   end
   q=q+1;
```

```
end
y21                                     %Display result if so desired
y22                                     %Display result if so desired
h2=y21+abs(y22)                         %Calculate rear spar height
%*************************************************************************
return
```

```
function[xcupper,zcupper,xclower,zclower]=NLF0215(xcupper,zcupper,xclower,zclower)

%Written by Capt Peter Cseke, Jr. - Fall 1999 - AFIT/ENY
%Defines the geometric locus of the airfoil profile
%Inputs:  none
%Outputs: none

%The nondimensional coordinates of the NLF0215 high altitude, high endurance airfoil

xcupper=[0.0 0.0024 0.00909 0.02004 0.03527 0.05469 0.07816
0.10546 0.13635 0.17050...
      0.20758 0.24720 0.28894 0.33237 0.37702 0.42253 0.46864 0.51524 0.56247 0.61010...
      0.65752 0.70408 0.74914 0.79206 0.83222 0.86902 0.90193 0.93044 0.95409 0.97285...
      0.98710 0.99658 1.00000];
zcupper=[0.0 0.00917 0.01947 0.03027 0.04120 0.05201 0.06250
0.07247 0.08175 0.09019...
      0.09761 0.10389 0.10887 0.11240 0.11428 0.11427 0.11219 0.10784 0.10147 0.09373...
      0.08513 0.07603 0.06673 0.05746 0.04844 0.03983 0.03175 0.02428 0.01737 0.01082...
      0.00507 0.00126 0.00000];

xclower=[0.00000 0.00245 0.01099 0.02592 0.04653 0.07242 0.10324
0.13854 0.17788...
      0.22073 0.26654 0.31473 0.36468 0.41576 0.46731 0.51867 0.56920 0.61825 0.66662...
      0.71614 0.76645 0.81565 0.86198 0.90359 0.93862 0.96588 0.98504 0.99630 1.0];
zclower=[-0.00006 -0.00704 -0.01211 -0.01656 -0.02052 -0.02399
-0.02699 -0.02954...
      -0.03166 -0.03334 -0.03456 -0.03531 -0.03554 -0.03519 -0.03415 -0.03225 -0.02925...
      -0.02441 -0.01663 -0.00705 0.00167 0.00804 0.01155 0.01198 0.00990 0.00655...
      0.00323 0.00086 0.0];

return
```

```
function [y]=interp(x1,x2,x,y1,y2);

%Written by Capt Peter Cseke, Jr. - Fall 1999 - AFIT/ENY
%Linear interpolation subroutine
%Inputs:  Maximum and minimum independent variables x2 and x1
%         Maximum and minimum dependent variables y2 and y1
%         Independent variable (x) for which the dependent variable (y) is sought
%Outputs: Value y

y=y1+(x-x1)*(y2-y1)/(x2-x1);

return
```

```
%program plotprofile.m

%Written by Capt Peter Cseke, Jr. - Fall 1999 - AFIT/ENY
%Calculates and plots the geometric properties of the airfoil profile
%Uses:    NLF0215.m subroutine for airfoil input data
%Outputs: plots dimensional and non-dimensional profile

xcupper=[];zcupper=[];xclower=[];zclower=[];
%Call the profile function for non-dimensional data
[xcupper,zcupper,xclower,zclower]=NLF0215(xcupper,zcupper,xclower,zclower);

%These are some of the design variables:
b=21.33;
lam=0.40;
croot=5.08;
ctip=lam*croot;
tipoffset=(croot-ctip)/2;

%Calculate the root and tip chord length from non-dimensional data:
%x=(x/chord)*chord); z=(z/chord)*chord);
xrootup=xcupper*croot;
zrootup=zcupper*croot;
xrootlo=xclower*croot;
zrootlo=zclower*croot;

%In order to plot the tip on the same plot, we need to offset it according to taper
xtipup=xcupper*ctip+tipoffset;
ztipup=zcupper*ctip;
xtiplo=xclower*ctip+tipoffset;
ztiplo=zclower*ctip;

%Plot the non-dimensional profile picture from airfoil data
close all; figure(1) plot(xcupper,zcupper,xclower,zclower,'b-');
```

```
title(['NLF(1)-0215F Airfoil - Non-Dimensional Coordinates']);
xlabel('Station (x/c)');
ylabel('Ordinate (z/c)');

axis([0 1 -0.5 0.5]);
grid on;

%Plot the airplane-specific root and tip profiles:
figure(2) plot(xrootup,zrootup,xrootlo,zrootlo,'b-');
hold on;
plot(xtipup,ztipup,'m-',xtiplo,ztiplo,'m-');
hold off;
title(['NLF(1)-0215F Airfoil Root and Tip Profiles']);
xlabel('Station (ft)');
ylabel('Ordinate (ft)');

axis([0 croot -croot/2 croot/2]);
grid on;
```

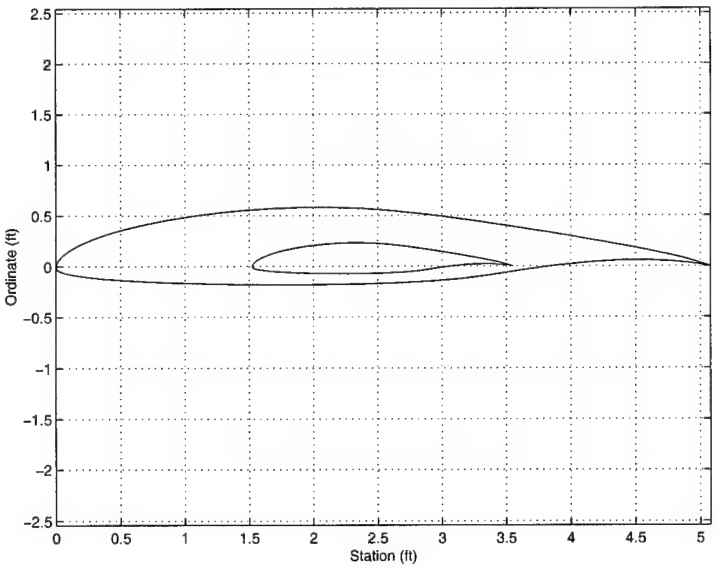

Figure A.1 The NLF(1)-0215F High-Endurance Airfoil Profile at Wing Root and Tip (No Washout)

Appendix B. Isotropic Beam Torsion Codes

```
%program shearflow3cell

%Calculate the moments required and shearflows generated by achieving desired
%twist per unit length of a single-, and three-cell, closed-section torque box :

%Written by Capt Peter Cseke, Jr. - Fall 1999 - AFIT/ENY
%Calculates the shear flow in three-cell, closed section box beam due to imposed tip
%twist angle.  It also calculates the necessary concentrated tip moment.
%Uses   : area.m
%Outputs: shear flows, moment

close all;
clear all;

%Input Profile parameters
L=21.33;                %Spanwise lenght of torque box (ft)
spar1=0.25;             %Location of Main Spar (% chord)
spar2=0.70;             %Location of Rear Spar (% chord)
chord=5.08;             %Chord Length at station (ft)

plotprofile(L,chord);   %Plot the picture of the 2-D profile (if so desired)

t1=0.048;               %Thickness (in) of nose cone skin (Area 1)
t2=t1;                  %Thickness (in) of torque box skin (Area 2)
t3=t1;                  %Thickness (in) of rear surface skin (Area 3)
ts1=0.072;              %Thickness (in) of main spar
ts2=0.049;              %Thickness (in) of rear spar
```

```
c=chord*12;                %Convert chord length to inches
Lt=L*12;                   %Convert spanwise length to inches

%Call the function that calculates the profile geometric parameters.  Send spar
%locations as non-dimensional (x/c), send chord length (c) in inches.
[A1,l1,A2,l21,l22,A3,l31,l32,h1,h2]=area(spar1,spar2,c);
A2=188.4158;
%*****************************************************************************
%Select the material properties of the beam:
E=10.4*10^6;                    %Young's Modulus for Aluminum 2024-T3 [psi]
G=3.86*10^6;                    %Shear Modulus for Aluminum 2024-T3 [psi]
rhosp=0.101;                    %Density for Aluminum 2024-T3 [lb/in^3]
Gspar1=G;

%Designate the Shear Modulus of the spar as the reference shear modulus
G0=Gspar1;
%The rear spar is made of identical material as main spar:
Gspar2=Gspar1;
rhosk=rhosp;
Gskin=Gspar1;

%*****************************************************************************
Gstar=Gskin/G0;             %Define the Weighted Shear Modulus


%*****************************************************************************
%Calculate and plot moment required for generating the given angle of twist
%for single-cell, closed section torquebox.

close all;

d=(1/2)*c*(spar2-spar1)     %Half distance between spars

thetamin=2;                 %The given degrees of twist
```

```
thetamax=10;
increment=2;
j=0;

%Generate plot of required moment versus angle of twist for single cell beam
for i=thetamin:increment:thetamax;
   theta=i;
   j=j+1;
   thetarad=theta*pi/180;      %The twist in radians
   thetarad_unit=thetarad/Lt;  %The twist per unit length in radians/in

   %Calculate shear flow due to moment
   q(j)=thetarad_unit*(2*A2*G)*(1/(l21/t2+h2/ts2+l22/t2+h1/ts1))

   %Calculate the moment [in-lb] required for twist:
   Mt=2*A2*q(j);
   M(j)=Mt/12
   angle(j)=theta;
end

%Calculate the Moment and shear-flow for simplified torquebox:
T=sqrt(1+((h2-h1)/(4*d))^2);    %The path length correction constant
A_s=2*d*(0.5*h1+0.5*h2);        %The simplified torque-box area

q_s=thetarad_unit*(2*A2*G)*(1/(4*T*d/t2+h2/ts2+l22/t2+h1/ts1));

Mt_s=2*A_s*q_s;                 %The Moment (in-lb) required for twist
M_s=Mt_s/12;                    %The Moment (ft-lb) required for twist

%*****************************************************************************
%Calculate and plot moment required for generating the given angle of twist
%for three-cell, closed section torquebox.

%Calculate the constants obtained by solving the Theta1 continuity relations
```

```
%for q1 (shear flow in nose torque box) in terms of q2 and q3, and substituting
%back into the Theta2=Theta3 continuity relation, solving for q3 (shear flow in
%trailing edge torque box) in terms of q2:
C1=l21/(Gstar*t2)+(h2/ts2)+(l22/(Gstar*t2))+(h1/ts1)+(A2*h2/(A3*ts2));
C2=(l1/(Gstar*t1)+(h1/ts1)+(A1*h1/(A2*ts1)));
C3=(A2/A3)*(l31/(Gstar*t3)+l32/(Gstar*t3)+h2/ts2);
C4=(A1/A2)*(l21/(Gstar*t2)+h2/ts2+l22/(Gstar*t2)+h1/ts1);

%Substitute q3 into the q1 equation, and solve for q1 in terms of q2 only.
%Express in terms of constants:
S3=(C1*C2-(C4*h1/ts1)-(h1/ts1)^2)/(C2*C3+h2/ts2-(h1*h2/(ts1*ts2)));
S1=(C4+(h1/ts1)-(h2/ts2)*S3)/(l1/(Gstar*t1)+h1/ts1+(A1*h1/(A2*ts1)));

%*************************************************************************
%Calculate the effective torsional Stiffness for each subsection
GJeff1=(4*A1^2)/((l1/(Gskin*t1))+(h1/(G0*ts1)));
GJeff2=(4*A2^2)/((l21/(Gskin*t2))+(l22/(Gskin*t2))+(h1/(G0*ts1))+(h2/(G0*ts2)));
GJeff3=(4*A3^2)/((l31/(Gskin*t3))+(l32/(Gskin*t3))+(h2/(G0*ts2)));
GJeff=GJeff1+GJeff2+GJeff3

thetamin=2;                %Degrees of twist required at tip (end of torquebox)
j=0; for i=thetamin:increment:thetamax;
   theta=i;
   j=j+1;
   angle(j)=theta;
    thetarad=theta*(pi/180);        %Convert degrees to radians
    thetaunit=thetarad/Lt;          %Radians of twist per unit length (rad/in)

    %The applied moment required to achieve the required twist per unit length:
    Mt(j)=(GJeff)*thetaunit;        %in-lb

    %Then the shear flow in the second subsection
    q2(j)=Mt(j)/(2*(A1*S1+A2+A3*S3))
```

```
    %Express q1 and q3 in terms of the constants multiplying q2:
    q1(j)=S1*q2(j)                  %=q1=Mt/(2*(A1+A2/S1+A3*S3/S1))
    q3(j)=S3*q2(j)

    Mtftlb(j)=Mt(j)/12                                          %ft-lb
    %The total moment can also be calculated from:
    Mtsum=2*(A1*q1+A2*q2+A3*q3);                                %in-lb
    %This should yield identical answer to Mtftlb:
    Mt2=Mtsum/12;                                               %ft-lb

    %The in-plane shear stress (psi) in the skin of the nose torque box:
    sigma1skin(j)=q1(j)/t1;
    %The in-plane shear stress (psi) in the skin of the main torque box:
    sigma2skin(j)=q2(j)/t2;
    %The in-plane shear stress (psi) in the skin of the trailing edge box:
   sigma3skin(j)=q3(j)/t3;
end

%Plot the single-cell and three-cell torque box required moments to generate
%given angle of tip twists
figure(1);
plot(angle,M,'b^',angle,Mtftlb,'rs');
hold on;
title(['Required Moments for Single- and Three-Cell Beam
Torsion']);
ylabel('Moment (ft-lb)');
xlabel('Twist Angle (deg)');
legend('Single-Cell Beam','Three-Cell Beam',4);
plot(angle,M,'b-',angle,Mtftlb,'r-');
grid on; hold off;

%Plot the single-cell and three-cell torque box shear flows generated by
%given angle of tip twists
figure(2);
```

```
plot(angle,q,'b^',angle,q1,'rs',angle,q2,'go',angle,q3,'md'); hold
on; title(['Shear Flows for Single- and Three-Cell Beam
Torsion']); ylabel('Shear Flow (lb/in)'); xlabel('Twist Angle
(deg)'); legend('Single-Cell Beam','Three-Cell Beam, Nose
Section',...
   'Three-Cell Beam, Mid Section','Three-Cell Beam, Tail Section',2);
plot(angle,q,'b-',angle,q1,'r-',angle,q2,'g-',angle,q3,'m-'); grid
on; hold off;
```

Appendix C. Anisotropic Composite Beam Torsion Codes

```
%Program Compl_aniso_compz.m

%Written by Capt Peter Cseke, Jr. - Fall 1999 - AFIT/ENY
%Driver program to Matlab functions  Layup.m
%                                    Anisotorsion_compz.m
%Defines trapezoid single-cell box beam geometric and material properties, applied
%cross section loads and moments. Calculates tip twist angle of box beam.
%
%Uses   :  Layup.m to calculate engineering properties of composite lamina.
%          Anisotorsion_compz.m to calculate twist angle of box beam.
%Outputs:  Tip twist angle of box beam.
%
%User enters:
%orientation: [0 45 -45 90 -90] etc, as a row vector;
%times      : The number of times ply is repeated;
%symmetry   : 0 for no;
%             1 for yes
%Example    : [0 45 -45 90]4s
%             orient = [0 45 -45 90]
%              times = 4
%                sym = 1
%Note       : all properties are vectors with properties per ply.
%Limits     : Assumes weighted center of laminate is at h/2.
%*****************************************************************************
close all;
clear all;

%Define beam geometric parameters
cr=60.96;               %Root chord length [in]
```

```
c1=0.25;c2=0.70;        %Main spar and Rear spar location in chord percent
h1=8.4334;              %Height if Main Spar [in]
h2=5.3035;              %Height of Rear Spar [in]
l21=27.7732;            %Length of top surface skin between Main and Rear Spars [in]
l22=29.2992;            %Length of bottom surface skin between Main and Rear Spars [in]
L=255.96;               %Spanwise length of torque box [in]

%Define the Loads and Moments acting:
P=0;                    %Spanwise extensional load  [lb]
Vx=0;                   %Vertical shear load (lift) [lb]
Vy=0;                   %Horizontal shear load (drag) [lb]
Mx=0;                   %Applied moment about x axis (bending) [in-lb]
My=0;                   %Applied moment about y axis (bending) [in-lb]
M_ftlb=4404;            %Applied moment about z axis (torque) [ft-lb]
M=M_ftlb*12;            %                                     [in-lb]

%*****************************************************
%Carbon/Epoxy (AS4/3501-6)
E1=20.6*10^6;           %Young's Modulus (fiber direction)
E2=1.50*10^6;           %Young's Modulus (matrix direction)
G12=1.04*10^6;          %Shear Modulus (in-plane)
v12=0.27;               %Poisson's Ratio
v21=0.02;               %Poisson's Ratio

%*****************************************************************************
theta=45;           %Center composite fiber rotation angle (deg)
times=1;            %Number of time lamina is wound
sym=1;              %Symmetry of lamina 0=no,1=yes
thick=0.005;        %Thickness per layer of angle lamina (given by material props.)
t=[thick];          %Thickness vector per layer of lamina

%*****************************************************************************
%Define layer of angled lamina (only one layer of variable) orientation angles
anglemin=10;
```

```
angleincr=5;
anglemax=15;

count=0;              %Reset the loop-count variable (# of angles)
j=1;
for j=anglemin:angleincr:anglemax  %Loop through the angle range

   count=count+1;
   angle(count)=j;   %Form the angle vector for the plot
    %*****************************************************************************
    %Define one layer of angled lamina orientation angles
    orientcom=[45 45 -45 -45 0 0 90 90];

    %*****************************************************************************
    %Redefine thicknesses according to number of plies
    t1=times*thick*length(orient)*(sym+1); %Total thickness of laminate at main spar
    t2=t1;                                 %Total thickness of laminate at rear spar
    ts=t1;                                 %Total thickness of laminate at skin

    %*****************************************************************************
    %Form the material properties for each angle ply (number of angle ply from orient)
    E1x=ones(size(orientcom))*E1;
    E2x=ones(size(orientcom))*E2;
    G12x=ones(size(orientcom))*G12;
    v12x=ones(size(orientcom))*v12;
    tx=ones(size(orientcom))*t;

    %*****************************************************************************
    %Calculate engineering properties of the composite laminate in the structural axes:
    [Ex,Ey,Gxy,a,vxy,vyx,nsx,nxs,nys,nsy]=Layup(E1x,E2x,v12x,G12x,tx,orientcom,times,sym);

    %Calculate the tip twist angle for the composite construction torquebox
    [S,fideg]=Anisotorsion_compz(cr,c1,c2,h1,h2,l21,l22,t1,t2,ts,L,P,Vy,Vx,Mx,My,M,...
                                 Ex,Ey,Gxy,vxy,vyx,nsx,nxs,nys,nsy);
```

```
    twist(count)=fideg;

end

twist
%Declare plot style lines and markers
linestyle=['b- ';'g- ';'r- ';'m- ';'c- ';'k- ';'y- '];
markstyle=['b+ ';'go ';'rh ';'md ';'cp ';'k* ';'yv '];

figure(1) plot(angle,twist,markstyle(1,:)); hold on;
plot(angle,twist,linestyle(1,:)); hold on;

title(['Twist Angles Due To Uniform Moment']);

ylabel('Twist Angle(deg)');
xlabel('Fiber Angle (deg)');
grid on;
```

```
%Function Anisotorsion_compz

%Written by Capt Peter Cseke, Jr. - Fall 1999 - AFIT/ENY
%Calculates the tip twist angle of the single-cell trapezoid box-beam using
%Libove's solution
%Uses:      Box beam geometric and material parameters are input from driver program
%Outputs:   Tip twist angle in degrees.
%Comment:   Also works for isotropic torsion, due to fact that Beta2=0 for
%           isotropic materials.

function
[S,Fideg]=Anisotorsion_compz(cr,c1,c2,h1,h2,l21,l22,t1,t2,ts,L,P,Vy,Vx,Mx,My,M,...
                             Ex,Ey,Gxy,vxy,vyx,nsx,nxs,nys,nsy);

%************************************************************************
%Define the half-width (d), and top surface length correction factor (T)
d=cr*(c2-c1)/2;
T=sqrt(1+((h2-h1)/(4*d))^2);
Area=2*d*(h1/2+h2/2);

%Calculate distance from origin to top and bottom surfaces (approximation)
m=(h1+h2)/4;

%The Compliance Matrix in the x-y structural axes:
S11=1/Ex; S12=-vyx/Ey; S14=nsx/Gxy;

S21=-vxy/Ex; S22=1/Ey; S24=nsy/Gxy;

S41=nxs/Ex;  S42=nys/Ey; S44=1/Gxy;

S=[S11 S12 S14;S21 S22 S24;S41 S42 S44];

%Define elastic constants for constitutive relations:
```

```
alfa1=S11;alfa2=S14;alfa4=S44;

%Define elastic constants for force-strain relations:
B1=1/alfa1;B2=-alfa2/alfa1;B4=alfa4-(alfa2^2/alfa1);

%Define the elements of the B matrix:
b11=4*B1*ts*d*T+B1*t2*h2+B1*t1*h1; b12=0; b13=-B1*d*(t2*h2-t1*h1);

b21=0;
b22=(-1/12)*B1*(t2*h2^3+4*ts*d*T*h2^2+4*ts*d*T*h1*h2+t1*h1^3+4*ts*d*T*h1^2);
b23=0;

b31=B1*d*(t2*h2-t1*h1);
b32=0;
b33=(-1/3)*B1*d^2*(4*ts*d*T+3*t2*h2+3*t1*h1);

B=[b11 b12 b13;b21 b22 b23;b31 b32 b33];
A=inv(B);
a11=A(1,1);a12=A(1,2);a13=A(1,3);
a21=A(2,1);a22=A(2,2);a23=A(2,3);
a31=A(3,1);a32=A(3,2);a33=A(3,3);

a4=8*m*B1*d^2*T^2*ts+4*d^2*B1*h1*ts*T+d*B1*h1*t2*h2+(1/2)*d*B1*t1*h1^2+...
   4*d^3*B1^2*T^2*t2^2*h2+2*d^2*B1*T*ts*h2+d^2*B1^2*T*t2^2*h2^2+...
   2*m*B1*d*T*t2*h2;
a5=(1/12)*B1*d*(-t1*h1^3+t2*h2^3+6*ts*T*d*h2^2+6*ts*T*d*h2*h1+8*m*ts*T^2*d*h2+...
   16*m*ts*T^2*d*h1);
a6=(1/2)*B1*d^2*(4*m*t2*T*h2+2*h1*t2*h2-t1*h1^2+t2*h2^2);

%Define the elements of the C matrix:
c11=B2*h2-B2*h1; c21=B2*d*T*(h2+h1); c31=B2*d*(h2+h1);

c12=4*B1*ts*d^2*T^2*B2-4*B2*B1^2*d^2*T^2*t2^2*h2-2*B2*B1*d*T*ts*h2...
   -B2*B1^2*d*T*t2^2*h2^2+2*B2*B1*d*T*t2*h2+4*B1*B2*h1*ts*d*T...
```

```
   +B2*B1*h1*t2*h2+B2*B1*h1^2*t1/2;
c22=(-1/12)*B2*B1*(-t1*h1^3+6*h2^2*t2*d*T+6*h2*h1*t2*d*T+24*ts*h2*d^2*T^2-...
   2*d*T*B1*t2^2*h2^3);
c32=(-1/6)*B2*B1*d*(8*ts*d^2*T^2+6*h1*h2*t2+12*ts*T*d*h2+24*ts*h1*d*T...
   +3*t1*h1^2+24*T^2*d^2*B1*t2^2*h2+6*d*T*B1*t2^2*h2^2);

c13=(1/12)*B1*B2*(t1*h1^3+6*ts*d*T*h2^2+6*ts*d*T*h1*h2+t2*h2^3);
c23=(1/4)*(B1*B2*ts*T^2*d^2*(h2^2+h1^2+2*h1*h2));
c33=(1/12)*B1*B2*(-t1*h1^3+6*ts*d*T*h2^3+6*ts*d*T*h1*h2+t2*h2^3);

c14=(-1/6)*B1*B2*d*(-3*t1*h1^2+6*h1*h2*t2+8*ts*d^2*T^2+12*t2*d*T*h2-3*t2*h2^2);
c24=(1/12)*B1*B2*d*(6*h2^2*t2*d*T+6*h2*h1*t2*d*T-h2^3*t2+t1*h1^3);
c34=(1/2)*B1*B2*d^2*(2*h1*h2*t2-t1*h1^2+h2^2*t2);

C=[c11 c12 c13 c14;c21 c22 c23 c24;c31 c32 c33 c34];

%Define the elements of the D vector:
d1=B4*(4*d*T*t1*t2+ts*t1*h2+ts*t2*h1)/(ts*t2*t1);
d2=(-1/2)*B4*B1*(8*d^2*T^2*ts*t1*B1*t2^2*h2+4*d*T*ts^2*t1*h2...
   +2*d*T*ts*t1*B1*t2^2*h2^2+4*t2^2*t1*d*T*h2+16*d^2*T^2*t2*ts*t1+...
   8*t2*ts^2*h1*d*T+2*ts^2*ts*h1*h2+t2*ts*t1*h1^2)/(t2*ts*t1);
d3=(1/12)*B4*B1*(-t2*h1^3+t2*h2^3+6*ts*d*T*h2^2+6*ts*d*T*h1*h2+16*t2*d^2*T^2*h1...
   +8*t2*d^2*T^2*h2)/t2;
d4=(-1/2)*B4*B1*d*(-4*t1*t2*d*T*h2-ts*t1*h2^2+ts*t1*h1^2-2*ts*h1*t2*h2)/(ts*t1);

%Define the shear flow at s=0:
q0=(1/(2*Area))*(M-a22*a5*Vy+(a13*a4-a33*a6)*Vx);

%Define the derivatives of the longitudinal strain, and curvatures:
e0p=a13*Vx;
Kxp=a22*Vy;
Kyp=a33*Vx;

%Define the values for the Q's:
```

```
Q1=c11*q0+c12*e0p+c13*Kxp+c14*Kyp;
Q2=c21*q0+c22*e0p+c23*Kxp+c24*Kyp;
Q3=c31*q0+c32*e0p+c33*Kxp+c34*Kyp;

e0=a11*(P-Q1)-a12*(Mx+Q2)-a13*(My+Q3);
Kx=a21*(P-Q1)-a22*(Mx+Q2)-a23*(My+Q3);
Ky=a31*(P-Q1)-a32*(Mx+Q2)-a33*(My+Q3);

%The rotation in radians per unit length:
dFdz=(1/(2*Area))*(-e0*c11+Kx*c21+Ky*c31+q0*d1+e0p*d2+Kxp*d3+Kyp*d4);

%The rotation in degrees per unit length:
dfdz_deg=dFdz*180/pi;

%The rotation in degrees for entire length of beam:
Fideg=dfdz_deg*L; return
```

```
%Function Layup

%Calculates engineering properties of laminate consisting of uniform lamina,
%and orientation angles.
%Input:  Composite lamina properties in material 1-2 axes
%Return: Laminate engineering properties for the purposes of stiffness (C) and
%        compliance matrix (S) calculations.

function
[Ex,Ey,Gxy,a,vxy,vyx,nsx,nxs,nys,nsy]=Layup(E1,E2,v12,G12,t,orient,times,sym)
%*************************************************************************
%       Layup(E1, E2, v12, G12, t, orient, times, sym)
%       E1:     lamina Young's Modulus (1 direction) per ply
%       E2:     lamina Young's Modulus (2 direction) per ply
%       v12:    lamina Poisson's Ratio per ply
%       G12:    lamina Shear Modulus per ply
%       t:      vector of lamina thickness per ply
%       orient: vector of orientations in degrees
%       times:  Multiples of orient
%       sym:    Symmetric? (0 = NO, anything else means yes)
%
%       Example:   [0 45 -45 90]4s
%         orient = [0 45 -45 90]
%          times = 4
%            sym = 1
%
%       note: all properties are vectors with properties per ply.
%       Assumes midplane = h/2.
%
%       Written by: Capt Jim Rogers
%       Modified by: Capt Peter Cseke

A=zeros(3,3); B=A; D=A;
```

```
for i=1:times
   E1ex((i-1)*length(E1)+1:i*length(E1))=E1;
   E2ex((i-1)*length(E2)+1:i*length(E2))=E2;
   v12ex((i-1)*length(v12)+1:i*length(v12))=v12;
   G12ex((i-1)*length(G12)+1:i*length(G12))=G12;
   tex((i-1)*length(t)+1:i*length(t))=t;
   orientex((i-1)*length(orient)+1:i*length(orient))=orient;
end if sym ~= 0
   E1ex(2*length(E1ex):-1:length(E1ex)+1)=E1ex;
   E2ex(2*length(E2ex):-1:length(E2ex)+1)=E2ex;
   v12ex(2*length(v12ex):-1:length(v12ex)+1)=v12ex;
   G12ex(2*length(G12ex):-1:length(G12ex)+1)=G12ex;
   tex(2*length(tex):-1:length(tex)+1)=tex;
   orientex(2*length(orientex):-1:length(orientex)+1)=orientex;
end

%The number of laminas (in one ply)
n=length(orientex);

tott=sum(tex); h=zeros(n+1,1);

h(1)=-tott/2; for i=2:n+1
   h(i)=sum(tex(1:i-1))-tott/2;
end

for i=1:n
   %From the symmetry of the compliance matrix:
   v21=v12ex(i)*E2ex(i)/E1ex(i);
   q11=E1ex(i)/(1-v12ex(i)*v21);

   %Equation (3.56)
   Q12=[  q11          v21*q11             0;
        v21*q11    q11*E2ex(i)/E1ex(i)     0;
```

```
          0           0              G12ex(i)];

   %Equation (3.59)
   mc=cos(orientex(i)*pi/180);
   ns=sin(orientex(i)*pi/180);
   T=[mc^2 ns^2 2*mc*ns; ns^2 mc^2 -2*mc*ns; -mc*ns mc*ns mc^2-ns^2];
   Q12(:,3)=2*Q12(:,3);

   %Equation (3.66)
   Qxy=T\Q12*T;

   %Reset the actual value of the 3rd column of Q12
   Q12(:,3)=Q12(:,3)/2;

   %Divide 3rd column by 2
   Qxy(:,3)=Qxy(:,3)/2;

   %Calculate laminate stiffness matrices (Eq. 5.20)
   A=A+Qxy*(h(i+1)-h(i));
   B=B+Qxy*(h(i+1)^2-h(i)^2)/2;
   D=D+Qxy*(h(i+1)^3-h(i)^3)/3;
end

%Calculate the laminate compliance matrices (Eq. 5.27)
Bs=-A\B; Cs=B/A; Ds=D-B*(A\B);
%The laminate extensional compliance matrix (S):
a=inv(A)-Bs*(Ds\Cs);

%Calculate laminate engineering properties (barred values) referenced to
%x and y axes (including Poisson's ratios, and shear-coupling coefficients):
Ex=1/tott/a(1,1);
Ey=1/tott/a(2,2);
Gxy=1/tott/a(3,3);
vxy=-a(2,1)/a(1,1);
```

```
vyx=-a(1,2)/a(2,2);

nsx=a(1,3)/a(3,3);

nxs=a(3,1)/a(1,1);

nys=a(3,2)/a(2,2);

nsy=a(2,3)/a(3,3);


return
```

Appendix D. Anisotropic

Composite-PZT Beam Torsion Codes

```
%Program Compl_aniso_pzt.m

%Written by Capt Peter Cseke, Jr. - Fall 1999 - AFIT/ENY
%Driver program to Matlab functions  Layup.m
%                                    Anisotorsion_pzt.m
%Defines trapezoid single-cell box beam geometric and material properties, applied
%cross section loads and moments.  %Calculates tip twist angle of box beam.
%
%Uses   :  Layup.m for engineering properties of lamina and composite-pzt lamina.
%          Anisotorsion_pzt.m to calculate twist angle of box beam.
%Outputs:  Tip twist angle of box beam.
%
%User enters:
%orientation: [0 45 -45 90 -90] etc, as a row vector;
%times      : The number of times ply is repeated;
%symmetry   : 0 for no;
%             1 for yes
%Example    : [0 45 -45 90]4s
%             orient = [0 45 -45 90]
%              times = 4
%                sym = 1
%User enters: Loading condition on cross section (P,Vx,V,Mx,My,M=Mz)
%             Select PZT laminate material properties from available choices
%Note       : all properties are vectors with properties per ply.
%Limits     : Assumes weighted center of laminate is at h/2.
%*****************************************************************************
close all;
clear all;
```

```
%Define beam geometric parameters
cr=60.96;               %Root chord length [in]
c1=0.25;c2=0.70;        %Main spar and Rear spar location in chord percent
h1=8.4334;              %Height if Main Spar [in]
h2=5.3035;              %Height of Rear Spar [in]
l21=27.7732;            %Length of top surface skin between Main and Rear Spars [in]
l22=29.2992;            %Length of bottom surface skin between Main and Rear Spars [in]
%t1=0.072;              %Main Spar thickness [in]
%t2=0.049;              %Rear Spar thickness [in]
%ts=0.048;              %Skin thickness (t1=t2) [in]
L=255.96;               %Spanwise length of torque box [in]

%Define the Loads and Moments acting:
P=0;                    %Spanwise extensional load  [lb]
Vx=0;                   %Vertical shear load (lift) [lb]
Vy=0;                   %Horizontal shear load (drag) [lb]
Mx=0;                   %Applied moment about x axis (bending) [in-lb]
My=0;                   %Applied moment about y axis (bending) [in-lb]
M_ftlb=4404;            %Applied moment about z axis (torque) [ft-lb]
M=M_ftlb*12;            %                                     [in-lb]

%*****************************************************
%Carbon/Epoxy (AS4/3501-6)
E1=20.6*10^6;           %Young's Modulus (fiber direction)
E2=1.50*10^6;           %Young's Modulus (matrix direction)
G12=1.04*10^6;          %Shear Modulus (in-plane)
v12=0.27;               %Poisson's Ratio
v21=0.02;               %Poisson's Ratio
thick=0.005;            %Thickness per layer of angle lamina (given by material props.)

%*****************************************************
%Piezoceramic Lamina
E1pzt=4.6786*10^6;      %Young's Modulus (AFC)(poling, long. or fiber direction psi)
```

```
E2pzt=2.4173*10^6;      %Young's Modulus (AFC) (transverse direction)(psi)
G12pzt=5.8015*10^5;     %Shear Modulus (AFC)(in-plane, psi)
thickpzt=0.006496063;   %Thickness of one layer of PZT lamina (AFC)

%E1pzt=5.4389*10^6;     %Young's Modulus (Ron Barrett)
%E2pzt=2.0305*10^6;     %Young's Modulus (Ron Barrett)
%G12pzt=5.5114*10^5;    %Shear's Modulus (Ron Barrett)
%thickpzt=0.005;        %Thickness of one layer of PZT lamina (Ron Barrett)
%d13=1.66*10^-10;       %Dielectric constant (m/V)

%E1pzt=9.1374*10^6;     %Young's Modulus (Zhou, Liang & Rogers)
%E1pzt=10.153*10^7;     %Young's Modulus (Crawley, de Luis)

v12pzt=0.30;            %Poisson's Ratio
%v21pzt=0.30;           %Poisson's Ratio

%*****************************************************************************
anglepzt=45;            %Orientation of PZT patch
theta=45;               %Center composite fiber rotation angle (deg)
times=1;                %Number of times lamina is wound
sym=0;                  %Symmetry of lamina 0=no,1=yes

%*****************************************************************************
%Define layer of angled lamina (only one layer of variable) orientation angles
anglemin=0;
angleincr=2;
anglemax=90;

count=0;                %Reset the loop-count variable (# of angles)

for j=anglemin:angleincr:anglemax   %Loop through the angle range

    count=count+1;
    angle(count)=j;
```

```
%*******************************************************************************
%Define layer of angled lamina-pzt orientation angles
orientall=[0 j anglepzt -j 0];
orientcom=[0 j theta -j 0];
locatepzt=3;            %The PZT layer location in the laminate

%*******************************************************************************
%Redefine thicknesses according to number of plies
t=[thick];                                  %Thickness vector per layer of lamina
t1=times*thick*length(orientcom)*(sym+1); %Total thickness of laminate at main spar
t2=t1;                                      %Total thickness of laminate at rear spar

%Total thickness of laminate (composite and pzt) at skin
ts=times*thick*(length(orientall)-1)*(sym+1)+thickpzt;

%*******************************************************************************
%Form material properties for each angle ply (number of angle ply from orientall)
E1xp=ones(size(orientall))*E1;
E2xp=ones(size(orientall))*E2;
G12xp=ones(size(orientall))*G12;
v12xp=ones(size(orientall))*v12;
txp=ones(size(orientall))*t;

E1xp(locatepzt)=E1pzt;
E2xp(locatepzt)=E2pzt;
G12xp(locatepzt)=G12pzt;
v12xp(locatepzt)=v12pzt;
txp(locatepzt)=thickpzt;

%*******************************************************************************
%Call Layup.m subroutine to calculate composite-pzt laminate engineering properties
[Epx,Epy,Gpxy,ap,vpxy,vpyx,npsx,npxs,npys,npsy]=Layup(E1xp,E2xp,v12xp,G12xp,txp,...
                                                    orientall,times,sym);
```

```
%The Compliance Matrix (plane stress) for the Composite-PZT Laminate in the x-y
%structural axes:
Sp11=1/Epx;    Sp12=-vpyx/Epy; Sp14=npsx/Gpxy;
Sp21=-vpxy/Epx; Sp22=1/Epy;    Sp24=npsy/Gpxy;
Sp41=npxs/Epx;  Sp42=npys/Epy;  Sp44=1/Gpxy;

Spzt=[Sp11 Sp12 Sp14;Sp21 Sp22 Sp24;Sp41 Sp42 Sp44];

%*****************************************************************************
%Calculate laminate engineering properties (composite laminate only)
E1x=ones(size(orientcom))*E1;
E2x=ones(size(orientcom))*E2;
G12x=ones(size(orientcom))*G12;
v12x=ones(size(orientcom))*v12;
tx=ones(size(orientcom))*t;

%Call Layup.m subroutine to calculate composite only laminate engineering properties
[Ex,Ey,Gxy,a,vxy,vyx,nsx,nxs,nys,nsy]=Layup(E1x,E2x,v12x,G12x,tx,orientcom,times,sym);

%The Compliance Matrix (plane stress) for the Composite-PZT Laminate in the x-y
%structural axes:
S11=1/Ex;    S12=-vyx/Ey; S14=nsx/Gxy;
S21=-vxy/Ex; S22=1/Ey;    S24=nsy/Gxy;
S41=nxs/Ex;  S42=nys/Ey;  S44=1/Gxy;

Scom=[S11 S12 S14;S21 S22 S24;S41 S42 S44];

%*****************************************************************************
%Call anisotropic torsion solution subroutine to calculate the amount of tip torsion
%for the single cell box beam
[fideg]=Anisotorsion_pzt(cr,c1,c2,h1,h2,l21,l22,t1,t2,ts,L,P,Vy,Vx,Mx,My,M,Spzt,Scom);

twist(count)=fideg;
```

```
end
orientall
twist

%Declare plot style lines and markers
linestyle=['b- ';'g- ';'r- ';'m- ';'c- ';'k- ';'y- '];
markstyle=['b+ ';'go ';'rh ';'md ';'cp ';'k* ';'yv '];

figure(1); plot(angle,twist,markstyle(2,:));
hold on;
plot(angle,twist,linestyle(2,:));
hold on;

title(['Twist Angles Due To Uniform Moment']);

ylabel('Twist Angle (deg)');
xlabel('Fiber Angle (deg)');
legend('AFC',0);
grid on;
```

```
%Function Anisotorsion_pzt

%Written by Capt Peter Cseke, Jr. - Fall 1999 - AFIT/ENY
%Calculates the tip twist angle of the single-cell trapezoid box-beam with PZT actuator
%embedded in top and bottom skins.  No PZT in main or rear spars.
%Uses:      Box beam geometric and material parameters are inputed from driver program
%Output:    Tip twist angle in degrees
%Also works for isotropic torsion, because Beta2=0 (B2 and Bp2) for isotropic materials.

function[Fideg]=Anisotorsion_pzt(cr,c1,c2,h1,h2,l21,l22,t1,t2,ts,L,P,Vy,Vx,Mx,My,M,Sp,Sc);

%*************************************************************************
%Define the half-width, and top surface length correction factor
d=cr*(c2-c1)/2;
T=sqrt(1+((h2-h1)/(4*d))^2);
Area=2*d*(h1/2+h2/2);
m=(h1+h2)/4;

%Designate the compliance Matrix for the composite laminate:
S11=Sc(1,1);S12=Sc(1,2);S14=Sc(1,3);
S21=Sc(2,1);S22=Sc(2,2);S24=Sc(2,3);
S41=Sc(3,1);S42=Sc(3,2);S44=Sc(3,3);

%Designate the compliance Matrix for the composite-pzt laminate:
Sp11=Sp(1,1);Sp12=Sp(1,2);Sp14=Sp(1,3);
Sp21=Sp(2,1);Sp22=Sp(2,2);Sp24=Sp(2,3);
Sp41=Sp(3,1);Sp42=Sp(3,2);Sp44=Sp(3,3);

%Define elastic constants for constitutive relations of composite laminate only:
alfa1=S11;alfa2=S14;alfa4=S44;

%Define elastic constants for constitutive relations of composite-pzt laminate:
alfap1=Sp11;alfap2=Sp14;alfap4=Sp44;
```

```
%Define elastic constants for force-strain relations of composite laminate only:
B1=1/alfa1;B2=-alfa2/alfa1;B4=alfa4-(alfa2^2/alfa1);

%Define elastic constants for force-strain relations of composite-pzt laminate:
Bp1=1/alfap1;Bp2=-alfap2/alfap1;Bp4=alfap4-(alfap2^2/alfap1);

%Define the elements of the B matrix:
b11=4*Bp1*ts*d*T+B1*t2*h2+B1*t1*h1;
b12=0;
b13=-B1*d*(t2*h2-t1*h1);

b21=0;
b22=(-Bp1*ts*h2^3*d*T)/(3*(h2-h1))+(1/(3*(h2-h1)))*(Bp1*ts*h1^3*d*T)-...
   (1/12)*B1*t2*h2^3-(1/12)*B1*t1*h1^3;
b23=0;

b31=B1*d*(t2*h2-t1*h1); b32=0;
b33=(-4/3)*Bp1*ts*d^3*T-B1*t2*d^2*h2-B1*t1*d^2*h1;

B=[b11 b12 b13;b21 b22 b23;b31 b32 b33];

A=inv(B); a11=A(1,1);a12=A(1,2);a13=A(1,3);
a21=A(2,1);a22=A(2,2);a23=A(2,3);
a31=A(3,1);a32=A(3,2);a33=A(3,3);

a4=(1/2)*d*B1*t2*h2^2+2*h2*Bp1*ts*d^2*T+d*h1*B1*t2*h2+4*h1*Bp1*ts*d^2*T+...
   (1/2)*d*B1*t1*h1^2+2*m*d*T*B1*t2*h2+8*m*Bp1*d^2*T^2*ts;

a5=(1/12)*(-B1*t1*h1^3+6*Bp1*ts*d*T*h2*h1+B1*t2*h2^3+6*Bp1*ts*d*T*h2^2+...
   8*m*Bp1*d*T^2*ts*h2+16*m*Bp1*d*T^2*ts*h1);

a6=(-1/2)*d^2*(-4*m*T*B1*t2*h2-t2*Bp1*h2^2+4*B1*t2*d*T*h2-4*d*t2*T*Bp1*h2+...
   B1*t1*h1^2-2*B1*h1*t2*h2);
```

```
%Define the elements of the C matrix:
c11=B2*h2-B2*h1; c21=Bp2*d*T*(h2+h1); c31=B2*d*(h2+h1);

c12=B2*((-1/2)*B1*t2*h2^2-2*h2*Bp1*ts*d*T+4*h1*Bp1*ts*d*T+(1/2)*B1*t1*h1^2+...
   h1*B1*t2*h2)+Bp2*(2*d*T*B1*t2*h2+4*Bp1*ts*d^2*T^2);
c22=(B2/12)*(B1*t1*h1^3+B1*t2*h2^3)+(Bp2/2)*(-d*T*B1*t2*h2^2-4*Bp1*ts*d^2*T^2*h1-...
   d*T*h1*B1*t2*h2-4*Bp1*ts*d^2*T^2*h2);
c32=(-d/6)*(3*B2*B1*t2*h2^2+12*d*B2*T*Bp1*ts*h2+8*Bp1*ts*d^2*T^2*Bp2+...
   3*B2*B1*t1*h1^2+6*B2*h1*B1*t2*h2+24*d*B2*T*h1*Bp1*ts);

c13=(1/12)*B2*(B1*t2*h2^3+6*Bp1*ts*h2^2*d*T+6*Bp1*ts*h1*h2*d*T+B1*t1*h1^3);
c23=(1/4)*Bp1*ts*Bp2*d^2*T^2*(h2^2+h1^2+2*h1*h2);
c33=(1/12)*d*B2*(-B1*t1*h1^3+B1*t2*h2^3+6*Bp1*ts*h2^2*d*T+6*Bp1*ts*h1*h2*d*T);

c14=(1/6)*d*(-8*Bp1*ts*d^2*T^2*Bp2+3*B2*B1*t1*h1^2-6*B2*B1*h1*t2*h2...
   -12*Bp2*d*T*B1*t2*h2-12*d*B2*t2*T*h2*B1+3*B2*t2*Bp1*h2^2+12*d*B2*t2*T*Bp1*h2);
c24=(1/12)*d*(B2*B1*t1*h1^3+6*Bp2*d*T*h2*h1*B1*t2+6*Bp2*d*T*B1*t2*h2^2-B2*t2*Bp1*h2^3);
c34=(1/2)*d^2*B2*(-4*d*t2*T*h2*B1+t2*Bp1*h2^2+4*t2*d*T*Bp1*h2-B1*t1*h1^2+2*B1*h1*t2*h2);

C=[c11 c12 c13 c14;c21 c22 c23 c24;c31 c32 c33 c34];

%Define the elements of the D vector:
d1=(4*Bp4*d*T*t1*t2+B4*ts*t1*h2+B4*ts*t2*h1)/(ts*t2*t1);
d2=(-1/2)*(B4*ts*t1*B1*t2*h2^2+16*Bp1*d^2*T^2*Bp4*t2*ts*t1+8*B4*t2*ts^2*h1*Bp1*d*T+...
   2*B4*t2^2*ts*B1*h1*h2+B4*t2*ts*B1*t1*h1^2+4*Bp4*t2^2*t1*d*T*h2*B1+...
   4*B4*ts^2*t1*h2*Bp1*d*T)/(t2*ts*t1);
d3=(1/12)*(8*Bp1*d^2*T^2*Bp4*t2*h2+16*Bp1*d^2*T^2*Bp4*t2*h1+6*B4*d*T*Bp1*ts*h2^2+...
   6*B4*d*T*Bp1*ts*h1*h2+B4*B1*t2*h2^3-B1*B4*t2*h1^3)/t2;
d4=(1/2)*d*(4*B4*d*T*ts*t1*Bp1*h2+2*Bp4*B1*ts*h1*h2*t2-Bp4*B1*ts*t1*h1^2+...
   4*Bp4*t1*d*T*B1*t2*h2+B4*ts*t1*Bp1*h2^2-4*B4*d*T*ts*t1*h2*B1)/(ts*t1);

%Define the shear flow at s=0:
q0=(1/(2*Area))*(M-a22*a5*Vy+(a13*a4-a33*a6)*Vx);
```

```
%Define the derivatives of the strain, and curvatures:
e0p=a13*Vx; Kxp=a22*Vy; Kyp=a33*Vx;

%Define the values for the Q's:
Q1=c11*q0+c12*e0p+c13*Kxp+c14*Kyp;
Q2=c21*q0+c22*e0p+c23*Kxp+c24*Kyp;
Q3=c31*q0+c32*e0p+c33*Kxp+c34*Kyp;

Z1=0; Z2=0;Z3=0; e0=a11*(P-Q1+Z1)-a12*(Mx+Q2+Z2)-a13*(My+Q3+Z3);
Kx=a21*(P-Q1+Z1)-a22*(Mx+Q2+Z2)-a23*(My+Q3+Z3);
Ky=a31*(P-Q1+Z1)-a32*(Mx+Q2+Z2)-a33*(My+Q3+Z3);

%The rotation in radians per unit length:
dFdz=(1/(2*Area))*(-e0*c11+Kx*c21+Ky*c31+q0*d1+e0p*d2+Kxp*d3+Kyp*d4);

%The rotation in degrees per unit length:
dfdz_deg=dFdz*180/pi;

%The rotation in degrees for entire length of beam:
Fideg=dfdz_deg*L;

return
```

Appendix E. Anisotropic

Composite-PZT Strain Actuation Codes

```
%Program Compl_aniso_pzt_e.m

%Written by Capt Peter Cseke, Jr. - Fall 1999 - AFIT/ENY
%Driver program to Matlab functions  Layup.m
%                                    Anisotorsion_pzt.m
%Defines trapezoid single-cell box beam geometric and material properties,
%applied cross section loads and moments.
%Calculates tip twist angle of box beam.
%Uses   :  Layup.m to calculate engineering properties of lamina and
%          composite-pzt lamina.
%          Anisotorsion_pzt_e.m to calculate twist angle of box beam.
%Outputs:  Tip twist angle of box beam.
%
%User enters:
%orientation: [0 45 -45 90 -90] etc, as a row vector;
%times      : The number of times ply is repeated;
%symmetry   : 0 for no;
%             1 for yes
%Example    : [0 45 -45 90]4s
%    orient = [0 45 -45 90]
%     times = 4
%       sym = 1
%Note       : All properties are vectors with properties per ply.
%Limits     : Assumes weighted center of laminate is at h/2.
%*****************************************************************************

close all; clear all;
%Define beam geometric parameters
```

```
cr=60.96;               %Root chord length [in]
c1=0.25;c2=0.70;        %Main spar and Rear spar location in chord percent
h1=8.4334;              %Height of Main Spar [in]
h2=5.3035;              %Height of Rear Spar [in]
l21=27.7732;            %Length of top skin between Main and Rear Spars [in]
l22=29.2992;            %Length of bottom skin between Main and Rear Spars [in]
L=255.96;               %Spanwise length of torque box [in]

%Define the Loads and Moments acting:
P=0;                    %Spanwise extensional load  [lb]
Vx=0;                   %Vertical shear load (lift) [lb]
Vy=0;                   %Horizontal shear load (drag) [lb]
Mx=0;                   %Applied moment about x axis (bending) [in-lb]
My=0;                   %Applied moment about y axis (bending) [in-lb]
M_ftlb=0;               %Applied moment about z axis (torque) [ft-lb]
M=M_ftlb*12;            %                                     [in-lb]

%Voltage applied to PZT lamina in poling direction
%V=[100 250 500 750 1000];      %AFC Lamina
V=[50 75 100 150 200];          %G-1195 Lamina

%For the sake of the legend for figure 2, rewrite in string format
%Uncomment depending which PZT lamina is used
%Volts=['100 V ';'250 V ';'500 V ';'750 V ';'1000 V'];   %AFC Lamina
Volts=['50 V ';'75 V ';'100 V';'150 V';'200 V'];         %G-1195 lamina

%*************************************************
%Carbon/Epoxy (AS4/3501-6)
E1=20.6*10^6;           %Young's Modulus (fiber direction) [psi]
E2=1.50*10^6;           %Young's Modulus (transverse direction) [psi]
G12=1.04*10^6;          %Shear Modulus (in-plane) [psi]
v12=0.27;               %Poisson's Ratio
v21=0.02;               %Poisson's Ratio
thick=0.005;            %Thickness per layer of angle lamina
```

```
                    %(given by material props.)

%*****************************************************
%AFC Piezoceramic Lamina (Aaron Bent)
%E1pzt=4.6786*10^6;              %Young's Modulus (poling, or fiber direction psi)
%E2pzt=2.4173*10^6;              %Young's Modulus (transverse direction)[psi]
%G12pzt=5.8015*10^5;             %Shear Modulus (in-plane) [psi]
%thickpzt_mm=0.165;              %Thickness of one layer of PZT lamina [mm]
%thickpzt_m=thickpzt_mm/1000;    %Thickness of one layer of PZT lamina [m]
%thickpzt=thickpzt_m/0.0254;     %Thickness of one layer of PZT lamina [in]
%efinsp_m=0.001125;              %Electrode finger spacing [m]

%thick_select=efinsp_m;         %The AFC lamina uses electrode fingerspacing
                                %as characteristic thickness to divide V
%d33=180*10^-12;                %Piezoelectric constant in poling direction [m/V]
%d31=-50*10^-12;                %Piezoelectric constant in transverse direction [m/V]

%PZT-Composite Lamina G-1195 (Ron Barrett)
E1pzt=5.4389*10^6;              %Young's Modulus (poling or fiber direction psi)
E2pzt=2.0305*10^6;              %Young's Modulus (transverse direction)[psi]
G12pzt=5.5114*10^5;             %Shear Modulus (in-plane, psi)
thickpzt_mm=0.2032;             %Thickness of one layer of PZT lamina [mm]
thickpzt_m=thickpzt_mm/1000;    %Thickness of one layer of PZT lamina [m]
thickpzt=thickpzt_m/0.0254;     %Thickness of one layer of PZT lamina [in]

Lambda=207*10^-6;               %Actuation Strain
thick_select=thickpzt_m;        %The G-1195 lamina uses lamina thickness to divide V%

d33=250*10^-12;                 %Piezoelectric constant in poling direction [m/V]
d31=25*10^-12;                  %Piezoelectric constant in transverse direction (m/V)
                                %using the small signal linear model
                                %(Crawley-Anderson 1990)
v12pzt=0.30;                    %Poisson's Ratio
```

```
anglepzt=45;                    %Orientation of PZT patch

%*************************************************************************
theta=45;                       %Center composite fiber rotation angle (deg)
times=1;                        %Number of times lamina is wound
sym=0;                          %Symmetry of lamina 0=no,1=yes

%*************************************************************************
%Define layer of angled lamina (only one layer of variable) orientation angles
anglemin=0
angleincr=5          %Keep increment at 5, so that 15, 30, 45, etc. can be found
anglemax=90;

%The same defined for easier plotting
angle_select=[15 30 45 60 75 90]; anglerange=['15 deg';'30
deg';'45 deg';'60 deg';'75 deg';'90 deg'];

count=0;                        %Reset the loop-count variable (# of angles)
select=1;                       %Set counter for counting elements of angle-select
for j=anglemin:angleincr:anglemax   %Loop through the angle range

   count=count+1;                   %Update the loop variable
   angle(count)=j;
   orientall=[0 j anglepzt -j 0];
   %Orientation angles for 3 layers of composite-PZT laminate:
   %orientall=[0 anglepzt anglepzt anglepzt 0];
   orientcom=[0 j theta -j 0];      %Orientation angles for composite laminate
   locatepzt=3;                     %The pzt layer location in the laminate
                                    %Needs to be changed to reflect changes in
                                    %"orientall" and "orientcomp"

    %************************************************************************
    %Redefine thicknesses according to number of plies
    t=[thick];                      %Thickness vector per layer of lamina
```

```
t1=times*thick*length(orientcom)*(sym+1); %Total main spar lamina thickness
t2=t1;                          %Total rear spar lamina thickness

%Total thickness of laminate (composite and pzt) at skin
ts=times*thick*(length(orientall)-1)*(sym+1)+thickpzt;

%*************************************************************************
%Form the material properties for each angle ply
%(number of angle ply from orientall)
E1xp=ones(size(orientall))*E1;
E2xp=ones(size(orientall))*E2;
G12xp=ones(size(orientall))*G12;
v12xp=ones(size(orientall))*v12;
txp=ones(size(orientall))*t;

E1xp(locatepzt)=E1pzt;%E1xp(2)=E1pzt;E1xp(4)=E1pzt;
E2xp(locatepzt)=E2pzt;%E2xp(2)=E2pzt;E2xp(4)=E2pzt;
G12xp(locatepzt)=G12pzt;%G12xp(2)=G12pzt;G12xp(4)=G12pzt;
v12xp(locatepzt)=v12pzt;%v12xp(2)=v12pzt;v12xp(4)=v12pzt;
txp(locatepzt)=thickpzt;%txp(2)=thickpzt;txp(4)=thickpzt;

%*************************************************************************
%Call the Layup.m subroutine to calculate composite-pzt laminate engineering
%properties
[Epx,Epy,Gpxy,ap,vpxy,vpyx,npsx,npxs,npys,npsy]=Layup(E1xp,E2xp,...
                                    v12xp,G12xp,txp,orientall,times,sym);

%The Compliance Matrix (plane stress) for the Composite-PZT Laminate in the x-y
%structural axes:
Sp11=1/Epx;     Sp12=-vpyx/Epy; Sp14=npsx/Gpxy;
Sp21=-vpxy/Epx; Sp22=1/Epy;     Sp24=npsy/Gpxy;
Sp41=npxs/Epx;  Sp42=npys/Epy;  Sp44=1/Gpxy;

Spzt=[Sp11 Sp12 Sp14;Sp21 Sp22 Sp24;Sp41 Sp42 Sp44];
```

```
%************************************************************************
%Calculate laminate engineering properties (composite laminate only)
E1x=ones(size(orientcom))*E1;
E2x=ones(size(orientcom))*E2;
G12x=ones(size(orientcom))*G12;
v12x=ones(size(orientcom))*v12;
tx=ones(size(orientcom))*t;

%Call the Layup.m subroutine to get composite laminate engineering properties
[Ex,Ey,Gxy,a,vxy,vyx,nsx,nxs,nys,nsy]=Layup(E1x,E2x,...
                                        v12x,G12x,tx,orientcom,times,sym);

%The Compliance Matrix (plane stress) for the Composite Laminate in the
%x-y structural axes:
S11=1/Ex;    S12=-vyx/Ey; S14=nsx/Gxy;
S21=-vxy/Ex; S22=1/Ey;    S24=nsy/Gxy;
S41=nxs/Ex;  S42=nys/Ey;  S44=1/Gxy;

Scom=[S11 S12 S14;S21 S22 S24;S41 S42 S44];

%************************************************************************
for i=1:length(V);
  V(i);
  %The applied electric field (thick_select depends on type of PZT lamina used)
  E33=V(i)/thick_select;            %[V/m]

  %*********************  Use only for G-1195  ***************************
  Ea=V(i)/thickpzt_mm          %Applied voltage per milimeter [V/mm]

  %From Crawley and Lazarus 1991 using Figure A1.
  Lambda=((150*10^-6)/400)*Ea   %Induced Strain from linear approximation

  %From Crawley and Anderson 1990 using Figure 7.
```

```
d33=((50*10^-12)/(120*10^-6))*(Lambda)+(240*10^-12)

%d33=Lambda/E33;              %The secant piezoelectric coefficient [m/V]
d31=(1/10)*d33
%************************************************************************

%The piezoelectric strain-shear vector in the material principle directions
pztstrain12=[d31 0 0;0 d31 0;0 0 d33]*E33;  % {x y z}=[T]{1 2 3} rotation
%pztstrain12=[d33 0 0;0 d31 0;0 0 d31]*E33; % {z x y}=[T]{3 1 2} rotation

%Subroutine to transform principle strains/shears into structural strains/shears
pztstrainzx=transform(pztstrain12,anglepzt);

%The piezoelectric strain and shear in the z-x structural axes
ep_z=pztstrainzx(3,3);
%ep_z=pztstrainzx(1,1);

gp_zx=pztstrainzx(3,1);
%gp_zx=pztstrainzx(1,2);

%Call the anisotropic torsion solution subroutine to calculate the amount
%of tip torsion for the single cell box beam
fideg=Anisotorsion_pzt_e(cr,c1,c2,h1,h2,l21,l22,t1,t2,ts,L,P,Vy,Vx,Mx,...
                         My,M,ep_z,gp_zx,Spzt,Scom);

twist(count,i)=fideg;   %The 2-D twist angle variable
                        %Rows: different composite angle
                        %Columns: different Voltage applied
end

%Select only the angles desired to plot (don't want to plot all angles 0-90)
if j==angle_select(select)
   twist_select(select,:)=twist(count,:);
   select=select+1;
```

```
      end
end

%Here are the angles from 15-90 with 15 degree increments
twist_select

%Declare plot style lines and markers
linestyle=['b- ';'g- ';'r- ';'m- ';'k- ';'c- ';'y- '];
markstyle=['b+ ';'go ';'rh ';'md ';'kp ';'c* ';'yv '];

figure(1)
for k=1:1:length(angle_select)      %Length of lamina angles
   %Plot the angles of twist with markers
   plot(V,twist_select(k,:),markstyle(k,:));
   hold on;
end for k=1:1:length(angle_select)
   %Plot the angles of twist with lines for better visibility
   plot(V,twist_select(k,:),linestyle(k,:)');
   hold on;
end

%title(['Twist Angles Due To Strain Actuation - Lamina Angles']);
ylabel('Twist Angle (deg)');
xlabel('Applied Electric Field (V)');
legend([anglerange],2);
grid on; hold off;

figure(2)
for m=1:1:length(V)                    %Length of Voltages
   %Plot the angles of twist with markers
   plot(angle,twist(:,m),markstyle(m,:));
   hold on;
end for m=1:1:length(V)
   %Plot the angles of twist with lines for better visibility
```

```
   plot(angle,twist(:,m),linestyle(m,:));
   hold on;
end
%title(['Twist Angles Due To Strain Actuation - Applied Voltage']);
ylabel('Twist Angle (deg)');
xlabel('Fiber Angle (deg)');
legend([Volts],0);
grid on; hold off;
```

```
%Function Anisotorsion_pzt_e.m

%Written by Capt Peter Cseke, Jr. - Fall 1999 - AFIT/ENY
%Calculates the tip twist angle of the single-cell trapezoid box-beam with PZT actuator
%embedded in top and bottom skins.  No PZT in main or rear spars.
%Uses:      Box beam geometric and material parameters are inputed from driver program
%Output:    Tip twist angle in degrees
%Also works for isotropic torsion, because Beta2=0 (B2 and Bp2) for isotropic materials

function[Fideg]=Anisotorsion_pzt_e(cr,c1,c2,h1,h2,l21,l22,t1,t2,ts,L,P,Vy,Vx,Mx,...
                                   My,M,ep,gp,Sp,Sc);

%*************************************************************************
%Define the half-width, and top surface length correction factor
d=cr*(c2-c1)/2;
T=sqrt(1+((h2-h1)/(4*d))^2);
Area=2*d*(h1/2+h2/2);
m=(h1+h2)/4;

%Designate the compliance Matrix for the composite laminate:
S11=Sc(1,1);S12=Sc(1,2);S14=Sc(1,3);
S21=Sc(2,1);S22=Sc(2,2);S24=Sc(2,3);
S41=Sc(3,1);S42=Sc(3,2);S44=Sc(3,3);

%Designate the compliance Matrix for the composite-pzt laminate:
Sp11=Sp(1,1);Sp12=Sp(1,2);Sp14=Sp(1,3);
Sp21=Sp(2,1);Sp22=Sp(2,2);Sp24=Sp(2,3);
Sp41=Sp(3,1);Sp42=Sp(3,2);Sp44=Sp(3,3);

%Define elastic constants for constitutive relations of composite laminate only:
alfa1=S11;alfa2=S14;alfa4=S44;

%Define elastic constants for constitutive relations of composite-pzt laminate:
```

```
alfap1=Sp11;alfap2=Sp14;alfap4=Sp44;

%Define elastic constants for force-strain relations of composite laminate only:
B1=1/alfa1;B2=-alfa2/alfa1;B4=alfa4-(alfa2^2/alfa1);

%Define elastic constants for force-strain relations of composite-pzt laminate:
Bp1=1/alfap1;Bp2=-alfap2/alfap1;Bp4=alfap4-(alfap2^2/alfap1);

%Define the elements of the B matrix:
b11=4*Bp1*ts*d*T+B1*t2*h2+B1*t1*h1; b12=0;
b13=-B1*d*(t2*h2-t1*h1);

b21=0;
b22=(-Bp1*ts*h2^3*d*T)/(3*(h2-h1))+(1/(3*(h2-h1)))*(Bp1*ts*h1^3*d*T)-...
   (1/12)*B1*t2*h2^3-(1/12)*B1*t1*h1^3;
b23=0;

b31=B1*d*(t2*h2-t1*h1);
b32=0;
b33=(-4/3)*Bp1*ts*d^3*T-B1*t2*d^2*h2-B1*t1*d^2*h1;

B=[b11 b12 b13;b21 b22 b23;b31 b32 b33];

A=inv(B);
a11=A(1,1);a12=A(1,2);a13=A(1,3);
a21=A(2,1);a22=A(2,2);a23=A(2,3);
a31=A(3,1);a32=A(3,2);a33=A(3,3);

a4=(1/2)*d*B1*t2*h2^2+2*h2*Bp1*ts*d^2*T+d*h1*B1*t2*h2+4*h1*Bp1*ts*d^2*T+...
   (1/2)*d*B1*t1*h1^2+2*m*d*T*B1*t2*h2+8*m*Bp1*d^2*T^2*ts;

a5=(1/12)*(-B1*t1*h1^3+6*Bp1*ts*d*T*h2*h1+B1*t2*h2^3+6*Bp1*ts*d*T*h2^2+...
   8*m*Bp1*d*T^2*ts*h2+16*m*Bp1*d*T^2*ts*h1);
```

```
a6=(-1/2)*d^2*(-4*m*T*B1*t2*h2-t2*Bp1*h2^2+4*B1*t2*d*T*h2-4*d*t2*T*Bp1*h2+...
   B1*t1*h1^2-2*B1*h1*t2*h2);

%Define the elements of the C matrix:
c11=B2*h2-B2*h1;
c21=Bp2*d*T*(h2+h1);
c31=B2*d*(h2+h1);

c12=B2*((-1/2)*B1*t2*h2^2-2*h2*Bp1*ts*d*T+4*h1*Bp1*ts*d*T+(1/2)*B1*t1*h1^2+...
   h1*B1*t2*h2)+Bp2*(2*d*T*B1*t2*h2+4*Bp1*ts*d^2*T^2);
c22=(B2/12)*(B1*t1*h1^3+B1*t2*h2^3)+(Bp2/2)*(-d*T*B1*t2*h2^2-4*Bp1*ts*d^2*T^2*h1-...
   d*T*h1*B1*t2*h2-4*Bp1*ts*d^2*T^2*h2);
c32=(-d/6)*(3*B2*B1*t2*h2^2+12*d*B2*T*Bp1*ts*h2+8*Bp1*ts*d^2*T^2*Bp2+...
   3*B2*B1*t1*h1^2+6*B2*h1*B1*t2*h2+24*d*B2*T*h1*Bp1*ts);

c13=(1/12)*B2*(B1*t2*h2^3+6*Bp1*ts*h2^2*d*T+6*Bp1*ts*h1*h2*d*T+B1*t1*h1^3);
c23=(1/4)*Bp1*ts*Bp2*d^2*T^2*(h2^2+h1^2+2*h1*h2);
c33=(1/12)*d*B2*(-B1*t1*h1^3+B1*t2*h2^3+6*Bp1*ts*h2^2*d*T+6*Bp1*ts*h1*h2*d*T);

c14=(1/6)*d*(-8*Bp1*ts*d^2*T^2*Bp2+3*B2*B1*t1*h1^2-6*B2*B1*h1*t2*h2...
   -12*Bp2*d*T*B1*t2*h2-12*d*B2*t2*T*h2*B1+3*B2*t2*Bp1*h2^2+12*d*B2*t2*T*Bp1*h2);
c24=(1/12)*d*(B2*B1*t1*h1^3+6*Bp2*d*T*h2*h1*B1*t2+6*Bp2*d*T*B1*t2*h2^2-B2*t2*Bp1*h2^3);
c34=(1/2)*d^2*B2*(-4*d*t2*T*h2*B1+t2*Bp1*h2^2+4*t2*d*T*Bp1*h2-B1*t1*h1^2+2*B1*h1*t2*h2);

C=[c11 c12 c13 c14;c21 c22 c23 c24;c31 c32 c33 c34];

%Define the elements of the D vector:
d1=(4*Bp4*d*T*t1*t2+B4*ts*t1*h2+B4*ts*t2*h1)/(ts*t2*t1);
d2=(-1/2)*(B4*ts*t1*B1*t2*h2^2+16*Bp1*d^2*T^2*Bp4*t2*ts*t1+8*B4*t2*ts^2*h1*Bp1*d*T+...
   2*B4*t2^2*ts*B1*h1*h2+B4*t2*ts*B1*t1*h1^2+4*Bp4*t2^2*t1*d*T*h2*B1+...
   4*B4*ts^2*t1*h2*Bp1*d*T)/(t2*ts*t1);
d3=(1/12)*(8*Bp1*d^2*T^2*Bp4*t2*h2+16*Bp1*d^2*T^2*Bp4*t2*h1+6*B4*d*T*Bp1*ts*h2^2+...
   6*B4*d*T*Bp1*ts*h1*h2+B4*B1*t2*h2^3-B1*B4*t2*h1^3)/t2;
d4=(1/2)*d*(4*B4*d*T*ts*t1*Bp1*h2+2*Bp4*B1*ts*h1*h2*t2-Bp4*B1*ts*t1*h1^2+...
```

```
   4*Bp4*t1*d*T*B1*t2*h2+B4*ts*t1*Bp1*h2^2-4*B4*d*T*ts*t1*h2*B1)/(ts*t1);

%Define the shear flow at s=0:
q0=(1/(2*Area))*(M-a22*a5*Vy+(a13*a4-a33*a6)*Vx);

%Define the derivatives of the strain, and curvatures:
e0p=a13*Vx;
Kxp=a22*Vy;
Kyp=a33*Vx;

%Define the values for the Q's:
Q1=c11*q0+c12*e0p+c13*Kxp+c14*Kyp;
Q2=c21*q0+c22*e0p+c23*Kxp+c24*Kyp;
Q3=c31*q0+c32*e0p+c33*Kxp+c34*Kyp;

Z1=4*ep*d*T*Bp1*ts;
Z2=0; Z3=0;
e0=a11*(P-Q1+Z1)-a12*(Mx+Q2-Z2)-a13*(My+Q3-Z3);
Kx=a21*(P-Q1+Z1)-a22*(Mx+Q2-Z2)-a23*(My+Q3-Z3);
Ky=a31*(P-Q1+Z1)-a32*(Mx+Q2-Z2)-a33*(My+Q3-Z3);

%The PZT shear around the perimeter (using shear in the structural axes)
g_total=4*gp*d*T;
e_total=4*ep*d*T;

%The rotation in radians per unit length:
dFdz=(1/(2*Area))*(-e0*c11+Kx*c21+Ky*c31+q0*d1+e0p*d2+Kxp*d3+Kyp*d4+e_total*c11+g_total);

%The rotation in degrees per unit length:
dfdz_deg=dFdz*180/pi;

%The rotation in degrees for entire length of beam:
Fideg=dfdz_deg*L;
return
```

```
%Function transform.m

%Written by Capt Peter Cseke, Jr. - Winter 2000 - AFIT/ENY
%Subroutine to Compl_aniso_pzt_e.m
%
%Calcultes the transformed values of the piezoelectric strain vector in the
%structural axes, given the PZT layup angle.
%
%Caution:   Fiber orientation (in this subroutine only) agrees with that
%           accepted in the literature for smart materials, that is:
%                                                   3 - fiber direction
%                                                   1 - transverse direction
%                                                   2 - out of plane direction
%           This change in notation does not affect the notation in main code
%           as long as the PZT strains are sent back in the z-x structural axes
%           that correspond to the original structural axes defined in the
%           problem statement.
%Uses   :   PZT strains (3x3 matrix) in principle axes 1-2
%Outputs:   PZT strains (3x3 matrix) in structural axes z-x.

function [pztstrainzx]=transform(pztstrain12,angledeg);

%Calculate the rotation angle in radians
anglerad=angledeg*pi/180;

%For the sake of simplicity
s=sin(anglerad);
c=cos(anglerad);

%The transformation matrix
Trans=[c 0 s;0 1 0;-s 0 c];  % {x y z}=[T]{1 2 3} rotation
%Trans=[c -s 0;s c 0;0 0 1]; % {z x y}=[T]{3 1 2} rotation
```

```
%Invert the transformation matrix
Cinv=inv(Trans);

%The transformation of PZT strains from the 3-1 principle into the z-x structural axes
pztstrainzx=Cinv*pztstrain12*Trans;

return
```

Bibliography

1. Agnes, Gregory S. *Vibration Control of Composite Beams Through Strain Actuation and H-Infinity Control Theory*. MS thesis, University of Maryland, 1991.

2. Badir, Ashraf M. *Analysis of Two-Cell Composite Beams*. Technical Report AIAA-95-1208, Clark Atlanta University, Dept. of Engineering, 1995.

3. Barrett, Ron. "Aeroservoelastic DAP Missile Fin Development," *Smart Materials and Structures*, *Vol. 2*:55–65 (1993).

4. Batra, R. C. and K. Gosh. "Deflection Control During Dynamic Deformations of Rectangular Plate Using Piezoceramic Elements," *AIAA Journal*, *Vol. 33*(8):1547–1548 (1995).

5. Bent, Aaron A. and N. W. Hagood. "Piezoelectric Fiber Composites with Interdigitated Electrodes," *Journal of Intelligent Material Systems and Structures* (1996).

6. Bernstein, Dennis S. "A Student's Guide to Research," *IEEE Control Systems*, 102–108 (February 1999).

7. Canan, James W. "Seeing More, and Risking Less, with UAVs," *Aerospace America*, *Vol. 37*(10):26–35 (October 1999).

8. Crawley, Edward F. and Eric H. Anderson. "Detailed Models of Piezoceramic Actuation in Beams," *Journal of Intelligent Material Systems and Structures*, *Vol. 1*:4–25 (January 1990).

9. Crawley, Edward F. and Javier de Luis. "Use of Piezoelectric Actuators as Elements of Intelligent Structures," *AIAA Journal*, *Vol. 26*(10):1373–1385 (October 1987).

10. Crawley, Edward F. and Kenneth B. Lazarus. "Induced Strain Actuation of Isotropic and Anisotropic Plates," *AIAA Journal*, *Vol. 29*(6):944–951 (1991).

11. Daniel, Isaac M. and Ori Ishai. *Engineering Mechanics of Composite Materials*. Oxford University Press, 1994.

12. Forster, Edwin E. and Henry T. Y. Yang. "Flutter Control of Wing Boxes Using Piezoelectric Actuators," *Journal of Aircraft*, *Vol. 35*(6):949–956 (November-December 1998).

13. John D. Anderson, Jr. *Introduction to Flight* (Third Edition). McGraw-Hill, Inc., 1989.

14. Kudva, Jayanth N., et al. *Adaptive Aircraft Wing*. AGARD SMP Lecture Series on "Smart Structures and Materials", October 1996.

15. Lazarus, Kenneth B. and Edward F. Crawley. *Induced Strain Actuation of Isotropic and Anisotropic Plates*. Technical Report AIAA-89-1326, Massachusetts Institute of Technology, Dept. of Aeronautics and Astronautics, 1989.

16. Lazarus, Kenneth B. and Edward F. Crawley. "Static Aeroelastic Control Using Strain Actuated Adaptive Structures," *Journal of Intelligent Material Systems and Structures*, *Vol. 2*:386–410 (July 1991).

17. Libove, Charles. "Stresses and Rate of Twist in Single-Cell Thin-Walled Beams with Anisotropic Walls," *AIAA Journal*, *Vol. 26*(9):1108–1118 (September 1988).

18. Maugh, Lawrence C. *Statically Indeterminate Structures*. John Wiley and Sons, Inc., 1964.

19. Megson, Thomas H. *Linear Analysis of Thin-Walled Elastic Structures*. John Wiley and Sons, Inc., 1974.

20. Peery, D. J. and J. J. Azar. *Aircraft Structures* (2nd Edition). McGraw-Hill, 1982.

21. Pytel, Andrew and Ferdinand L. Singer. *Strength of Materials*. Harper Collins Publishers, 1987.

22. Raymer, Daniel P. *Aircraft Design: A Conceptual Approach*. AIAA Education Series, American Institute of Aeronautics and Astronautics Inc., 1992.

23. Rogers, Jim, "Layup Matlab Subroutine," October 1999.

24. Romeo, Giulio, et al. "Nonlinear Angle of Twist of Advanced Composite Wing Boxes Under Pure Torsion," *AIAA Journal*, *Vol. 31*(6):1297–1302 (November-December 1994).

25. Rupert, Scott P. *Scattering Comparison of Alternative Wing Control Surfaces*. MS thesis, Air Force Institute of Technology, 2000.

26. Vinson, Jack R. *The Behavior of Thin Walled Structures: Beams, Plates, and Shells*. Kluwer Academic Publishers, 1989.

Vita

Captain Peter Cseke, Jr. was born on June 27, 1967 in Budapest, Hungary. He graduated from JAG H.S. in May of 1985. He then worked as a grounds-keeper at the local shipyard, a mainframe computer operator at a computer services company, served 18 months of mandatory military service, and owned a taxi-cab business. He moved to the U.S. in December 1989, and enrolled at the West Chester University of Pennsylvania to study Physics. After completing his Physics degree he transferred to the Pennsylvania State University for Aerospace Engineering, graduating with both degrees in May of 1995. In the summer of 1995 he attended the USAF Officer Training School at Maxwell AFB, Alabama, and was commissioned on September 22, 1995. He served as an Advanced Missile Flight Test Engineer at the 475th Weapons Evaluation Group, 83rd Fighter Weapons Squadron at Tyndall AFB, Florida, for the follow-on operational testing and evaluation (FOT&E) of the AIM-120 Advanced Medium Range Air-to-Air Missile (AMRAAM). He took part in William Tell 1996, and was project manager for the High-Time AIM-120 AMRAAM Hardware Reliability Program. In March of 1998 he was selected to attend the Air Force Institute of Technology's School of Engineering to earn a Master of Science Degree in Aeronautical Engineering. He is a member of the American Institute of Physics (AIP), the American Institute of Aeronautics and Astronautics (AIAA), the Honor Society of Aerospace Engineers ($\Sigma\Gamma$T), and the Honors Mathematics Society (PME). His follow-on assignment is to the Air Force Research Laboratory at Hill AFB, Utah.

Permanent address: 8 Kane Drive
Malvern, PA 19355
e-mail: pcsekejr@earthlink.net

REPORT DOCUMENTATION PAGE

Form Approved
OMB No. 0704-0188

1. AGENCY USE ONLY *(Leave blank)*	2. REPORT DATE	3. REPORT TYPE AND DATES COVERED
	09 MAR 00	Master's Thesis

4. TITLE AND SUBTITLE
MODELING PIEZOCERAMIC TWIST ACTUATION IN SINGLE-CELL ANISOTROPIC TORQUE BOX OF LOW-OBSERVABLE UAV WING

5. FUNDING NUMBERS

6. AUTHOR(S)
Peter Cseke, Jr., Capt, USAF

7. PERFORMING ORGANIZATION NAME(S) AND ADDRESS(ES)
Air Force Institute of Technology
2950 P Street, Bldg 640
Wright-Patterson AFB, OH 45433-7765

8. PERFORMING ORGANIZATION REPORT NUMBER
AFIT/GAE/ENY/00M-4

9. SPONSORING/MONITORING AGENCY NAME(S) AND ADDRESS(ES)
AFIT/ENY
2950 P Street, Bldg 640
Wright-Patterson AFB, OH 45433-7765

10. SPONSORING/MONITORING AGENCY REPORT NUMBER

11. SUPPLEMENTARY NOTES
Advisor: Dr. Gregory S. Agnes, Capt, USAF
DSN 785-6565 ext. 4317 COM (937) 255-6565 ext. 4317
gregory.agnes@afit.af.mil

12a. DISTRIBUTION AVAILABILITY STATEMENT
Approved for public release; Distribution unlimited

12b. DISTRIBUTION CODE

13. ABSTRACT *(Maximum 200 words)*

The reduction of an aircraft radar cross section increases its survivability in hostile airspace by making it more difficult to track by enemy radar. Replacing articulated control surfaces with adaptive controls reduces surface discontinuities, and enhances low observability. Actuation of the aerodynamic surfaces is achieved by electric field applied to embedded PZT actuators, creating differential strain and shear in the host substrate. The torsion of the designed baseline UAV's wing torque box was modeled with a full complement of air loads by extending the Bredt-Batho theorem through modifying Libove's method, using a thin-walled, linearly elastic, fully anisotropic, trapezoid cross section, single-cell beam. The linear tip twist angles due to a uniform cross-sectional moment were verified using the isotropic Bredt-Batho theorem and published anisotropic results by applying isotropic, than anisotropic material elastic properties. These angles, compared to calculated isotropic and published anisotropic examples, were within 3.1% and 6.9-10.9%, respectively. The PZT actuation was achieved by substituting the hybrid PZT-composite elastic properties into the derived solution and inducing strain and shear in the PZT by applying an electric field. Applied voltage induced strain actuation of the structure using the AFC-5H and G-1195 substrate-embedded PZT laminae induced torsion of 0.03-0.40 and 0.12-1.04 degrees, respectively.

14. SUBJECT TERMS
Adaptive Controls, Anisotropy, Composites, Piezoceramics, PZT, Strain Actuation, Shear Flow, Strain Tensor, Thin-Walled Beams, Torque Box, Torsion, UAV, Wing Box

15. NUMBER OF PAGES
181

16. PRICE CODE

17. SECURITY CLASSIFICATION OF REPORT	18. SECURITY CLASSIFICATION OF THIS PAGE	19. SECURITY CLASSIFICATION OF ABSTRACT	20. LIMITATION OF ABSTRACT
UNCLASSIFIED	UNCLASSIFIED	UNCLASSIFIED	UL